University of Tennessee, Knoxville
TRACE: Tennessee Research and Creative Exchange

Doctoral Dissertations | Graduate School

8-2014

Probing the size dependent chemical properties of metals in reduced dimension

Xiangshi Yin
University of Tennessee - Knoxville, xyin3@vols.utk.edu

Follow this and additional works at: https://trace.tennessee.edu/utk_graddiss

 Part of the Condensed Matter Physics Commons

Recommended Citation

Yin, Xiangshi, "Probing the size dependent chemical properties of metals in reduced dimension. " PhD diss., University of Tennessee, 2014.
https://trace.tennessee.edu/utk_graddiss/2877

This Dissertation is brought to you for free and open access by the Graduate School at TRACE: Tennessee Research and Creative Exchange. It has been accepted for inclusion in Doctoral Dissertations by an authorized administrator of TRACE: Tennessee Research and Creative Exchange. For more information, please contact trace@utk.edu.

To the Graduate Council:

I am submitting herewith a dissertation written by Xiangshi Yin entitled "Probing the size dependent chemical properties of metals in reduced dimension." I have examined the final electronic copy of this dissertation for form and content and recommend that it be accepted in partial fulfillment of the requirements for the degree of Doctor of Philosophy, with a major in Physics.

Hanno H. Weitering, Major Professor

We have read this dissertation and recommend its acceptance:

Norman Mannella, Robert N. Compton, Craig E. Barnes

Accepted for the Council:

Carolyn R. Hodges

Vice Provost and Dean of the Graduate School

(Original signatures are on file with official student records.)

University of Tennessee, Knoxville
Trace: Tennessee Research and Creative Exchange

Doctoral Dissertations | Graduate School

8-2014

Probing the size dependent chemical properties of metals in reduced dimension

Xiangshi Yin
University of Tennessee - Knoxville, xyin3@vols.utk.edu

This Dissertation is brought to you for free and open access by the Graduate School at Trace: Tennessee Research and Creative Exchange. It has been accepted for inclusion in Doctoral Dissertations by an authorized administrator of Trace: Tennessee Research and Creative Exchange. For more information, please contact trace@utk.edu.

To the Graduate Council:

I am submitting herewith a dissertation written by Xiangshi Yin entitled "Probing the size dependent chemical properties of metals in reduced dimension." I have examined the final electronic copy of this dissertation for form and content and recommend that it be accepted in partial fulfillment of the requirements for the degree of Doctor of Philosophy, with a major in Physics.

Hanno H. Weitering, Major Professor

We have read this dissertation and recommend its acceptance:

Norman Mannella, Robert N. Compton, Craig E. Barnes

Accepted for the Council:
Carolyn R. Hodges

Vice Provost and Dean of the Graduate School

(Original signatures are on file with official student records.)

Probing the size dependent chemical properties of metals in reduced dimension

A Dissertation Presented for the

Doctor of Philosophy

Degree

The University of Tennessee, Knoxville

Xiangshi Yin

August 2014

© by Xiangshi Yin, 2014
All Rights Reserved.

To Mengshu and Shouheng

Acknowledgements

I would like to thank my supervisor Dr. Hanno Weitering and Dr. Paul Snijders, for their support and guidance throughout these years. I am very lucky to have the chance to work with both of them. Dr. Weitering showed my direction in physics. He can always inspire me with his profound knowledge and insights of different scientific problems, and he gave me the confidence to finish my job. Dr. Snijders taught me everything from small to large in great detail during my research. His office door is always open to me, and he's never tired of answering my stupid questions. I learnt a lot from them, both science and the rigorous working attitude of doing research. These will be a great fortune in my whole life.

My thanks also go to all the other members of my committee, Dr. Norman Mannella, Dr. Adriana Moreo, Dr. Robert Compton, and Dr. Craig Barnes, for their inspiring questions and suggestions.

I am very grateful to the all members in Dr. Weitering's and Dr. Mannella's groups, including Dr. Mustafa Özer, Dr. Eun Jun Moon, Dr. Daniel Mulugeta, Dr. Paolo Vilmercati, Dr. Christine Cheney, Dr. Saban Hus, Dr. Ao Teng, Hao Hu, Weisong Tu, and Michael McConnell, Nicholas Sirica, Xiaoqian Hu, and Randal McMilan. Special thanks to Dr. Özer, I learnt the importance of being precise and making no mistake in doing research from him.

Finally, I'd like to thank my father, mother, and sister, for supporting me so many years to chase my dream. Their love didn't decay with the long distance between China and the US. I'd like to thank the other half of my life, Mengshu, for being with me and encouraging me in ups and downs. She is the one that worths everything for me.

Take small steps, and do not stop.

小步走，不停步

— *Dr. Chenggao Fan*
My mentor

Abstract

Heterogeneously catalyzed reactions typically start with adsorption and dissociation of reactant molecules on the surface of a solid catalyst. In many instances, this is followed by surface diffusion of the adsorbed species, chemical reaction, and removal of the product molecule. According to the Sabatier principle, optimal catalytic performance requires that the bonding between the adsorbate molecule and the surface should neither be too strong nor too weak. This bonding strength is directly related to the catalyst's surface electronic structure and hence, electronic structure modification would seem a promising approach for tuning catalytic activity.

There have been many studies along this line, including electronic structure modification via surface alloying, introduction of 'active sites', size control, and charge transfer between the catalyst and its support. The underlying physics is often expressed within the context of the d-band model by Norskov. Specifically, the bonding strength of adsorbate molecules on transition metal surfaces is strongly influenced by the interaction between the molecular orbitals and the metal d states, which can be parameterized by the location of the d-band center relative to the Fermi level. This model has been successful in explaining trends in catalytic activity of transition metal surfaces but there are exceptions, presumably to competing factors that are structure or element specific, and that are not considered in the model. To firmly establish the validity of the model, we investigated ultrathin Pd and Ru films and tuned the location of the d-band center by changing the film thickness one atomic layer at a

time, while keeping all other variables unchanged. Interestingly, while bulk Pd is reactive towards oxygen, Pd(111) films below five monolayer, grown on Ru(0001), are surprisingly inert to oxygen. This trend is fully in line with the *d*-band model prediction. Here, the shift of the *d*-band center is associated with the increased band width of the $4d_{xz}$ [4dxz] and $4d_{yz}$ [4dyz] orbitals. On the other hand, Ru(0001) films on Pd(111) reveal a more complex behavior which can be attributed to Pd segregation. This study provides an in-depth look at orbital specific contributions to the chemical reactivity, providing new knowledge that could be useful in surface catalysis.

Table of Contents

List of Figures

Chapter 1

Introduction

1.1 Catalytic activities of materials in reduced dimension

Catalysis is arguably the most essential industrial process in our economy. It is involved in 80% of all chemical industrial processes, and by some measures it contributes to approximately 35% of the world's GDP (Armor, 2008). However, controlled tuning of catalytic activities still remains difficult. Therefore, investigating the mechanism underlying heterogeneous catalysis and achieving tunable catalytic activities of materials has been an important focal point of research at the confluence of materials science and chemistry for a long time.

Nano-materials, especially nano particles of transition metals and their oxides have been widely applied in industrial catalysis and have demonstrated excellent catalytic efficiency (Bell, 2003). The contrasting behaviors of materials at the nano-scale and in bulk form hinges on two effects that depend on the dimensionality of materials: the *Surface Effect*, and the *Quantum Effect*[*]. The surface effect is based on the fact that surface atoms typically have a lower coordination and therefore feature unsaturated

[*]Based on the classification of Roduner (2006b)

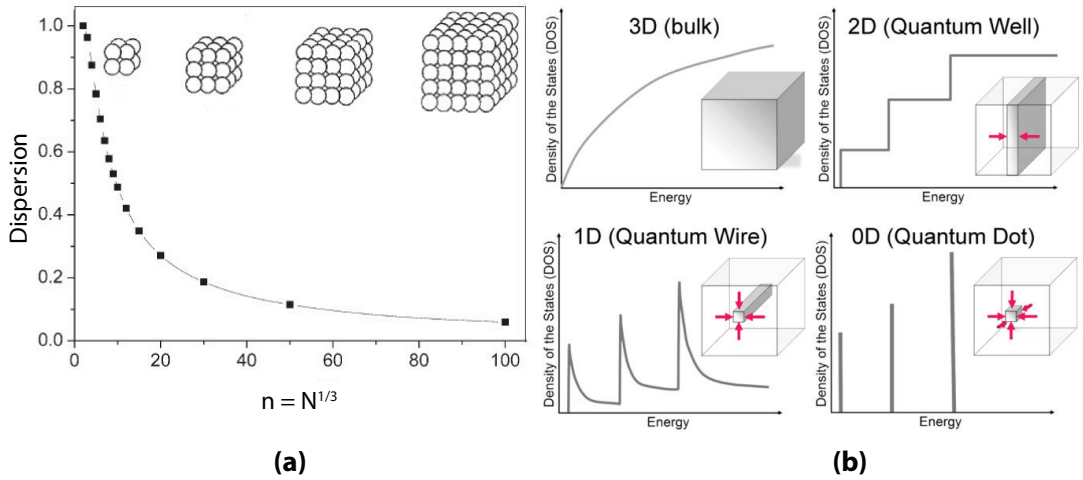

Figure 1.1: (a) Evolution of surface-to-volume ratio as a function of n for cubic clusters up to n=100, where n is the number of atoms along one edge. The structure of the first four clusters is displayed (captured from (Roduner, 2006a)). The inverse correlation between the surfaceto-volume ratio and the material size is visible here. (b) Evolution of the electronic DOS for different materials dimension for cubic clusters (captured from (Mino et al., 2013)). When the dimension is reduced, the electronic DOS becomes more and more discrete.

bonds. Consequently, surface atoms are less stable than atoms in the interior. For this reason, atoms on surfaces have a strong affinity to form bonds with adsorbate molecules. Since the surface-to-volume ratio (the fraction of surface atoms from the total number of atoms) is inversely related to the size of a particle (see Figure 1.1 (a)), the smaller a particle the larger the portion of atoms on the surface, and the stronger the bonding strength between the surface atoms and the adsorbate molecules. The quantum effect refers to the case where the valence electrons are delocalized, yet still confined by the physical boundaries of the material. If the material size is getting close to the *de Broglie* wavelength of the valence electrons, quantum effects become prominent. Quantum confinement of valence electrons will result in a discrete distribution of the electronic density of states (DOS) (see Figure 1.1 (b)). In this case, size variation will lead to a redistribution of valence charge, which can strongly modify the interaction strength between the adsorbate molecules and surface atoms (Ma et al., 2007). There have been many experimental studies regarding the size

effect on the chemical activity of nano-materials (Valden et al., 1998; Wilson et al., 2006; Joo et al., 2010). One notable example is gold (Valden et al., 1998). In the bulk it is one of the most chemically stable elements, yet it becomes very active towards CO oxidation in nano-cluster form.

Since most heterogeneous catalytic processes involve reactions at surfaces, detailed studies of the catalyst surface are necessary to acquire fundamental understanding of these reaction processes. Unfortunately, industrial catalysts are normally very complicated because they consist of small solid particles with poorly defined composition and morphology, dispersed on various supporting materials (Bell, 2003; Erti and Freund, 1999). As a result, there are too many unknown variables that could play a role in determining the catalytic properties of these particles. In order to narrow down the number of variables and to single out the most dominant parameters that are amenable to control, it is necessary to identify simple model systems for in-depth study. Well-ordered single crystalline surfaces are a good option, because their structure may be varied by choosing different surface orientations (Erti and Freund, 1999; Ertl et al., 2008, p. 833). Moreover, by introducing defects and by modifying the crystal's chemical composition, the morphology of the surface may be tailored to bridge the "materials gap"[†] between the model systems and the actual catalyst. These model systems, as well as their interaction with gaseous molecules, can be studied in great detail using the well-established suite of techniques that the field of surface science has developed over decades. Some of these will be introduced in Chapter 3. Unfortunately, most of these techniques can only be applied at very low pressure whereas actual catalysis typically occurs at atmospheric or even much higher pressures. The term "pressure gap" (Cant et al., 1978; Engel and Ertl, 1979; Over et al., 2000) has been coined to describe the mismatch of environments in fundamental research and applications. Nonetheless, investigations conducted on a simple platform

[†]The "materials gap" is due to the fact that many fundamental studies use model systems (e.g., single crystals) that cannot represent the complex structure of a supported catalyst.

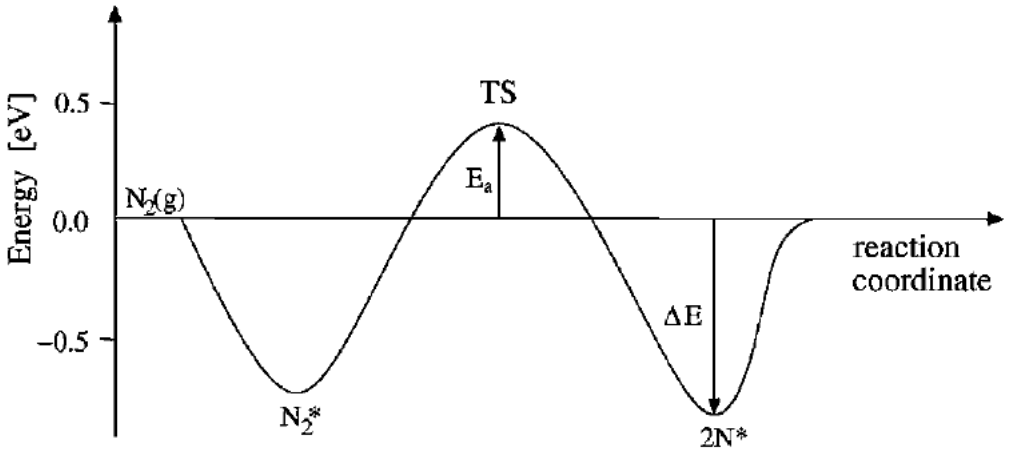

Figure 1.2: Calculated potential energy diagram for N_2 activation at a Ru step. The molecular (N_2^*) states, as well as the transition state for dissociation (TS), are indicated. The asterisk means that the corresponding species are adsorbed on the surface. The rate of dissociative adsorption is determined by the transition state energy, E_a, while the stability of the dissociated product is given by the chemisorption energy, ΔE. (from Nørskov et al. (2002))

in a "clean" and controlled environment do provide crucial information on how the basic interactions govern chemical reaction processes happening on the surface. This could help us understand the behavior of real catalysts without addressing the "pressure gap", for instance by verifying ideas developed for chemical reactions under industrial conditions (Stoltze and Nørskov, 1985; Over et al., 2000; Ertl, 2002).

Even with an appropriate model system, one still needs to identify the key parameters that one should focus on in order to understand and effectively tune the catalytic activities. Qualitatively, the interaction between the catalyst and reactants should be "just right" to facilitate catalysis. It should neither be too weak nor too strong. If the interaction is too weak, the reactants will fail to bind to the catalyst and no bonds will be broken and reformed. If the interaction is too strong, the reaction products will fail to desorb from catalyst. This "just right" idea is embodied in the so-called Sabatier principle (Rothenberg, 2008, p. 65), which can normally be depicted using a "volcano plot" (Dahl et al., 2001; Nørskov et al., 2002; Rothenberg, 2008,

p. 65). In heterogeneous catalysis, which is widely applied in industrial synthesis of chemicals such as hydrogen and ammonia (Chorkendorff and Niemantsverdriet, 2006), the reaction occurs at the boundary of two different phases, and it typically starts with the adsorption of reactant molecules from the gas or liquid phase onto the surface of a solid catalyst. The interaction between the reactant and the catalyst perturbs, specifically, the activation barrier for dissociation E_a and the stability of the intermediates as quantified by the chemisorption energy of the intermediate species ΔE (see Figure 1.2). In this case, a good catalyst corresponds to low activation energy and weak bonding of intermediates. However, it turns out that these two values are often correlated, and the best catalyst is normally a compromise of the two (Nørskov et al., 2002).

Since the reactant-catalyst interaction is determined by the electronic structure of the surface, modifying the surface electronic structure of a catalyst is an effective way to manipulate the activity of catalytic materials. There have been many experimental and theoretical attempts following this spirit, including doping with different atoms (Besenbacher et al., 1998), introducing active sites (Chen et al., 2005), varying the size and dimensionality of the catalysts (Ma et al., 2007), and tuning charge transfer processes between the catalyst and its support (Cooper et al., 2005). Theoretically, the underlying physics is expressed within the d-band model proposed by Norskov (Hammer and Nørskov, 1995b, 2000; Bligaard and Nørskov, 2007), which will be explained in Chapter 2. Here, the molecule-surface bonding strength on transition metal surfaces is strongly influenced by the coupling between the molecular energy levels and the metal d-band.

Our focus in this dissertation is mainly concentrated on size effects by tuning the thickness of Ru and Pd thin films. Both Pd and Ru are widely used catalysts in various chemical processes in industry (Grubbs, 2005; Nielsen et al., 2013; Ertl et al., 2008, p. 2296 and 2503). Both transition metals are also good catalysts for car

exhaust gas treatment via oxidation reactions (Over et al., 2000; Wang et al., 2003; Ertl et al., 2008, p. 2296). An understanding of the physical mechanisms underlying changes in activity as a function of control parameters such as size is therefore of fundamental importance. We will study the effect of thin film thickness variation on the chemical properties of ruthenium and palladium thin films with respect to oxygen adsorption. The bonding between oxygen and the metal surface plays an important role in the oxidation reactions of exhaust gas molecules (Ertl, 2002). A fundamental understanding of size effects in Ru and Pd could thus aid in a controlled tuning of the catalytic activity of these industrially relevant materials.

1.2 Overview of the dissertation

In this dissertation, we will investigate the chemical properties of ruthenium and palladium thin films with respect to oxygen adsorption. In Chapter 2, we will first present the theoretical models that are relevant to describing the chemical reactivity of thin films surfaces. In Chapter 3, we will discuss the experimental techniques applied in this research. Chapter 4 discusses the growth of ruthenium thin films and their chemical properties. We will show that it is difficult to obtain pure and atomically smooth Ru thin films on a Pd(111) substrate. Instead, we find that Pd diffuses to the surface of the Ru film, thus forming a Ru/Pd surface alloy that is very inert with respect to oxygen adsorption. The oxygen adsorption does not show any clear thickness dependence. In Chapter 5, we will describe the growth of palladium thin films and their chemical properties. We will show that pseudomorphic palladium thin films can be formed on the Ru(0001) surface at room temperature. Interestingly, while bulk Pd is reactive towards oxygen, Pd(111) films below five monolayer are surprisingly inert to oxygen. This observation is fully in line with the d-band model prediction. A corresponding theoretical explanation within the framework of d-band model will be provided. Finally, in Chapter 6, an outlook of future research will be presented.

Chapter 2

Theoretical background

One of the long term aims of surface science is to manipulate the properties of surfaces with the goal of designing new functional materials such as catalysts. In this respect gaining an understanding of the important physical properties of a surface that determine its chemical reactivity is imperative. As mentioned in the previous chapter, the breaking and formation of chemical bonds are the key elementary processes in catalysis. In this chapter we will discuss details about the interaction between the adsorbate molecule and the metal catalyst.

2.1 Electronic structure of the surface

* As discussed in Chapter 1, most catalytic processes involve reactions at the surface, and the atomic and electronic structure of the surface may strongly affect the reactant-catalyst interaction. Therefore, we first discuss the surface electronic structure.

The electronic band structure of a metal surface is significantly modified due to the loss of translational symmetry along the perpendicular z direction. In this case, the

*This section is inspired by Zangwill (1988); Groß (2007); Michaelides and Scheffler (2010); Vanderbilt (2013)

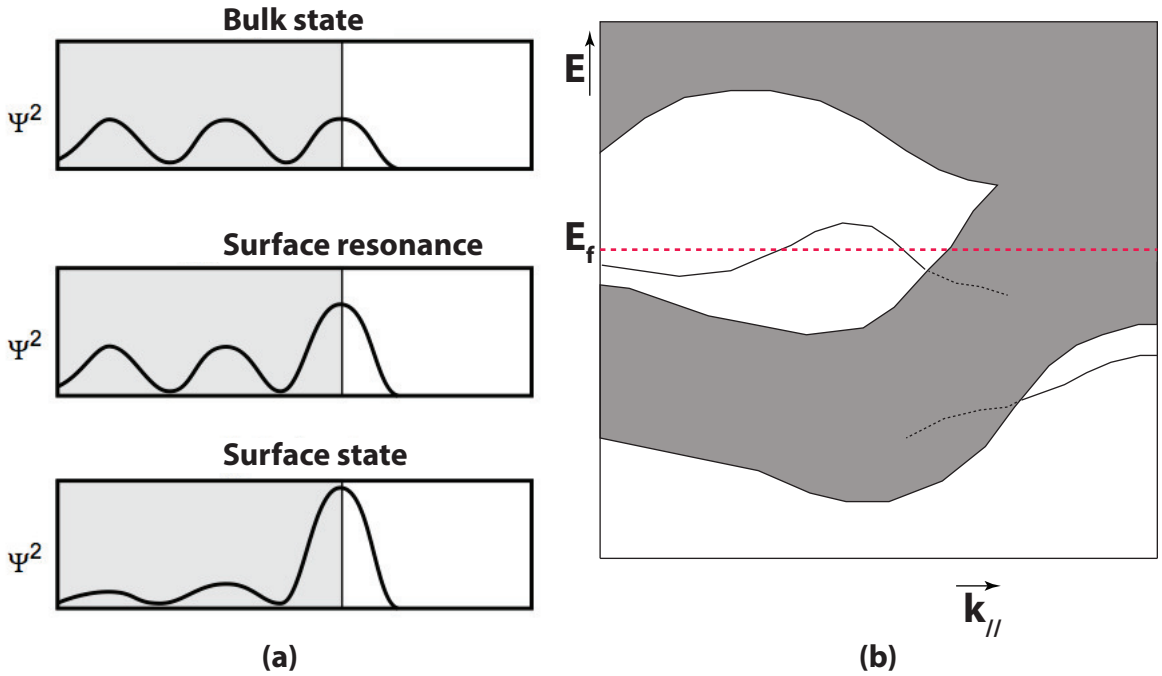

Figure 2.1: (a) Possible electronic states present near the surface region: bulk state, surface resonance, and surface state(captured and modified from Michaelides and Scheffler (2010)). (b) Surface states (solid line) are located in the band gap of the metal while surface resonances (dashed lines) overlap with the bulk continuum (gray). The gray area represents the projection of the bulk bands onto the surface plane.

wave number k_z for the Bloch wave is no longer a good quantum number. Due to the translational symmetry breaking, new solutions to the Schrödinger equation may exist. The corresponding wavefunctions, or "surface states" are localized at the surface, and the corresponding energies are located inside the forbidden zones or "band gaps" of the bulk band structure (see Figure 2.1 (b)). Surface states have a complex k_z and hence, the associated electron density decays exponentially away from the surface (see Figure 2.1 (a)). Inside the bulk, k_z is real, and the wave function is oscillatory and undamped. Due to the lower coordination of the surface atoms, surface states typically have smaller band width when compared to the bulk states. In addition to the surface states, there could also be some states that have a high amplitude at the surface but are degenerate with the bulk continuum. These are generally denoted as surface resonances (see the middle figure of Figure 2.1 (a) and

the dashed line in Figure 2.1 (b)).

Due to the low coordination of surface atoms, the local density of states (LDOS) at the surface will be narrower than the DOS in the bulk. For catalytically relevant transition metals, the d-band contribution to the DOS, which is already narrow in the bulk, features relatively sharp peaks. For transition metals with a more than half filled d-band, this narrowing results in an upward shift (see Appendix B.3 for detailed derivations) of the d-band center (Lischka and Groß, 2002). The d-band model then predicts (see Section 2.5.2) higher reactivity.

2.2 Thermodynamics at the surface

[†] DFT calculations can provide with us a microscopic picture of the atomic and electronic structure of the surface. However, phenomena at larger length and time scale, such as the morphology and structure of the surface, and the distribution of different chemical species on the surface at certain temperature and pressure, also affect the chemical properties. All of these phenomena are affected by thermodynamic conditions, and these should be taken into account.

Under defined (T, p), the appropriate thermodynamic potential to consider is the Gibbs free energy G, which is minimized when the system reaches a thermal equilibrium state at constant pressure and temperature. The saturation coverage of adsorbed gas atoms on the surface can be determined by analyzing G as a function of the coverage. Consider a simple system of a solid phase in contact with a molecular gas phase. The Gibbs free energy can be expressed as

$$G_{surf} = G - G_{solid} - G_{gas}, \tag{2.1}$$

[†]This section is inspired by Hondros and Seah (1977); Zangwill (1988); Rogal (2006); Rogal and Reuter (2006); Groß (2007)

where G is the total free energy of the whole system, G_{solid} and G_{gas} are the free energy of the bulk solid and gas environment, respectively. Assume there are N_s solid atoms and N_g gas atoms on the surface, then the free energy per unit area can be expressed as

$$\gamma(T,p) = (G(T,p,N_s,N_g) - N_s\mu_s - N_g\mu_g)/A, \tag{2.2}$$

where A represents the area of the surface. Here we neglected the almost constant contribution of the bulk and gas phase far from the surface region that is not affected by the surface atom distribution. μ_s is the Gibbs free energy per bulk atom, and μ_g is the Gibbs free energy per gas atom -i.e. these are their respective chemical potentials. Based on the above equation, it is easy to write down the expression of Gibbs free energy per unit area for a clean solid surface.

$$\gamma^{clean} = (G(T,p,N_c,0) - N_c\mu_c)/A, \tag{2.3}$$

where N_c is the number of solid atoms on a clean solid surface. Therefore, the free energy change upon gas adsorption or gas adsorption energy can be expressed as

$$\Delta\gamma^{ad} = (G(T,p,N_s,N_g) - G(T,p,N_c,0) - (N_s - N_c)\mu_s - N_g\mu_g)/A \tag{2.4}$$

If we allow for some simplification and drop some negligible terms, the free energy change upon adsorption can be approximately expressed as (Reuter and Scheffler, 2001; Rogal and Reuter, 2006)

$$\Delta\gamma^{ad} \simeq (E^{tot}(N_s,N_g) - E^{tot}(N_c,0) - (N_s - N_c)E_s^{tot})/A - N_g\mu_g(T,p)/A \tag{2.5}$$

The first three terms can normally be deduced from DFT calculations at 0K. As can be seen in the above expression, the free energy change is linearly proportional to the chemical potential of the gas atoms per unit area, and the slope is the number of gas atoms adsorbed on the solid surface per unit area. For a certain gas chemical

potential value, which is a function of the temperature and the gas pressure, the more negative the adsorption energy, $\Delta\gamma^{ad}$ is the more stable the corresponding adsorption state is. This can be conveniently illustrated in a Gibbs free energy plot (see Figure 2.2). It shows that when the oxygen partial pressure is low, the adsorption

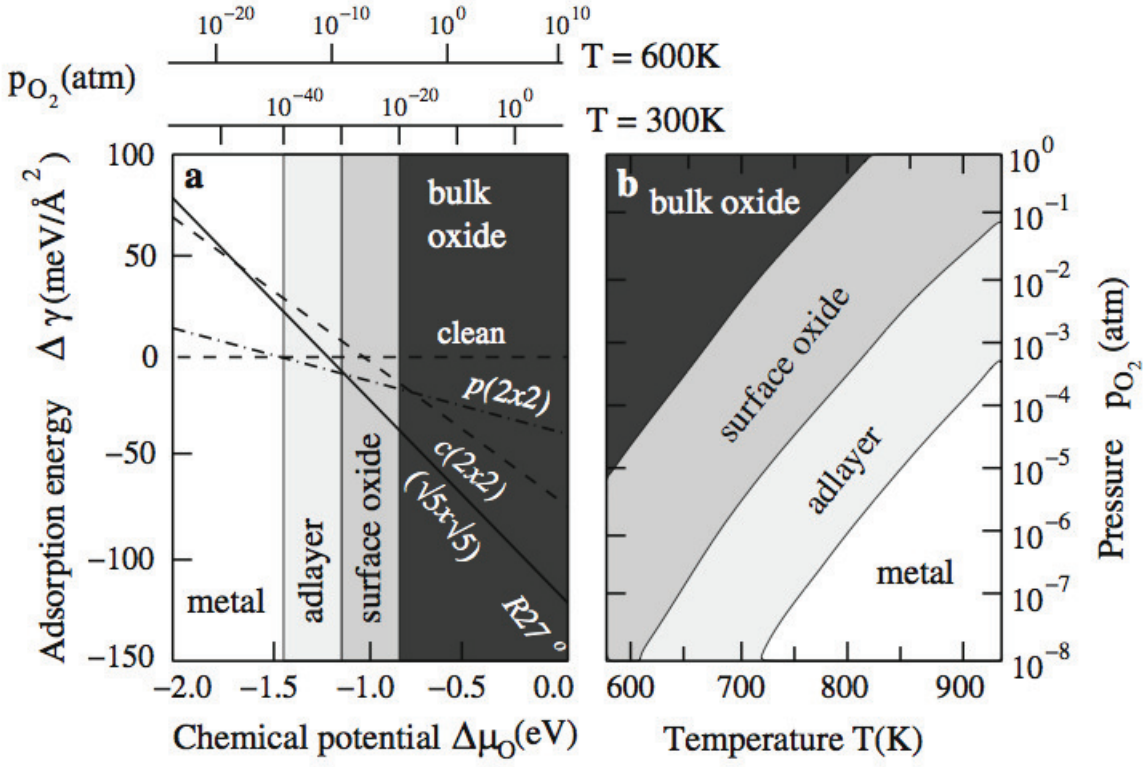

Figure 2.2: Calculated Gibbs fee energy plot (a) and surface phase diagram (b) for the clean Pd(100) surface and several oxygen-containing surface structures (after (Yip, 2007, p. 149)). Here, the chemical potential $\Delta\mu_0$ is the portion of chemical potential that is dependent on temperature and pressure(figures captured from (Groß, 2007, p. 155))

energy of different oxygen adsorbing configurations are all positive. This implies that there is an energy cost associated with adsorption, and these configurations are not favorable as compared to the clean surface. However, when the oxygen partial pressure is increased, the adsorption energy of oxygen decreases until it crosses the dashed horizontal line representing the clean surface, and chemisorption of oxygen starts to become energetically favorable. In Figure 2.2, this first occurs for the $p(2 \times 2)$

configuration. Further increasing of the oxygen pressure favors the $\sqrt{5} \times \sqrt{5}R27^\circ$ ordered palladium surface oxide and eventually bulk palladium oxide is the lowest energy configuration when the vertical line at $\Delta\mu_O \approx -0.8$eV is crossed in Figure 2.2.

At the surface of a solid solution or compound, there is another notable phenomenon that could occur and change the surface properties: segregation. Here atoms of one species diffuse onto the surface of the material to decrease the surface energy. The final equilibrium distribution of solute atoms can be described from thermodynamics as a minimum in the Gibbs free energy of the system as a function of the arrangement of the different atomic species in the sample. Assume that P solute atoms are distributed at random among N bulk lattice sites, and p solute atoms are distributed among n surface sites, each possessing a free energy of e. According to the Mclean model (Hondros and Seah, 1977), the total Gibbs free energy of the system can be expressed as:

$$G = pe + Pe_L - kTln\omega, \tag{2.6}$$

where e_L is the interaction energy of a solute atom in the bulk lattice and the 3rd term represents the configurational entropy associated with the arrangement of the solute atoms in the bulk and the surface, where

$$w = \frac{n!N!}{(n-p)!(N-P)!p!P!} \tag{2.7}$$

Minimizing this energy with respect to p and P will result in a relation yielding the optimized combination of (p,P):

$$\frac{p}{n-p} = \frac{P}{N-P} exp[\frac{e_L - e}{kT}] \tag{2.8}$$

Rewriting the above expression leads to the following relation:

$$\frac{X_b}{X_{b0} - X_b} = \frac{X_c}{1 - X_c} exp[\frac{E_1}{RT}], \tag{2.9}$$

where X_b and X_c are the corresponding concentrations of solute atoms at the surface and in the bulk, X_{b0} is the saturation level of X_b, and E_1 is the surface adsorption energy. Therefore, the fractional surface coverage of solute atoms is $\theta_b = \frac{KX_c}{1+KX_c}$, where $K = exp[\frac{E_1}{RT}]$. This expression implies that segregation is promoted by higher temperature and higher concentration of solute atoms in the bulk lattice. As will be discussed later in Chapter 4, this phenomenon is very common in alloy systems.

2.3 Thin film growth mode

[‡] Since we will discuss the growth of ultra-thin ruthenium and palladium films in Chapter 4 and Chapter 5, it is necessary to discuss some typical thin film growth modes. Similar to the previous section, a surface morphology with minimum free energy is favored. The resulting film morphology will be a compromise of different contributions to the total energy of the system, such as the internal energy, surface and interface energies, and film-substrate interaction due to for example epitaxial strain. Based on experimental observations, typical film growth falls into three categories: island (or Volmer-Weber, VW) mode, layer-by-layer (or Frank-Van der Merwe, FM) mode, and layer-plus-island (or Stranski-Krastanov, SK) mode (see Figure 2.3). The island growth mode occurs when the deposited species are more strongly bound to each other than to the substrate. The layer-by-layer mode corresponds to the opposite situation when the adsorbed molecules or atoms are more strongly bound to the substrate. Layer-plus-island mode corresponds to an intermediate situation.

From a thermodynamic point of view, the surface energy change upon nucleation on

[‡]This section is inspired by Venables (2000); Ohring (2001)

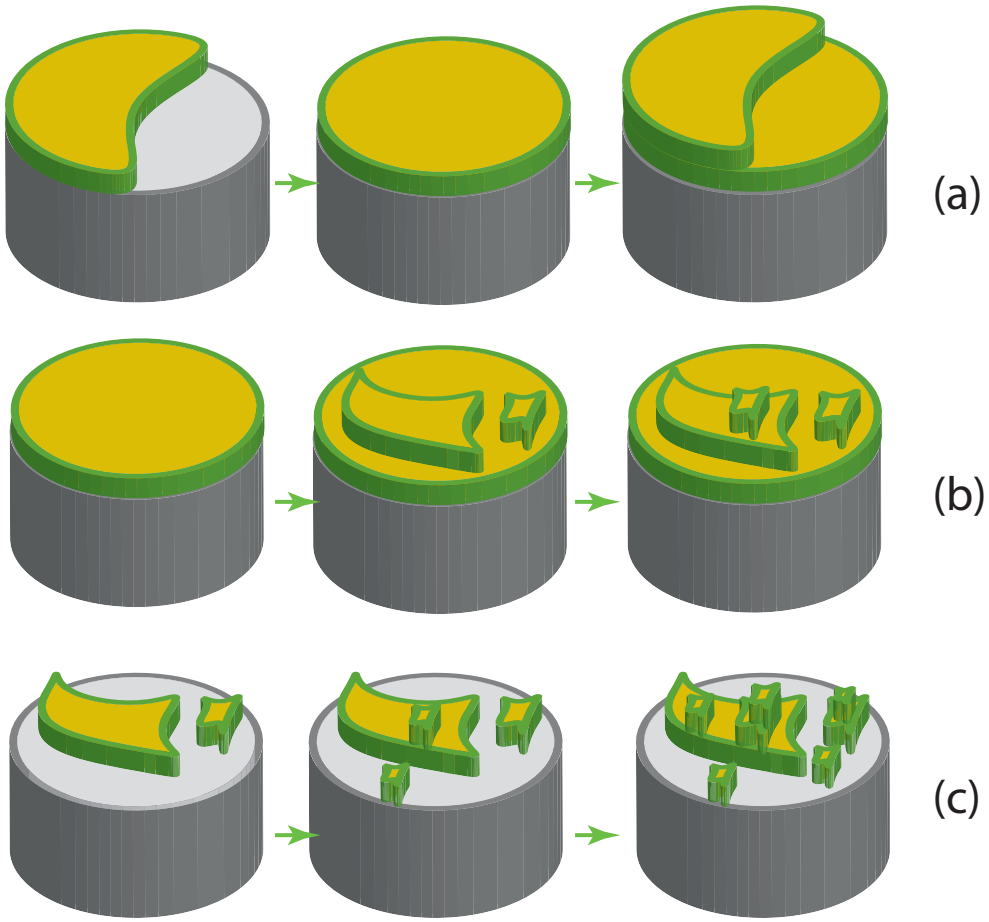

Figure 2.3: Three typical film growth modes: (a) Frank-Van der Merwe (FM) mode; (b) Stranski-Krastanov (SK) mode; (c) Volmer-Weber (VW) mode.

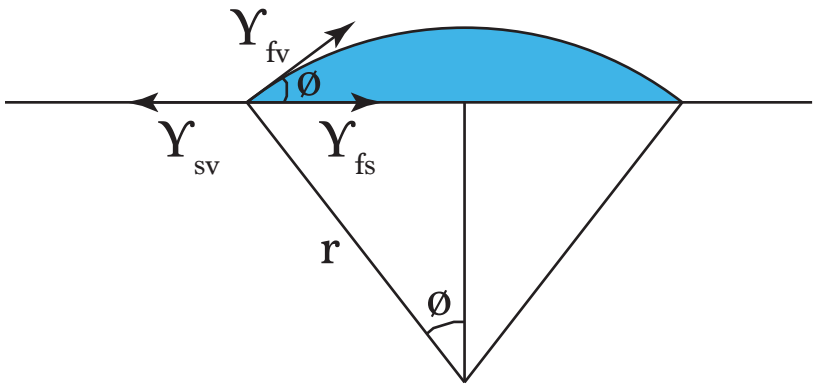

Figure 2.4: Heterogeneous nucleation process on substrate. r represents the cluster dimension. γ_{sv}, γ_{fv}, and γ_{fs} represent the surface tension per unit area for the substrate surface, film surface, and the film-substrate interface.

the substrate can be expressed as

$$\Delta G = a_3 r^3 \Delta G_V + a_1 r^2 \gamma_{fv} + a_2 r^2 \gamma_{fs} - a_3 r^2 \gamma_{sv}, \tag{2.10}$$

where ΔG_V represents the free energy change per unit volume of the deposited material. The three following terms corresponds to the free energy change due to the creation of different surfaces and interfaces, where a_n represent respective surface areas for the different surfaces. Since atoms on the surface always have a higher energy than atoms in bulk due to the reduced coordination (i.e., bonding) of the surface atoms, the creation of a surface always costs energy. The negative sign before the fourth term represents the energy gain due to the decrease of exposed substrate surface area. It can be shown that the free energy change follows the trend in Figure 2.5. It

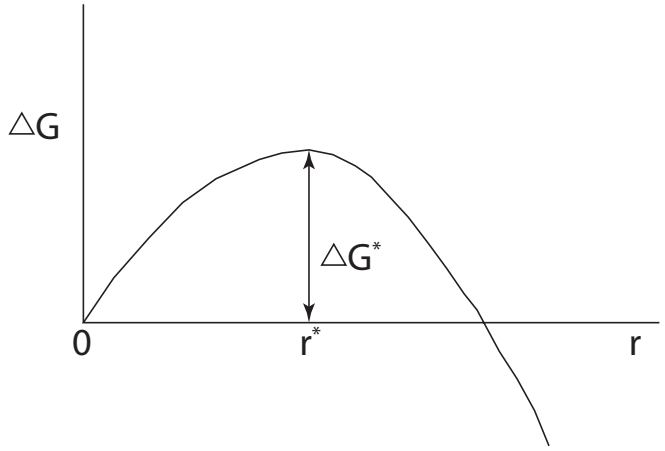

Figure 2.5: Free energy change ΔG in the nucleation process as a function of cluster radius. ΔG^* represents the critical energy barrier for nucleation, r^* represents the corresponding critical cluster size.

is clear that there is an energy barrier for the nucleation process. Clusters whose size is smaller than the critical value r^* are unstable and tend to shrink, while clusters larger than r^* become stable. The energy barrier can be expressed as

$$\Delta G^* = \Delta G^*_{f,h} \{ \frac{2 - 3\cos\phi + \cos^3\phi}{4} \}, \tag{2.11}$$

where $\Delta G^*_{f,h}$ represents a positive pre-factor that depends on the vapor pressure and the surface tension per unit area on the cluster surface.

A force balance of the different surface tensions requires that

$$\gamma_{sv} = \gamma_{fs} + \gamma_{fv}\cos\phi \tag{2.12}$$

For island growth, $\phi > 0$, according to Eq. 2.12, we have

$$\gamma_{sv} < \gamma_{fs} + \gamma_{fv} \tag{2.13}$$

For layer-by-layer growth, $\phi \simeq 0$, therefore (Ohring, 2001)

$$\gamma_{sv} \geq \gamma_{fs} + \gamma_{fv} \tag{2.14}$$

In this case, the surface tension of the substrate surface is comparable or even bigger than that on the film, and it is energetically favorable to completely cover or "wet" the surface with the film. From Eq. 2.11 it is clear this happens when $\phi = 0$. In the special case of homoepitaxial growth $\gamma_{fs} = 0$, and $\gamma_{sv} = \gamma_{fv}$. The layer-plus-island growth is an intermediate situation, where initially the three surface tension components fulfill the relation in Eq. 2.14. However, when the film material accumulates, the interface tension resulting from e.g. a lattice mismatch also grows and eventually the relation in Eq. 2.14 is not valid anymore and the system reverts to the island growth regime.

2.4 Catalysis and heterogeneous catalysis

[§] Catalysis is a process in which the rate of a chemical reaction is accelerated because of the interaction between reactants and other species that are not consumed during the reaction. These species are called catalysts. Catalysts lower the activation barrier

[§]This section is inspired by Deutschmann et al. (2000); Ertl et al. (2008)

of a chemical reaction as explained in Section 1.1 and hence the corresponding reaction rate will be improved. While catalysts improve the rate of a chemical reaction, they do not directly change the chemical equilibrium[¶]. Catalysts are not consumed in chemical reactions, but they do not have infinite life time. They can be poisoned or fouled by the adsorption of reaction byproducts or contaminants so that active catalytic sites become blocked and the catalytic activity decreases. Catalysts can also be deactivated due to thermal degradation or the volatilization of active components (Deutschmann et al., 2000, p. 80). Therefore, reactivation or replacement of the catalyst might be necessary in practice.

Catalysis can be classified into homogeneous catalysis and heterogeneous catalysis, according to the physical phases of catalysts and reactants involved in the chemical reactions. Homogeneous catalysis refers to the case when catalysts and reactants are in the same phase, e.g. both are liquid. Instead, heterogeneous catalysis refers to the situation where catalysts and reactants are present in different forms, such as gaseous reactants and a solid state catalyst. Compared to homogeneous catalysis, heterogeneous catalysis has several advantages. It is much easier to separate the reaction products from the catalyst. Solid state catalysts are generally more stable and have a longer life time. Both Pd and Ru are widely used catalysts in various chemical processes in industry (Grubbs, 2005; Nielsen et al., 2013; Ertl et al., 2008, p. 2296 and 2503), and especially, both of them are good catalysts for auto exhaust gas removal via oxidation reactions (Nieuwenhuys, 1999; Over et al., 2000; Wang et al., 2003; Ertl et al., 2008, p. 2296).

[¶]Note that the resultant changes in reactant and product concentrations will indirectly change the reaction equilibrium.

2.5 Adsorbate-Surface Interaction

In the previous sections, we discussed the electronic properties and thermodynamic aspect of solid surfaces. Since we are interested in the chemical properties of transition metal surfaces which can normally be probed from the adsorption of gas molecules, it is also necessary to go through some of the basic theoretical models describing the adsorbate-surface interaction.

2.5.1 The Frontier Molecular Orbitals

[‖] In solid state physics, the electronic structure of solid can be described as a set of energy bands, based on the consideration of translational symmetry of the atomic lattice and description of the electronic motion in terms of delocalized Bloch wavefunctions. On the other hand, from the chemists' perspective, there is another equivalent representation of a band structure in which the energy band in the solid can be considered as a large number of densely distributed hybridized molecular orbitals (Hoffmann, 1987, 1988b). From this perspective, we can start describing the molecule-surface interaction from a simple scenario of molecule-molecule interaction.

The interaction between two molecules can be analyzed, starting from their energy level diagrams. Using second order perturbation theory, the interaction energy, can be expressed in a way that depends on the orbital overlap and energy separation between the corresponding levels as (Griffiths, 2005)

$$\Delta E = \frac{|H_{ij}|^2}{E_i^0 - E_j^0} \tag{2.15}$$

For molecule-molecule interaction, and according to the number of electrons involved,

[‖] This section is inspired by (Hoffmann, 1987, 1988a,b; Groß, 2007, p. 130).

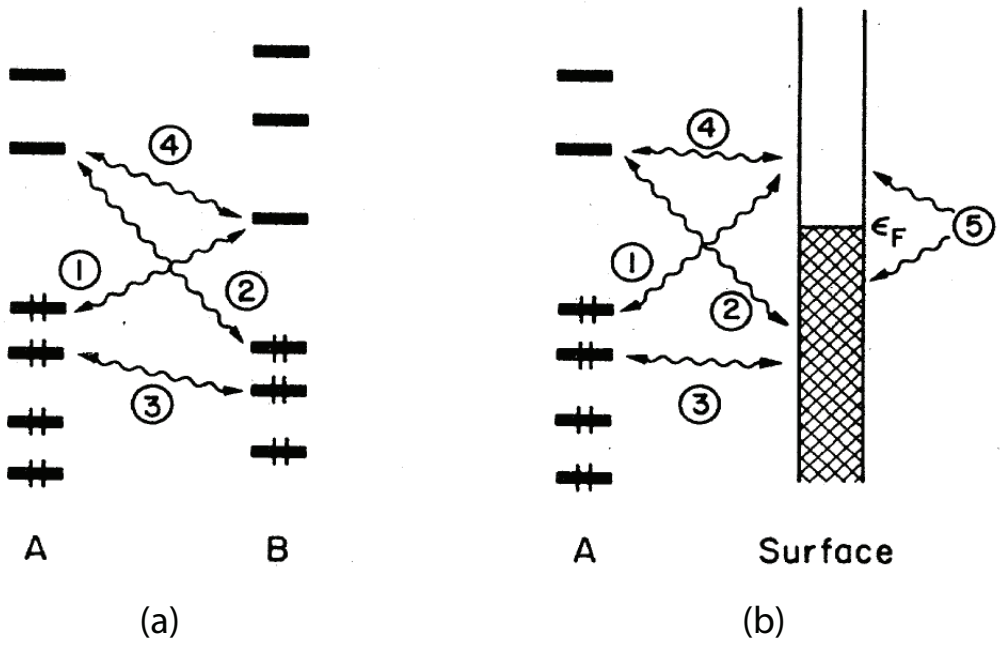

Figure 2.6: Frontier molecular orbitals involved in the molecule-molecule interaction and molecule-surface interaction (Hoffmann, 1988a). Four categories of molecular orbital interactions are indicated based on the number of electrons involved in the interaction. 1 and 2 are two-electron interaction, 3 is four-electron interaction, 4 is zero-electron interaction. 5 in Figure (b) represents the interaction between occupied and unoccupied levels in a solid, details will be explained in following text.

the interaction can be classified into four categories, see in Figure 2.6 (a). The two-electron interaction scheme (1&2) can lead to bonding. Here, hybridization of the two levels will split the original levels into a lower lying bonding state and a higher-lying anti-bonding state. The two electrons will fill the bonding state, which provides a net energy gain. Hence, the interaction stabilizes the new molecular band. The upward shift of the anti-bonding level exceeds the downward shift of the bonding level. Therefore, if both states are fully occupied as indicated in the four-electron interaction scheme (3) in Figure 2.6 (a) there will be a net repulsive interaction between the two molecules, and no bonding occurs. The hybridized states in interaction (4) will not be filled, therefore it doesn't have direct energetic consequences. According to Eq. 2.15, only two levels that are close in energy and have substantial wavefunction overlap will provide a considerable contribution to the overall bonding. Therefore, the highest

occupied molecular orbitals (HOMO), or a small subset of higher-lying levels, and the lowest unoccupied molecular orbital (LUMO), or some subsets of unoccupied molecular orbitals, dominates the interaction between two molecules. These are defined as the frontier orbitals (Hoffmann, 1988a).

For the molecule-surface system, there are no discrete energy levels corresponding to localized orbitals. In particular, metal surfaces contain a continuous distribution (or band) of delocalized wavefunctions. Nonetheless, one could still classify the interactions in a similar fashion, as long as one extra interaction (No.5 in Figure 2.6 (b)) is taken into account (Hoffmann, 1988a). This interaction is an indirect contribution to the substrate-adsorbate interaction, and originates from the static screening response of the Fermi sea to the formation of the hetero-polar bonds (1) and (2), see Figure 2.6 (b) (Hoffmann, 1988a). Within this framework the energy levels associated with the HOMO and LUMO can be represented by the density of states near the Fermi level. Thus, surface chemical activity should be governed by the local density of states (DOS) near the Fermi level. This model has been successfully used to explain the chemical activity of metal surfaces (Feibelman and Hamann, 1984, 1985; Harris and Andersson, 1985).

2.5.2 The *d*-band model

** Even though the energy gain argument in the model discussed above appears to be quite general in nature, there are examples where materials with a lower DOS near Fermi level are more chemically reactive towards H_2 dissociation than materials with a high local DOS near the Fermi level (Hammer and Nørskov, 1995a). Therefore, instead of focusing on states near the Fermi level, it has been proposed (Hammer and Nørskov, 1995b, 2000; Bligaard and Nørskov, 2007) using first principles DFT calculations, that the deeper lying states and the structure of the entire valence band

**This section is inspired by Hammer and Nørskov (2000) and Groß (2007).

of the metal surface are relevant for the surface reactivity. Despite this additional complexity, they showed that a single parameter, the position of the center of mass of the d-band DOS, E_d, can still be used as a good indicator of the adsorbate-surface interaction.

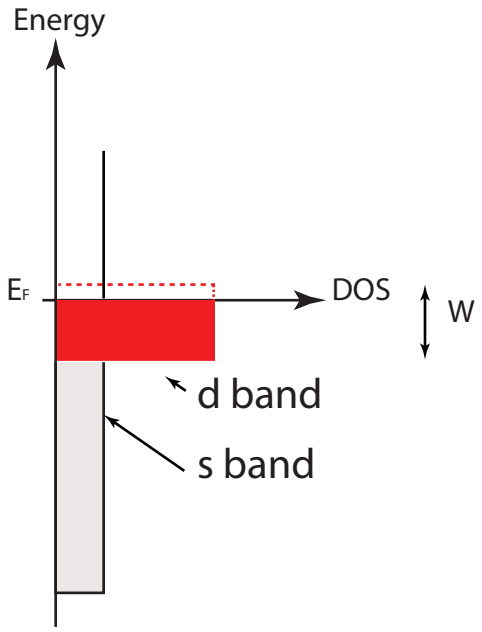

Figure 2.7: Schematic illustration of the density of states of a transition metal with a broad s-band and a narrow d-band with width W around the Fermi level.

Figure B.1 shows a typical density of states for a transition metal. The valence band mainly consists of a broad s-band and a narrow d-band. For many transition metals, the s-band is half filled. Therefore, the d-band with its increasing occupancy along transition metal rows in the periodic table, becomes the main factor determining the density of states near the Fermi energy and hence determines the reactivity of transition metal surfaces. In the d-band model, the adsorbate-surface interaction involves the interaction of the adsorbate molecular levels with both the outermost s and d-states of the transition metal surface. This interaction between the adsorbate and the surface will, if strong enough, result in lower energy bonding states and higher energy anti-bonding states (i.e. the position of the anti-bonding states relative

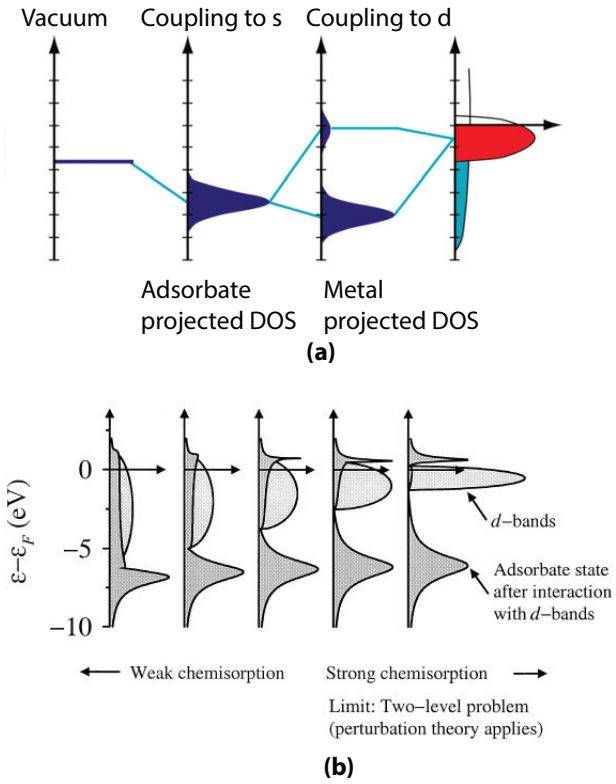

Figure 2.8: (Adapted from Hammer and Nørskov (2000))(a) Schematic illustration of the formation of a chemical bond between an adsorbate valence level and the s and d-bands of a transition metal surface. (b) Change of bonding strength with varying location of the d-band center. The local density of states is projected onto an adsorbate state interacting with the metal d-bands at a surface. The strength of the adsorbate-surface coupling matrix element V is kept fixed as the center of the d-bands ϵ_d moves toward the Fermi level while the width W of the d-bands is decreased to keep the number of electrons in the bands constant. As ϵ_d shifts up, the anti bonding states are emptied above the Fermi level and the bond becomes stronger.[††]

to the Fermi level E_F), similar to our discussion on the frontier molecular orbitals. Again, the interaction between the adsorbate and the surface can be attractive or repulsive. The filling of the anti-bonding states thus directly affects the stability of the chemisorbed molecules on the surface and the reactivity of the surface. The lower the occupancy of the anti-bonding states, the stronger the bonding.

[††]It's necessary to point out that this constant filling assumption is frequently applied to correlate the d-band width with the location of d-band center in order to incorporate the trend of materials' chemical activity within the framework of the d-band model (Kitchin et al., 2004a,b).

We normally describe this interaction between the adsorbate states and the valence electron bands of the transition metal surface in two steps (see Figure 2.8 (a)). First, when the separation between the adsorbate and the surface decreases, the molecular orbitals of the adsorbate molecules will interact with the metal s-band. Due the relatively large band width of the s-band, the resulting renormalized states will be a broad single resonance located slightly below the original adsorbate levels. While this interaction may be very strong, it will not vary much from one metal to another because of the quantitatively similar configuration of the s-band for the different transition metals. In a second step, these renormalized states will further hybridize with the metal d-band. Due to the narrow bandwidth of d-band, the hybridization will result in bonding states and anti-bonding resonances. Since the d-band is always located between the bonding and anti-bonding states, the position of d-band will strongly affect the filling of the anti-bonding states, and consequently the overall bond strength between the adsorbate molecule and the metal surface (see Figure 2.8 (b)). In the case of a single level adsorbate, such as a chemisorbed H atom, the hybridization of the metal d-states with the molecular resonances changes the total adsorption energy as follows (Hammer and Nørskov, 1995a)

$$\delta E_{chem} \sim -2(1-f)\frac{V^2}{\epsilon_d - \epsilon_H} + \alpha_{chem} V^2, \tag{2.16}$$

where E_H and E_d are the energy of H *1s* adsorbate resonance level and the metal d-band center relative to the Fermi level, f is the filling factor of metal d-band, V is the matrix element representing the coupling between the metal d-band and the molecular resonances, α_{chem} is a constant factor. The first term in this expression describes the energy gain due to the hybridization between the renormalized states and the d- states (the factor of 2 accounts for the spin degeneracy). The second term describes the energy rise due to the Pauli repulsion upon the overlapping of these two states.

Chapter 3

Experimental Procedure and Equipment

3.1 Thin film growth in UHV

There are many ways for depositing thin films. Depending on whether or not chemical reactions take place during the deposition process, the process is called chemical deposition or physical deposition. In chemical deposition methods, liquid or gas phase precursors undergo chemical reactions and produce nonvolatile reaction products that are deposited on a suitably placed substrate. Physical deposition is a way to transfer materials physically from the target to the substrate. The target material to be deposited is placed in an energetic environment so that atoms or clusters have enough energy to escape the deposition source, while the substrate is placed in a relatively low energy environment so that the incident atoms or clusters can stick to the substrate surface and form a solid layer. There are several means to inject the energy into the target material, such as thermal evaporation, sputtering, pulsed laser deposition, etc. In our experiments, we used two thermal evaporation methods to grow the Ru and Pd films that are the subject of our studies. These methods are schematically illustrated in Figure 3.1. In the e-beam evaporation method, electrons are emitted

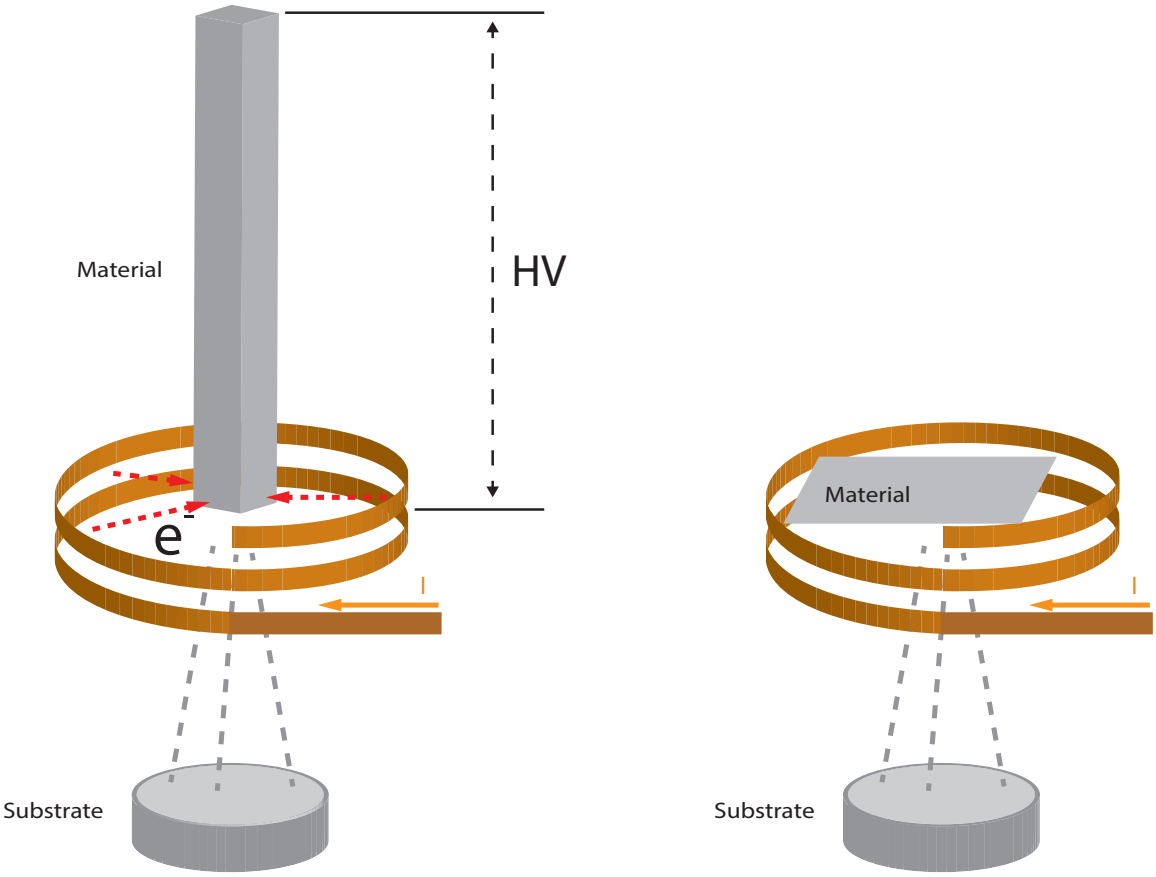

Figure 3.1: Left: E-beam evaporation of a metal from the tip of a metal rod. The tip is bombarded with energetic electrons that are accelerated from the hot filaments towards the tip. Right: thermal evaporation of a source material through direct contact with, or radiative heating by, a hot filament.

from a hot filament and accelerated to the apex of a metal rod (i.e., Pd or Ru) by applying a high voltage between the filament and metal rod (Figure 3.1: Left). The energy deposited by these electrons heats the metal to a temperature where the metal pressure is sufficiently high for attaining a significant rate of evaporation. Because the melting point of ruthenium is as high as 2334 °C, it is very difficult to evaporate. Therefore, a fairly high power evaporator was needed. In our deposition experiments, we used a 600W Tectra e-beam evaporator to facilitate the evaporation (Tectra, 2014). Figure 3.1 Right shows an alternative way for heating the source materials. Here, thermal energy is being generated via Joule heating of the wire

basket. Heat is transferred via direct contact or radiation. Sometimes, elevated substrate temperature are necessary to clean the surface or obtain the desired surface morphology. For metal substrates, elevated substrate temperature can be achieved by e-beam heating as shown in Figure 3.2. As will be shown later, this technique will be applied in the growth of Ru thin films.

3.2 Film thickness calibration

The film thickness is a very important parameter because many important physical and chemical properties are thickness (or size) dependent in the nano scale regime (Valden et al., 1998). Therefore, precise calibration of the film thickness is an important first step. There are many different ways to calibrate the film thickness, here we will briefly review the two main methods used in our experiments.

3.2.1 Quartz Crystal Microbalance

The quartz crystal microbalance (QCM) is a very sensitive mass sensing device. Its basic operating principle rests on the mass sensitivity of the resonant frequency of

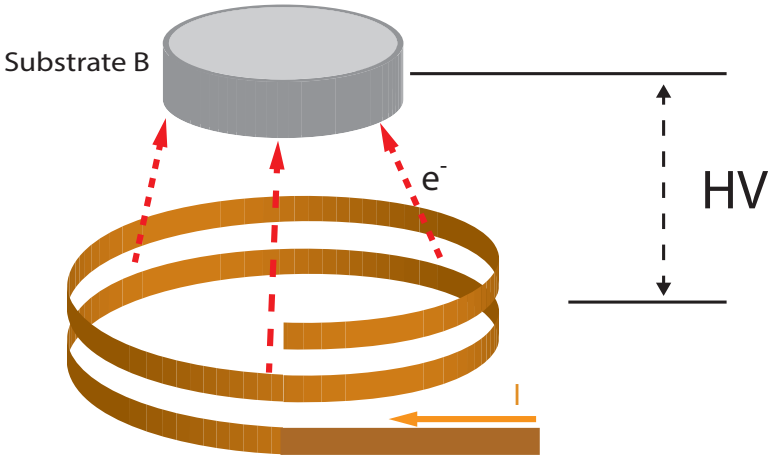

Figure 3.2: E-beam heating of a metal substrate.

an oscillating quartz crystal. The core of a QCM is a piezoelectric AT-cut quartz crystal * sandwiched between a pair of electrodes. When the electrodes are connected to an oscillator providing an AC voltage signal, the crystal will mechanically oscillate at its resonant frequency. This resonant frequency depends on the thickness of the quartz crystal. During normal operation, all the other influencing variables remain constant. Hence any change in mass ΔM due to *e.g.* a thin film being deposited on the crystal, will induce a shift of the resonant frequency Δf. Sauerbrey first showed that the frequency shift is linearly proportional to the mass change 3.1 based on the assumption that the extra mass on the electrodes is evenly distributed and is rigidly attached to the electrodes,

$$\Delta f = -C\Delta M, \tag{3.1}$$

where C is a constant that depends only on the thickness of the quartz slab and on the intrinsic properties of the quartz. For an AT-cut, 10 MHz quartz crystal, C equals 2.25 ng cm^{-2} Hz^{-1} if each side is covered by ΔM (Rodahl et al., 1995). The high sensitivity enables us to detect deposition rates of the order of a monolayer per minute. In fact, the high sensitivity of a QCM has been demonstrated by the detection of a submonolayer hydrogen film on the QCM (Kasemo and Törnqvist, 1980) for frequency

*The crystals used are normally in the form of plates or elements cut from synthetic crystal. The AT-cut crystal is in a plane which makes an angle of 35°15′ to the Z-axis.

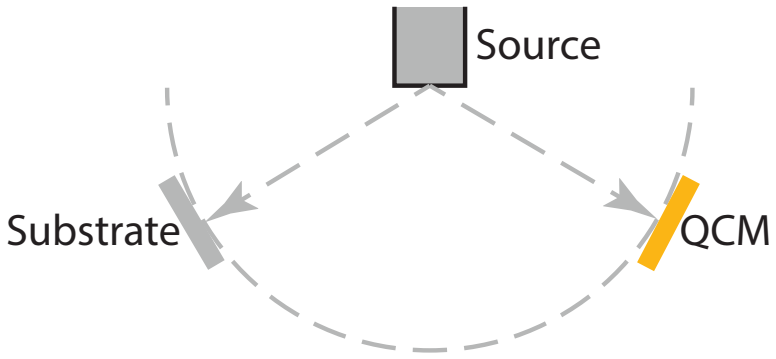

Figure 3.3: Idealized geometry of the quartz crystal microbalance and the substrate in the UHV chamber where the QCM and substrate are distributed symmetrically relative to the evaporation source.

resolution better than 0.01 Hz. In practice, other factors also play a role: the material density, the tooling factor, which depends on the relative position of the substrate and the QCM in vacuum chamber (Figure 3.3), and the Z-factor, which corrects the frequency-change-to-thickness transfer function for the effects of acoustic-impedance mismatch between the crystal and the deposited material. If the QCM, substrate, and the source are positioned in the idealized geometry shown in Figure 3.3, real time calibration of the deposition rate on the substrate can be achieved. Because the tooling factor is not exactly known, QCM data still need to be calibrated. However, once the QCM is calibrated, it provides a quick, sensitive, and reproducible in situ thickness measurement for the thin film growth experiments.

3.2.2 Spectroscopy based calibration

Another way to calibrate the growth rate is to measure the resulting film thickness after growth. This can be done using Auger electron spectroscopy (will be discussed later), which is a surface sensitive chemical fingerprint technique. If the film is uniform in thickness, we can determine the film thickness by monitoring the intensity of a

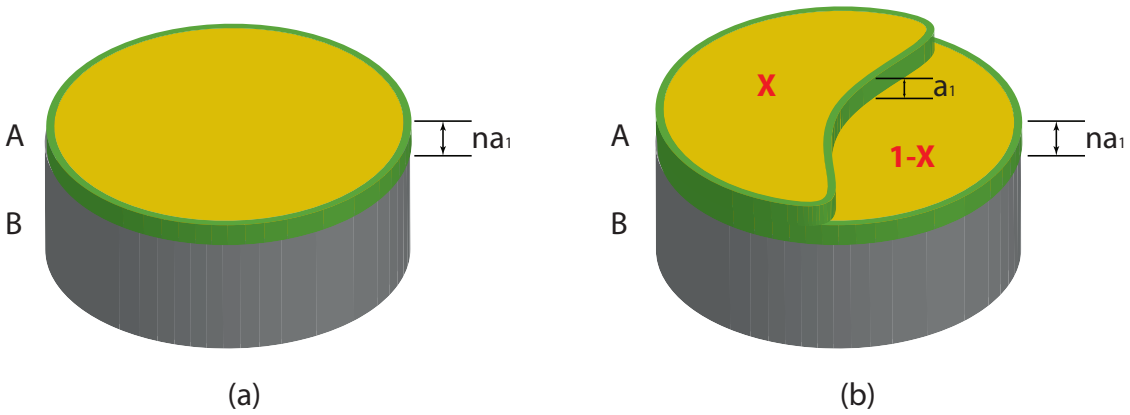

Figure 3.4: (a) n complete monolayers of thin film A grown on substrate B (b) There are n completed layers while the n+1 layer is incomplete. Here x represents the area portion of the submonolayer film and a_1 represents the corresponding lattice constant normal to the film plane.

specific Auger transition in the substrate or overlayer material (Gallon, 1969; Biberian and Somorjai, 1979). For example, in the case of films with uniform thickness, changes of the Auger intensities of the substrate and the deposited material can be modeled as follows.

First, for normal emission, the Auger intensity from a a clean substrate can be expressed as (see Appendix B.1 for a detailed derivation)

$$I_2^0 = I_2 \times \frac{1}{1 - e^{-a_2/\lambda_{22}}}, \tag{3.2}$$

where I_2 is the Auger signal of a single layer of deposited material, I_2 is the Auger signal of one single layer of substrate material, λ_{22} and λ_{21} are the inelastic mean free path of the substrate's Auger electrons inside the substrate and thin film materials, a_1 and a_2 are the lattice constants of the thin film and substrate materials along the growth direction. If there is a thin film of n complete monolayers on the substrate (see Figure 3.4(a)), then the Auger intensity from the thin film and the substrate will be

$$I_1^n = I_1 \times \frac{1 - e^{-na_1/\lambda_{11}}}{1 - e^{-a_1/\lambda_{11}}} \tag{3.3}$$

$$I_2^n = I_2 \times \frac{e^{-na_1/\lambda_{21}}}{1 - e^{-a_2/\lambda_{22}}} \tag{3.4}$$

If the surface layer of the thin film is not completed, i.e. if there are n complete layers while the n+1 layer is still incomplete (see Figure 3.4(b)), the corresponding Auger intensities are:

$$I_1^{n,n+1} = (1-x)I_1 \times \frac{1 - e^{-na_1/\lambda_{11}}}{1 - e^{-a_1/\lambda_{11}}} + xI_1 \times \frac{1 - e^{-(n+1)a_1/\lambda_{11}}}{1 - e^{-a_1/\lambda_{11}}} \tag{3.5}$$

$$I_2^{n,n+1} = (1-x)I_2 \times \frac{e^{-na_1/\lambda_{21}}}{1 - e^{-a_2/\lambda_{22}}} + xI_2 \times \frac{e^{-(n+1)a_1/\lambda_{21}}}{1 - e^{-a_2/\lambda_{22}}} \tag{3.6}$$

Therefore, the increase of Auger intensity upon the accumulation of the $(n+1)^{th}$ layer will be

$$\Delta I_1^{n,n+1} = I_1^{n,n+1} - I_1^n = xI_1 \times e^{-na_1/\lambda_{11}} \tag{3.7}$$

$$\Delta I_2^{n,n+1} = -xI_2 \times \frac{e^{-na_1/\lambda_{21}}(1 - e^{-a_1/\lambda_{21}})}{1 - e^{-a_2/\lambda_{22}}} \tag{3.8}$$

From Eq. 3.7 and Eq. 3.8, it is clear that the Auger intensity originating from the thin film and substrate vary exponentially with the film thickness, but in between two adjacent integer thicknesses the dependence is linear. If the film growth follows the layer-by-layer mode, with a stable evaporation flux, we can estimate the deposition rate during the growth by checking the Auger intensity variation based on these two equations.

Note that the above two equations hold for a strictly layer-by-layer growth mode. To properly analyze the Auger intensities, one has to carefully evaluate the morphology of the film. Due to its ability to image the surface morphology with atomic resolution, Scanning Tunneling Microscopy (STM) is capable of providing the necessary morphology information of the film for the modeling of the Auger intensities. STM can also be used independently to estimate the deposition rate for the thin film growth. As long as the deposition rate of the source is kept stable, one can vary the deposition time and track the film coverage on the surface with STM imaging. We employed both methods here as explained in the next section.

3.2.3 Thickness calibration with STM

As will be shown in Chapter 4, Ru thin film growth on a Pd(111) crystal does not follow a layer-by-layer growth mode. Therefore we will use both the QCM and the STM to calibrate the deposition rate.

We first monitor the evaporation speed with the QCM until the flux from the Ru source is stable. When the flux is stabilized, we grow a sub-monolayer Ru film on the Pd(111) substrate and record the duration of the growth. Subsequently we determine the film coverage with STM by determining the deposited volume of material from the imaged morphology. This last step is repeated for different deposition amounts up to 1 ML (Figure 3.5). By plotting the deposited amount, measured with STM, versus the deposition time, we obtain the deposition rate, which is turn provides the calibration factor of our QCM. Such a plot is shown in Figure 3.6. Once the calibration factor is known, there is no need to repeat the STM calibration, even when the deposition rate is changed.

In our Pd film growth experiments, we used a home-built wire basket source and the preferred location of the QCM was not available. Therefore we used AES and STM after stopping the film growth to determine the deposited quantity of Pd. It

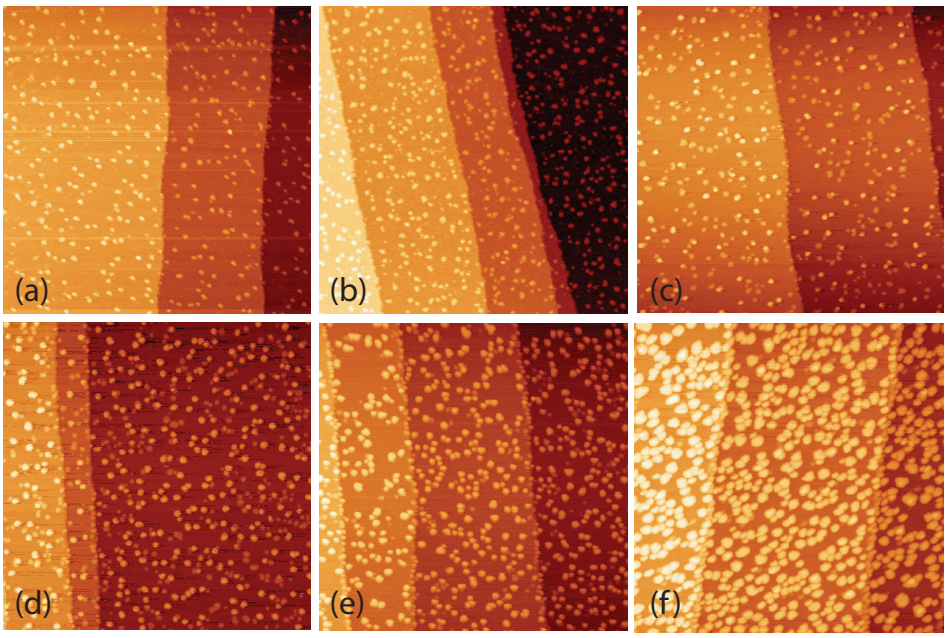

Figure 3.5: A set of sub-monolayer Ru film grown on the substrate at room temperature: (a) 0.06 ML (b) 0.08 ML (c) 0.09 ML (d) 0.2 ML (e) 0.3 ML (f) 0.64 ML.

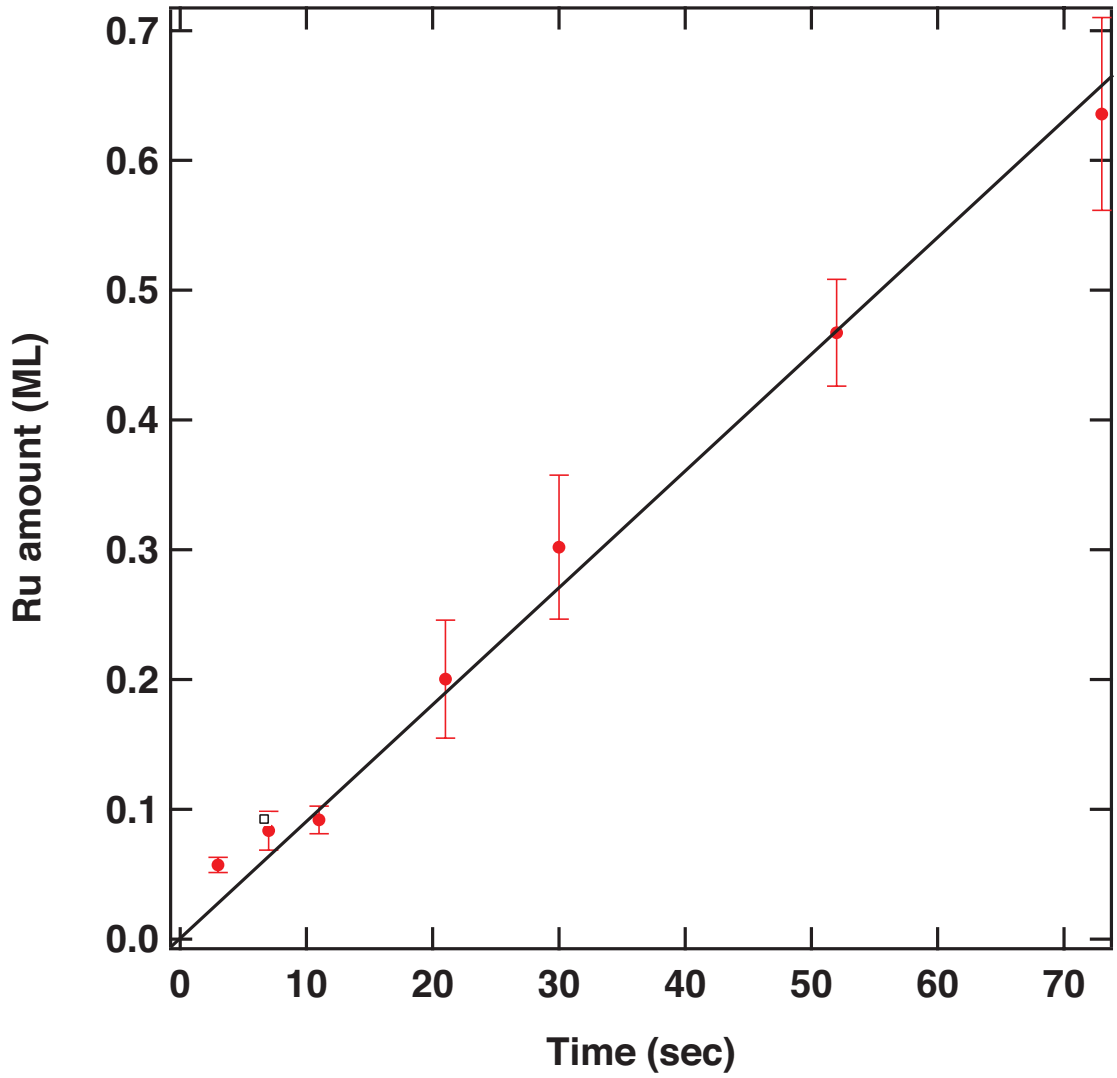

Figure 3.6: For each data point in the graph, the Ru amount was calibrated from STM images acquired at 10 different locations on the sample surface. The error bars represent the standard deviations of the measured amounts.

is known that Pd(111) films on the Ru(0001) substrate can be grown layer-by-layer (Park, 1988), so we can use Auger spectroscopy to determine the growth rate. Using the notation from Section 3.2.2, let I_1 and I_1^n be the intensities of selected Auger peak for one layer and n layers of Pd(111), respectively, and let I_2 and I_2^n be the intensities of the selected Auger peak for a single layer of Ru and for bulk Ru(0001) covered with n over-layers of Pd. For a fractional coverage, i.e., when the coverage is $n + x$, with n being an integer and $0 < x < 1$, the corresponding ratio of the Pd and

Ru Auger intensities can be written as (see Eq. 3.5 and Eq. 3.6)

$$\frac{I_{Pd}}{I_{Ru}} = \frac{xI_1^{n+1} + (1-x)I_1^n}{xI_2^{n+1} + (1-x)I_2^n} = \frac{I_1}{I_2} \times \frac{(1-x)\frac{1-e^{-na_1/\lambda_{11}}}{1-e^{-a_1/\lambda_{11}}} + x\frac{1-e^{-(n+1)a_1/\lambda_{11}}}{1-e^{-a_1/\lambda_{11}}}}{(1-x)\frac{e^{-na_1/\lambda_{21}}}{1-e^{-a_2/\lambda_{22}}} + x\frac{e^{-(n+1)a_1/\lambda_{21}}}{1-e^{-a_2/\lambda_{22}}}} \tag{3.9}$$

We can determine I_1/I_2 by analyzing a sub-monolayer Pd film, where $n = 0$ and x represents the film coverage. The value of x can be determined from STM imaging in conjunction with a measured value for the I_{Pd}/I_{Ru} ratio. With the value of I_1/I_2, we can make a plot of measured value of I_{Pd}/I_{Ru} as a function of Pd film thickness $n+x$. Film thickness can then be determined from this plot based on the experimentally measured value of I_{Pd}/I_{Ru}. Note that by taking the ratio of the Auger intensities, we eliminate instrumental factors that contribute to the measured intensities.

3.3 Characterization techniques

3.3.1 Scanning Tunneling Microscope (STM)

† Figure 3.7 shows a typical setup of a STM system. A probe tip, usually made

†This section is inspired by Chen (1993)

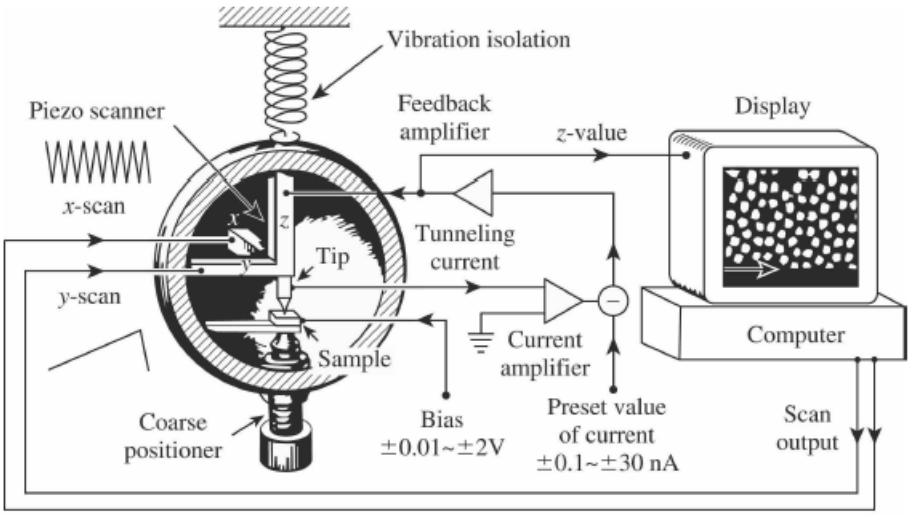

Figure 3.7: Schematic diagram of the scanning tunneling microscope. (Chen, 1993)

of W, Pt-Ir alloy, or gold, is attached to the piezo drive which consists of three piezoelectric transducers controlling the motion of the tip in three perpendicular directions {x,y,z}. Upon applying a voltage, the piezo drive can move the tip over the sample surface. When the tip-surface distance is of the order of several angstroms, the wave functions of the tip and surface atoms start to overlap, so that quantum tunneling may occur(see Figure 3.8(a)). In classical mechanics, this is not possible because the electrons don't have enough energy to overcome the vacuum barrier. In quantum mechanics, however, the behavior of electrons can be described by the wave function. It can be shown that the wave function of electrons originating from the sample side will decay exponentially into the vacuum barrier (Chen, 1993, p. 4) so that there is a finite probability of finding electrons originating from the sample side on the tip. When the work functions of sample and tip are the same, without a bias voltage, electrons in the sample can tunnel into the tip and *vice visa* with equal probability. Hence, there is no net tunneling current(Figure 3.8(a)). When applying a bias voltage V, there will be a net tunneling current (Figure 3.8(b)), which depends on the sample-tip distance according to

$$I \propto e^{-2W\sqrt{2mU}/\hbar}, \tag{3.10}$$

where W is the sample-tip distance, and U is the work function of the sample and tip. Using a feedback loop on the z-piezo drive, we can keep the tunneling current constant while scanning over the sample surface. The tip will then follow the contour of the surface so that we can obtain a height profile of the sample surface by recording the {x,y,z} piezo voltages. Note that STM images don't provide a straightforward interpretation of the atomic structure because the tunneling current is a convolution of the DOS (density of states) of the sample surface and the DOS of the tip (Chen, 1993, p. 23),

$$I \propto e^{-2W\sqrt{2mU}/\hbar} \int_0^{eV} \rho_S(E_f - eV + \epsilon)\rho_T(E_f + \epsilon)\mathrm{d}\epsilon, \tag{3.11}$$

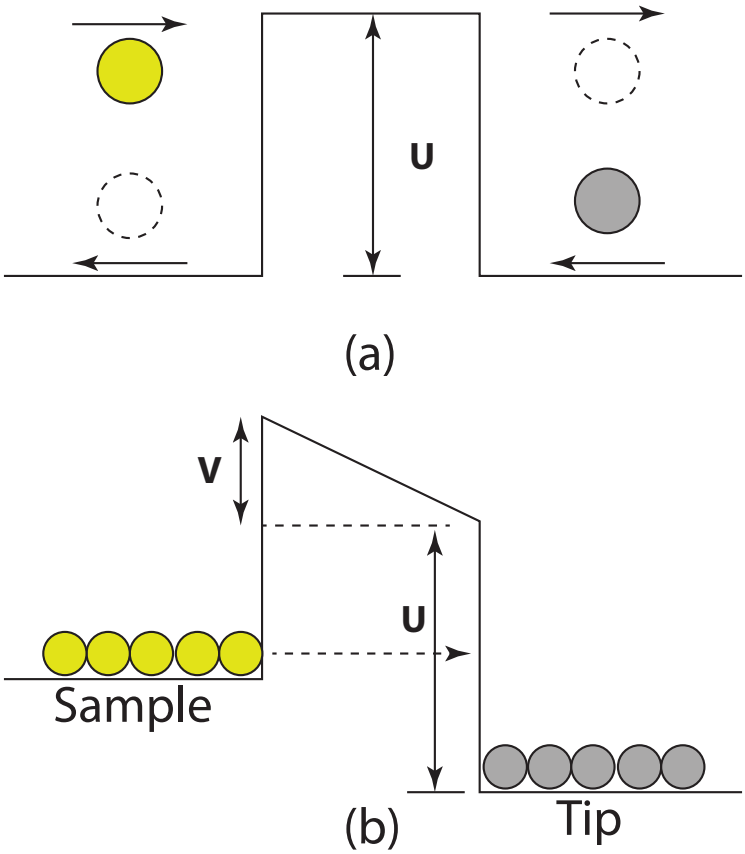

Figure 3.8: (a) Schematic of the quantum tunneling process when the sample and tip have the same work function and there is no bias voltage. U in the image represents the work function, or the height of the vacuum barrier. In this case, there is no net tunneling current, because electrons from the sample and tip can both tunnel to the other side of the barrier with the same probability. (b) The one dimensional sample-vacuum-metal tunneling junction in the presence of a bias voltage V.

where V is the bias, E_f is the Fermi energy, and ρ_S and ρ_T are the density of states of the sample surface and tip, respectively. If the DOS of the tip near the Fermi surface is structureless, then the variation of the tunneling current will be mostly reflecting the variation of the DOS of the sample surface. In that case, STM is actually imaging the local density of states on the sample surface. One example is the STM imaging of the Si(111)-2 $\times$ 1 surface (Stroscio et al., 1987). Two images recorded with opposite bias voltages (+1 V and -1 V) at the same spatial locations showed opposite surface corrugations. These surface corrugations in the STM images were interpreted as the

corrugations of the filled and empty- state surface wave functions.

3.3.2 Low Energy Electron Diffraction (LEED)

[‡] LEED is a commonly used diffraction technique to determine the structure and symmetry of the sample surface, Figure 3.9 shows the typical setup of LEED. Electrons with energies in the range of 20 - 500 eV that are elastically backscattered from a crystal surface will form a Fraunhofer diffraction pattern, which is the Fourier transform of the surface structure in real space. Due to the small value of the electron inelastic mean free path in this energy range, LEED is very surface sensitive.

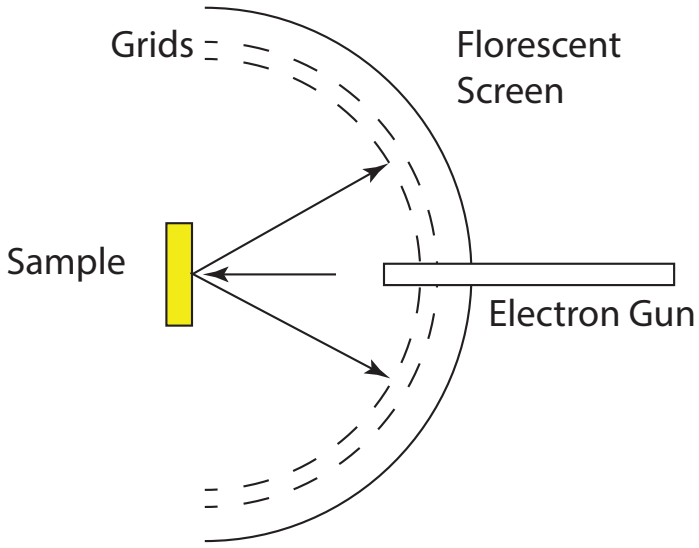

Figure 3.9: A simple schematic of the LEED system

For an ideal 3D lattice structure, the reciprocal lattice consists of a 3D array of discrete lattice points. The Ewald sphere is a useful concept for finding the diffraction conditions. Here, the vector k_i of the incident electron beam is pointing at the origin of the reciprocal lattice, as shown in Figure 3.10. This wavevector defines a sphere of radius k_i. Constructive interference of the elastically scattered electron beams occurs when the Ewald sphere intersects a reciprocal lattice point.

[‡]This section is inspired by Zangwill (1988).

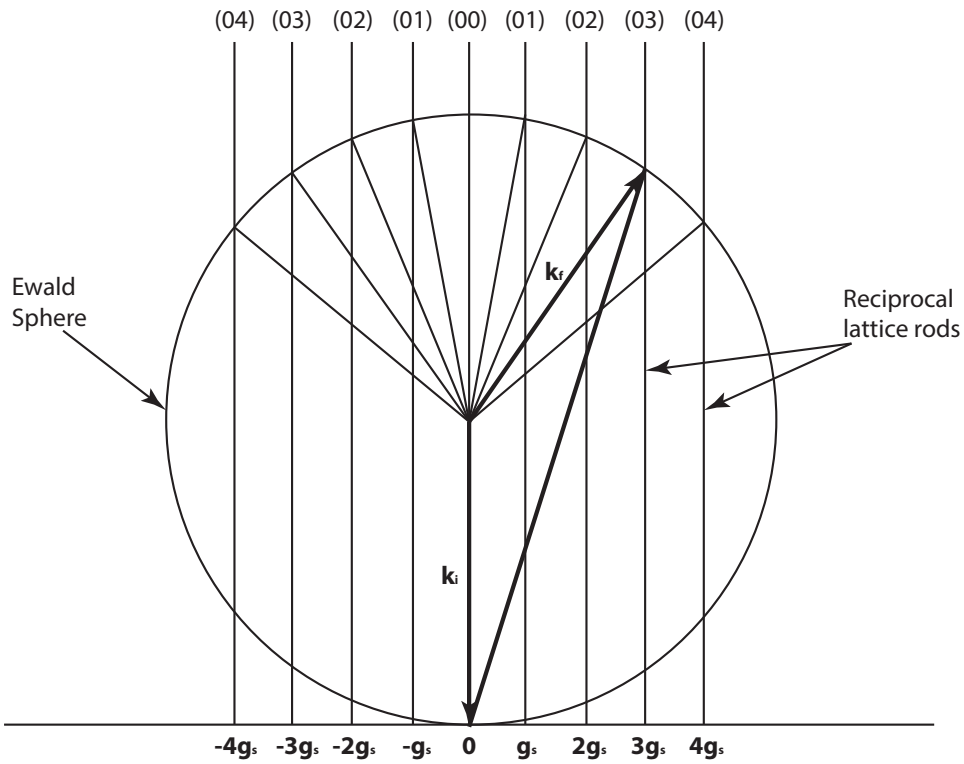

Figure 3.10: The Ewald sphere construction for an electron incident normal to the surface.

For a planar lattice mesh such as a 2D surface structure, the periodicity along the z-direction is lost, and hence, the corresponding Fourier spectrum is totally diffuse. The reciprocal lattice of an ordered 2D lattice thus consists of a discrete set of rods, where the rods are perpendicular to the surface plane. Constructive interference happens when the Ewald sphere intersects the reciprocal rods(see Figure 3.10),

$$(\mathbf{k_i} - \mathbf{k_f}) \cdot \mathbf{g_s} = 2\pi n, \tag{3.12}$$

where $\mathbf{k_i}$ and $\mathbf{k_f}$ are the wave vectors of the incident and scattered electron beams, respectively, and n is an integer number. In our experiments, we will mainly use LEED to verify the symmetry of the sample surface in order to identify ordered phases on the surface.

3.3.3 Auger Electron Spectroscopy (AES)

Auger Electron Spectroscopy is a commonly used elemental analysis technique based on the Auger electronic transition process (see Figure 3.11). In this technique, a high energy (e.g. 2 keV) electron beam impinges on the sample surface. The high energy electrons remove an electron from a core level. Subsequently, an electron from a higher energy level will drop down and fill this core hole. The energy released by this transition is transferred to another electron that is ejected from the atom. The kinetic energy of the outgoing electrons is measured using an electron energy analyzer. It is given by

$$E_k = E_1 - E_2 - E_3 - \phi, \tag{3.13}$$

where E_1, E_2, and E_3 are binding energies of the three energy levels involved in the Auger transition, and ϕ is the work function. Since the orbital energies of the core electrons are unique for a given element, analysis of the energy spectrum of the outgoing electrons can yield information about the chemical composition of the surface.

The core part of an Auger electron spectrometer is the cylindrical mirror analyzer (CMA). The CMA consists of two concentric cylinders (see Figure 3.12). The inner

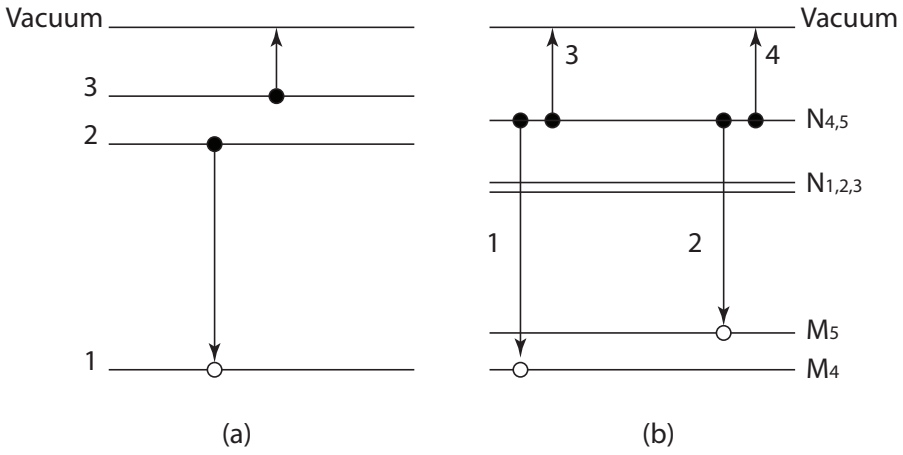

Figure 3.11: (a)A general Auger transition process. (b)Transition 1 or 2 followed by transition 3 or 4 constitute a MNN Auger process.

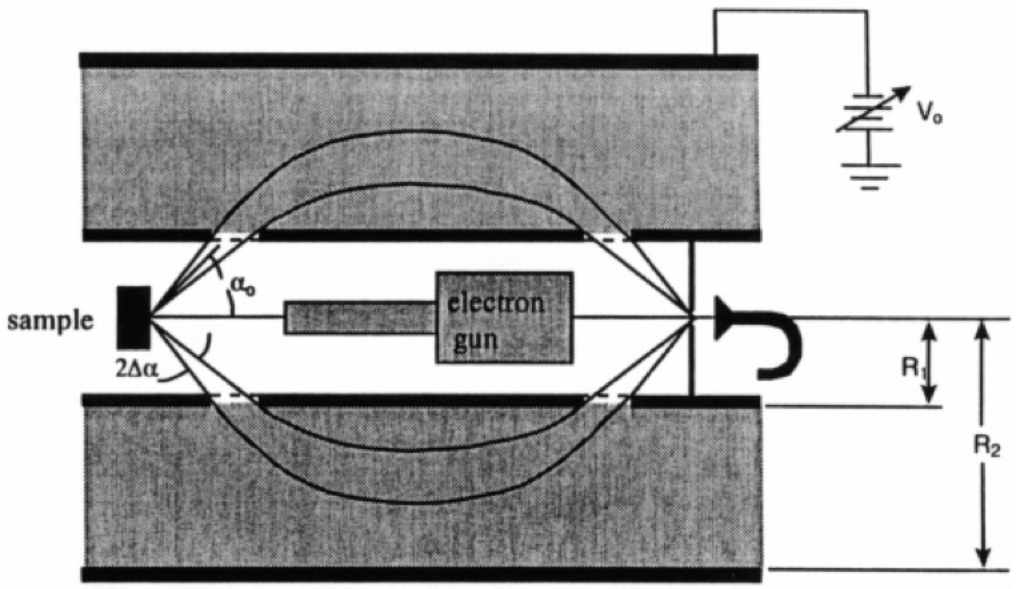

Figure 3.12: Schematic of a cylindrical mirror analyzer (CMA) integrated with a coaxial electron gun (adapted from Narumand and Childs (2004)).

cylinder is grounded, while the outer cylinder is negatively biased which produces an electric field between the two cylinders. Auger electrons emitted from the sample surface will enter the electric field between the two cylinders from an inlet on the inner cylinder and be collected with a detector located at the focal plane as indicated in Figure 3.12. While high energy electrons will impinge on the outer cylinder and low energy electrons will be attracted by the inner cylinder, only electrons with appropriate range of energy values can be finally detected. The energy range can be swept by varying bias on the outer cylinder, and the corresponding energy resolution is determined by the acceptance angle α_0 and the width of inlet $\Delta\alpha$. In practice (Narumand and Childs, 2004)), $\alpha_0 \simeq 42.31°$ and $\Delta\alpha \simeq 6°$ will allow an energy resolution $\Delta E/E$ around (0.3-0.6)%. For our system, the corresponding energy resolution is 0.6% of the electron energy.

Since the Auger current emitted with a given energy from a solid under electron bombardment is much smaller than the secondary electron current back scattered at that energy, it is extremely difficult to measure the Auger current directly. Therefore,

AES is often run in a derivative mode so as to highlight the peaks. Here the electron current arriving at the channeltron detector is modulated but applying a small AC voltage to the outer cylinder of the CMA. The AC modulation voltage is given by $\Delta V = ksin(\omega t)$, and the collected current becomes $I(V + ksin(\omega t))$. From a Taylor series expansion, we obtain

$$\begin{aligned} I(V + ksin(\omega t)) &= I_0 + \frac{dI}{dV} ksin(\omega t) + \frac{d^2I}{dV^2} k^2 sin^2(\omega t) + ... \\ &= I_0 + \frac{dI}{dE}\frac{dE}{dV} ksin(\omega t) + \frac{d^2I}{dV^2} k^2 sin^2(\omega t) + ... \\ &\equiv I_0 + \alpha \frac{dI}{dE} sin(\omega t) + \frac{d^2I}{dV^2} k^2 sin^2(\omega t) + ..., \end{aligned} \quad (3.14)$$

where α is a known constant. With a lock-in amplifier, we can easily detect the 1^{st} order term by tracking the sine signal with frequency ω and amplitude $\alpha \frac{dI}{dE}$. If necessary, we can integrate the measured derivative spectrum to obtain the real Auger intensity. In most cases, one can simply use the peak-to-valley amplitude in the derivative spectrum as an estimation of the Auger intensity, based on the assumption that line shape does not change. In our analysis, we will use the peak-to-valley amplitude in the Auger spectrum.

3.4 The Ultra High Vacuum System

Figure 3.13 is a picture of the ultra-high vacuum (UHV) system used in this work. The system has a base pressure in the 10^{-11} mbar pressure range. The UHV chamber is equipped with a variable temperature STM (VT-STM), a LEED system, a QCM, and a single pass CMA (cylindrical mirror analyzer) for AES. In addition, a mass spectrometer was used to monitor the gas constituents, a sputter gun to clean the sample surface, and an e-beam evaporator for the deposition of Ru films. Evaporation of Pd thin film was done with a homemade W wire-basket containing thin Pd metal pieces, as shown in Figure 3.1.

Figure 3.13: The UHV chamber: (1) STM, (2) LEED, (3) RGA, (4) Sputtering Gun, (5) E-beam Evaporator, (6) Load-lock.

Chapter 4

Growth and chemical properties of Ru thin films

4.1 Introduction

The valence shell electron configuration of the ruthenium atom is $4d^7 5s^1$. Ruthenium has the widest range of oxidation states (Naota et al., 1998), ranging from -2 in $Ru(CO)_4^{2-}$ to +8 in RuO_4), of all elements of the periodic table and exhibits various coordination geometries for each electronic configuration. Therefore, ruthenium has a strong potential to bind to a wide variety of chemical complexes and furthermore exhibits important catalytic properties. Ruthenium based catalysts have been used in various chemical reactions such as olefin metathesis (Grubbs, 2005), water splitting (Duan et al., 2012), and methanol dehydrogenation reactions (Nielsen et al., 2013). Well defined surfaces of ruthenium oxides also have technological value for the reduction of toxic CO (Over et al., 2000) and NO (Wang et al., 2003) in air pollution control. Reducing the dimensions of ruthenium-based catalyst nanoparticles may allow access to other parameters that could be utilized to tune their catalytic properties. In this chapter, we are aiming to prepare atomically flat ruthenium thin films to investigate the thickness-dependent chemical properties of those films with

respect to oxygen adsorption. We will use the Si(111) surface and Pd(111) surface as the substrates for Ru thin film deposition.

It has been shown that under low oxygen partial pressure ($< 5 \times 10^{-5}$ torr), oxygen adsorbs dissociatively on the Ru(0001) surface at room temperature (Mitchell et al., 1994) and reconstructs the surface layer into a 2×2 superstructure up to an atomic oxygen coverage of 0.25 ML (Wintterlin et al., 1997). The oxygen sticking probability decreases with increasing coverage (Stampfl et al., 1996). Upon further exposure, oxygen atoms accumulate up to 0.5 ML. At this coverage, the surface consists of a three domain 2×1 structure, where the 2×1 domains are rotated 120° with respect to one another (Madey et al., 1975). The sticking probability of oxygen decreases to almost zero upon further exposure (Stampfl et al., 1996). Therefore, at room temperature and at low partial pressures, the oxygen distribution on the surface saturates at a coverage of 0.5 ML. Since the saturation coverage of an adsorbate is a typical measure of the adsorbate-surface bonding strength (Alayoglu et al., 2008), we will determine the saturation coverage of oxygen on Ru thin films as a function of the film thickness, and investigate whether or not their chemical reactivity exhibits a significant size or thickness dependence.

4.2 Experimental Procedures

We use the Si(111) and Pd(111) surface as the substrates for Ru thin film deposition. Pd(111) was chosen because the in-plane lattice mismatch between Pd(111) and Ru(0001) is very small (1.5%). Many experiments have shown that atomically smooth metal films on semiconductors can be grown by depositing the metal at fairly low temperature followed by a gentle anneal (Smith et al., 1996; Zhang et al., 1998). This novel growth mode appears to be related to quantum size effects, which provide a thickness dependent contribution to the total free energy of the film (Zhang et al., 1998). The Si(111) surface has an in-plane lattice constant of 3.84 $\mathring{A}$, which

corresponds to lattice mismatch of 29% as compared to the in-plane lattice constant of a Ru(0001) surface. However, lattice mismatching is not always a critical factor for high-quality film growth, as exemplified by the Pb/Si(111) system, which has a large lattice mismatch (Weitering et al., 1992), but also features strong quantum size effects in its growth morphology (Wei and Chou, 2002). We explored Ru film growth on both Si(111) and Pd(111) with the goal of studying its chemical properties as a function of the film thickness.

The Si(111) surface was prepared in UHV by degassing a Si wafer piece at 600°C for a few hours, followed by an anneal at 750°C for 10 minutes, and subsequent flashing up to 1200°C. The Pd(111) surface used in this study was cleaned by cycles of 500 eV Ne ion bombardment at a pressure of 5×10^{-5} torr at room temperature for 30 minutes. The sample was subsequently annealed to 1100 °C for 5 minutes to restore the surface crystallinity. Ru thin films were deposited onto the Si and Pd substrates using e-beam evaporation. The substrate was held at liquid nitrogen or at room temperature. the Ru films were annealed at some elevated temperature. To adsorb oxygen on the Ru surface, we introduced molecular oxygen gas into the UHV chamber using a variable leak valve. The oxygen partial pressure in the UHV chamber was kept between 2×10^{-8} torr and 4×10^{-8} torr as measured with a quadrupole mass spectrometer. Exposure times were varied. The sample was kept at room temperature during the oxygen exposure. The amount of oxygen on the surface was quantified using the peak-to-valley intensity of the oxygen $KL_{2,3}L_{2,3}$ Auger signal, measured in the derivative mode (see Chapter 3).

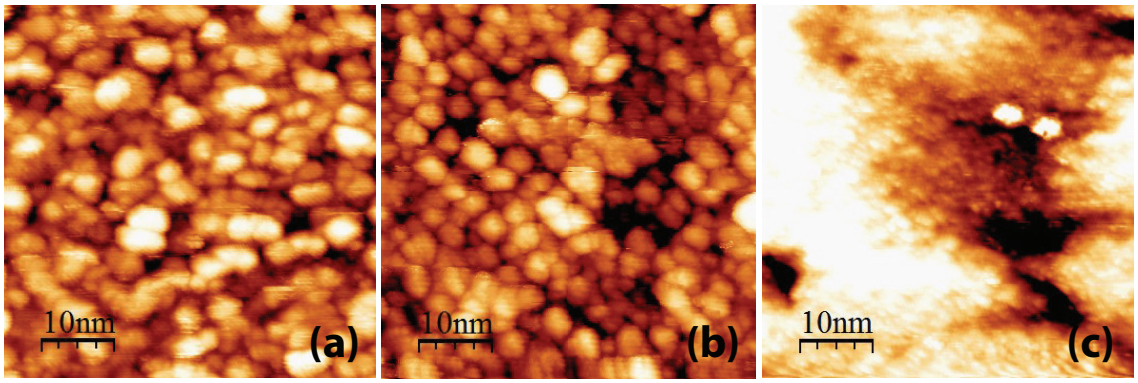

Figure 4.1: Evolution of the film morphology of a 12 ML Ru deposit on the Si(111) surface, as shown in these 50nm×500nm STM images. The images were recorded at room temperature. Panel (a) shows the morphology of a Ru film deposited at −153°C and annealed to room temperature. Panels (b) and (c) show the morphology after annealing to 200°C and 600°C, respectively

4.3 Results and Discussion

4.3.1 Thin film growth on the Si(111) surface

Ruthenium films were deposited on the Si(111) surface at LN_2 temperature and subsequently annealed at 200°C and 600°C for 2 minutes. The surface structure, morphology and chemical composition were studied with LEED, STM, AES, and x-ray photoelectron spectroscopy (XPS). STM images acquired at room temperature indicate that the Ru atoms coalesce into a nano-cluster morphology. This morphology persists even after annealing to 600°C (see Figure 4.1). LEED patterns were not observed for any of the annealing conditions, and XPS spectra of the Si 2p core level indicated that ruthenium silicide forms above 300°C. While the nanocluster morphology may be interesting for catalytic purposes, because of its high surface area, it is not a suitable surface to obtain a detailed fundamental insight into its chemical properties. For this purpose, we turned our attention to the Pd(111) substrate.

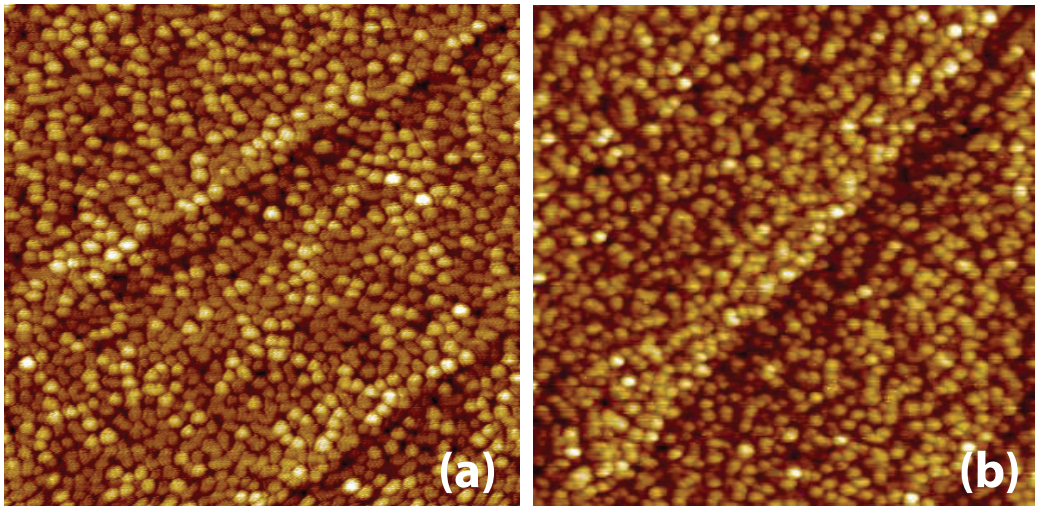

Figure 4.2: 100 nm×100 nm STM images of the surface morphology of 2 ML Ru films. Panel (a) corresponds to deposition and scanning at room temperature, while panel (b) corresponds to low temperature (−130°C) deposition followed by scanning at room temperature.

4.3.2 Thin film growth on the Pd(111) surface

In order to obtain flat films, we used the Pd(111) substrate. This choice was motivated for several reasons. First, the in-plane lattice constant of Pd(111) is 2.75 $\mathring{A}$ which closely matches the 2.71 $\mathring{A}$ in-plane lattice constant of Ru(0001). The in-plane lattice mismatch is only 1.5% which should facilitate epitaxial growth. Secondly, the atomic corrugation of the Pd(111) metal surface is significantly smaller than that of the Si(111)7×7 surface, which may facilitate faster adatom diffusion. Finally, while Pd and Ru may form a dilute alloy at the chosen growth condition, this is not expected to dramatically affect the growth mode because the packing density of the layers remains almost unaffected. These factors suggest that it may be easier to grow smooth films on Pd(111), as compared to Si(111). Ru was deposited onto the Pd(111) surface both at LN_2 temperature and at room temperature. At low temperature, the surface exhibits a nano-cluster morphology similar to that of the Si/Ru system in Section 4.3.1. This morphology persists up to room temperature (see Figure 4.2). In Figure 4.3, we present a detailed evolution of the surface morphology as a function of annealing temperature.

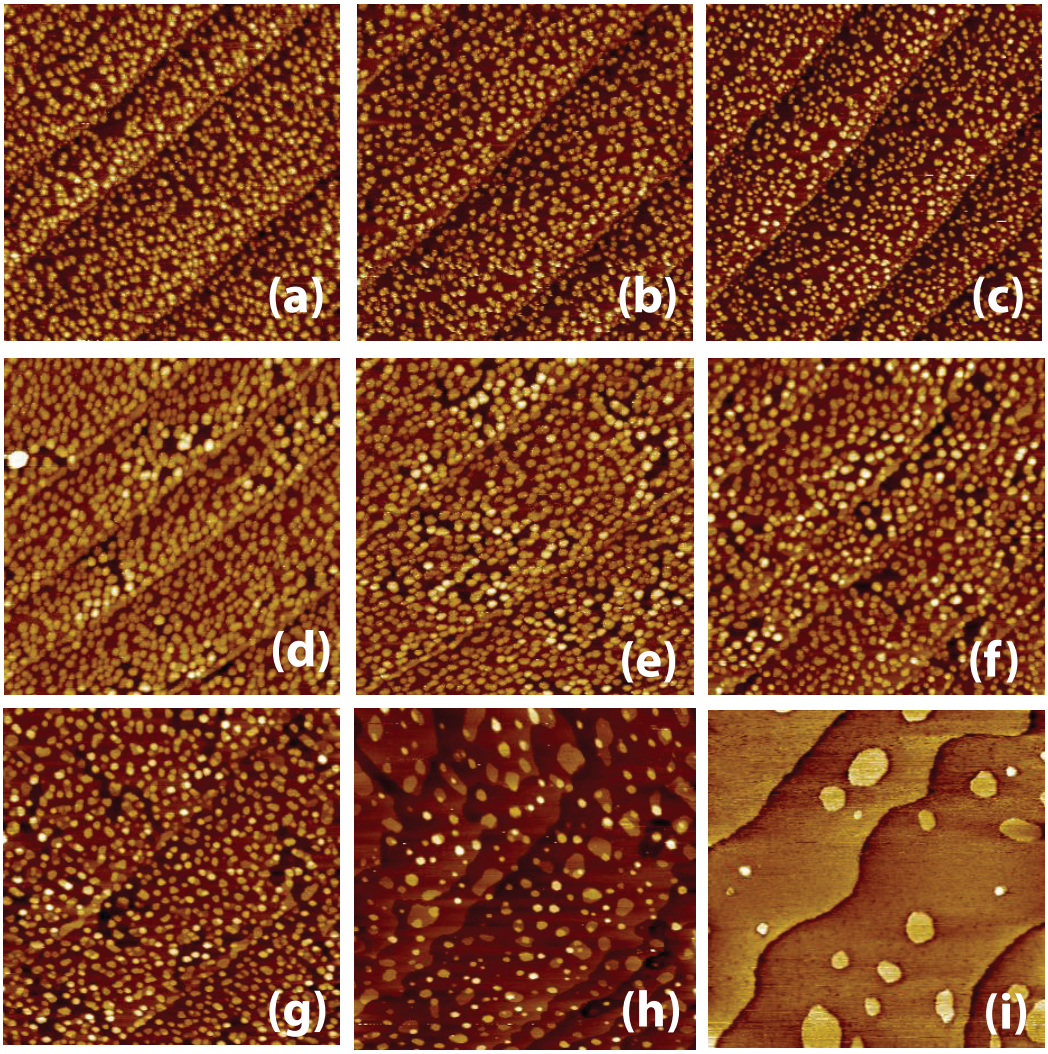

Figure 4.3: Evolution of the surface morphology of a 0.8 ML Ru deposit on Pd(111), recorded with STM immediately following evaporation at room temperature (a), and after a 10 minute anneal at (b) 70°C, (c) 120°C, (d) 180°C, (e) 220°C, (f) 270°C, (g) 320°C, (h) 370°C, and (i) 450°C. The STM image size is 200 nm×200 nm for all panels.

Since the initial deposition amount in Figure 4.3 is less than one monolayer, we expect that the distributed clusters in Figure 4.2 and Figure 4.3 are ruthenium, and that the flat parts in between these clusters represent the bare Pd(111) surface. This is certainly a reasonable assumption for the low-temperature deposition shown in Figure 4.2. As can be seen from the STM images in Figure 4.3, with increased

annealing temperature, starting at 180°C, atoms from the Pd(111) terraces begin to climb to the top of the ruthenium clusters, creating several deep depressions in between the clusters and enhanced brightness of the Pd-decorated ruthenium clusters as can be seen in Figure 4.3 (d). As the annealing temperature further increases, the density of these depressions increases as well until the surface acquires a smooth morphology as shown in Figure 4.3 (h) and (i). The absence of monolayer Ru islands corresponding to the volume of Ru that was deposited on the surface implies that the surface of the submonolayer film is in fact a surface alloy of Ru and Pd atoms.

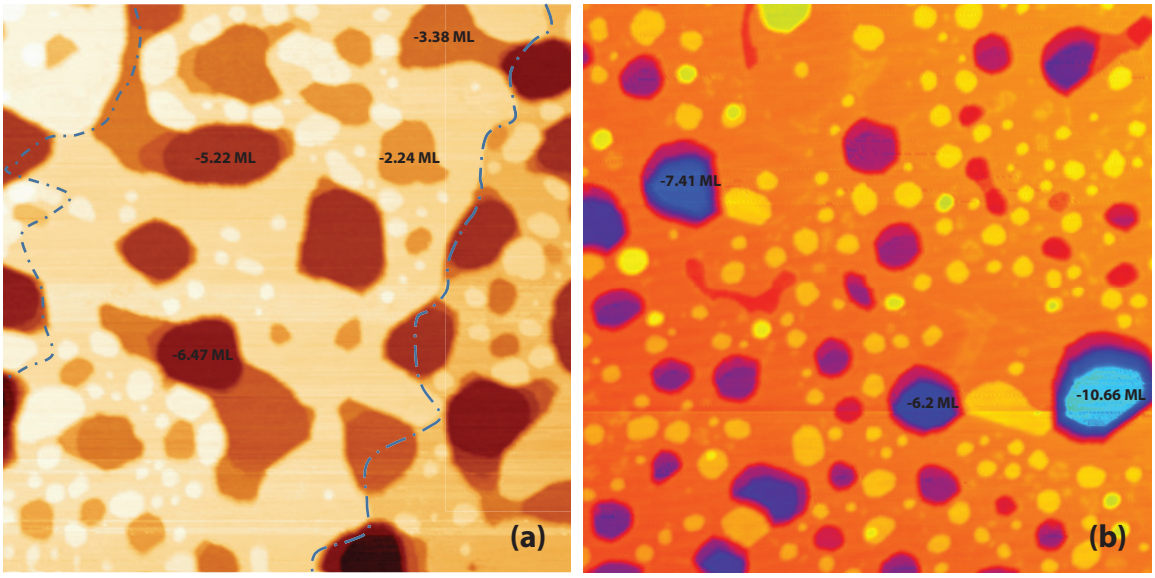

Figure 4.4: Surface morphology of a 3 ML Ru film (a) and a 5 ML Ru film (b), grown at room temperature and annealed to 600°C. Both images are 200 nm×200 nm in size. The heights of the islands and depths of the craters on the surface are indicated.

To study a possible thickness dependence of the chemical properties of the Ru films, we grew ruthenium films with different thicknesses. As shown in Figure 4.4, both 3 ML and 5 ML films show deep holes with depths that are much larger than the estimated film thickness. After a careful calibration of the STM z-piezo, using the well-known step-height of a Si(111) surface, it turned out that the depth of most holes

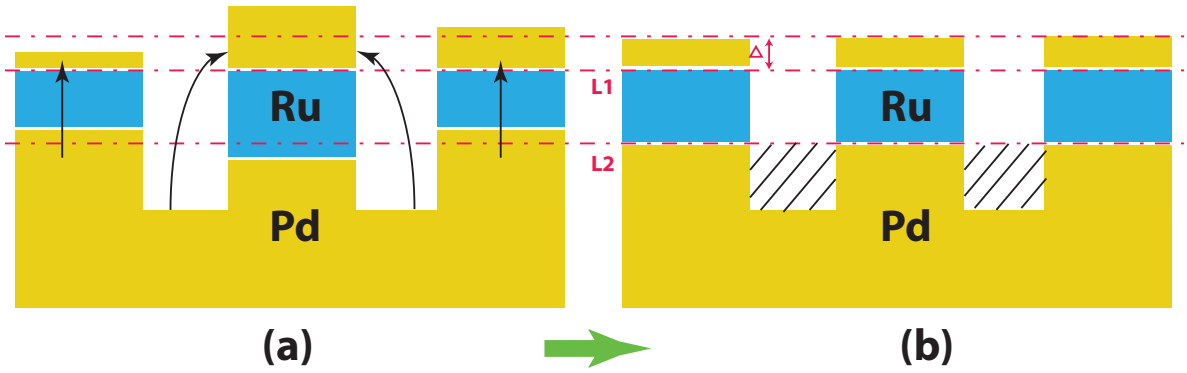

Figure 4.5: (a) Schematic model of the morphology and structure of Ru(0001) films grown on Pd. Arrows show the possible pathways of Pd atom segregation to the surface of the Ru film. (b) Simplified Ru/Pd stacking model with an evenly distributed Ru thin film and evenly distributed surface Pd atoms. *Yellow color*: Pd atoms; *Blue color*: Ru atoms.

does not correspond to an integer number times the Ru lattice constant. Consistent with the presence of exposed Pd in these holes, the opening of the holes at 600°C is accompanied by a very significant increase of the Pd $M_4N_{4,5}N_{4,5}$ Auger intensity (330 eV). However, the total surface area in the deep holes visible in the STM images is not able to explain the magnitude of the increased Pd Auger intensity, indicating that this increase cannot solely be attributed to the exposure of the clean Pd substrate. Instead, our observations provide strong evidence that Pd atoms are extracted from the substrate and diffuse onto the Ru film surface, thus causing an anomalously large increase of the Pd Auger intensity and providing an explanation for the observed hole depths. Hence a Ru-Pd alloy is formed on the Ru film surface during the annealing process. This is consistent with the results obtained from submonolayer Ru coverages discussed above. Theoretical and experimental results in the literature confirm this strong tendency of Pd segregation to the surface in the Pd-Ru system (Ruban et al., 1999; Bergbreiter et al., 2011).

In order to analyze the concentration of Pd atoms on the Ru film, we approximate the film structure as schematically presented in Figure 4.5. In reality the surface concentration of Pd atoms (as well as the Ru film thickness) may not be entirely

uniform, although STM images indicate that the total film thickness does not vary significantly for more than 1 or 2 ML (see Figure 4.5(a)). In order to simplify the calculation, we assume that both the thickness of the Pd surface layer and the Ru film underneath are evenly distributed as shown in Figure 4.5(b). We then set two levels L_1 and L_2 representing two different height in the histogram of the z-profile of the surface, and adjust two levels in the STM images (with the *SPIP* software from Ormicon) such that the material volume above L_1 equals the hatched volumes in Figure 4.5(b). We then take the material volume above L_1 as a measure of the surface concentration of Pd. Using this surface Pd concentration, we calculate the expected ratio of the Ru and Pd Auger peak intensities according to the model in Figure 4.5(b) (see Appendix A.1 for the Matlab code of the corresponding calculation). We can check the validity of this model by comparing the calculated and measured values of the Auger intensity ratio. From these data we conclude that the concentration of Pd atoms on top of the Ru islands is approximately 0.6 ML, which is independent of the Ru film thickness up to 5 ML.

4.3.3 Chemical properties of Ru thin films

Here, we proceed to evaluate the reactivity of the Ru films towards oxygen. In these experiments, the relative ratio of 510 eV oxygen $KL_{2,3}L_{2,3}$ and the 273 eV Ru $M_{4,5}N_{4,5}N_{4,5}$ Auger lines is used to track the amount of chemisorbed oxygen. Surprisingly, with oxygen exposures varying by over five orders of magnitude, from 1L* to 500,000L at room temperature, the 3 ML Ru film (which was annealed at 600°C, see Figure 4.4) does not reveal any oxygen related feature in the Auger spectra. Also, the LEED pattern lacks any evidence for the presence of an oxygen-induced surface reconstruction. This is very surprising because both bulk Ru(0001) and bulk Pd(111)

*1L is short for 1 Langmuir. It corresponds to an exposure of 10^{-6} torr during one second.

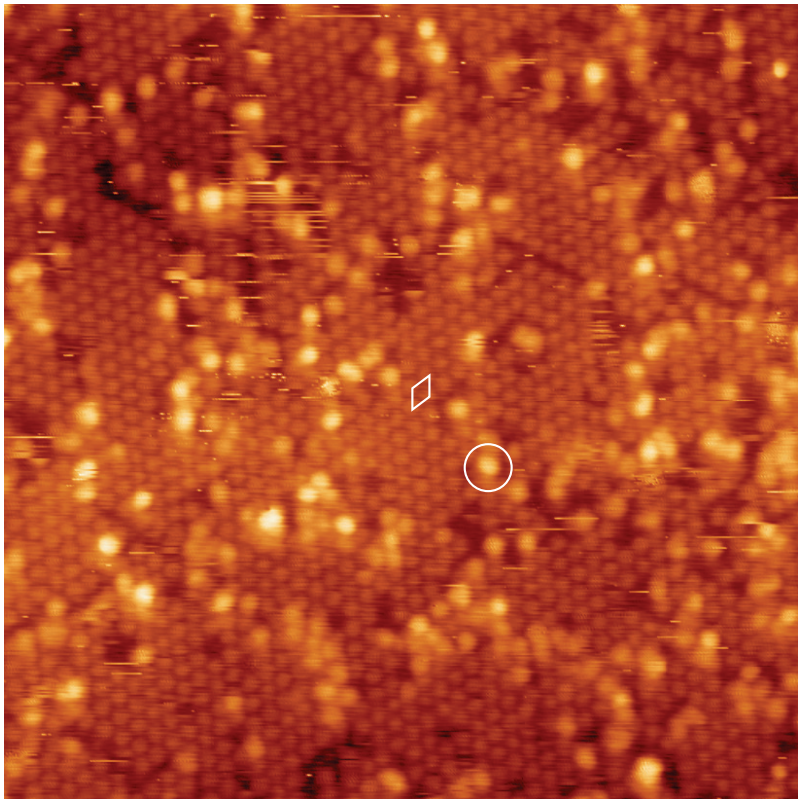

Figure 4.6: 24.9nm × 21.06nm STM image of the Ru(0001) bulk surface exposed to 1L oxygen at room temperature. Scanning parameters: (-1V, 1nA). The small white parallelogram in the image corresponds to the 2×2 unit cell of ordered oxygen atoms distribution on the surface, which is twice the periodicity of the Ru atoms. There are also some bright features on the surface marked by the white circle in the image, which could correspond to disordered oxygen atoms.

surfaces are known to be very active for the dissociative adsorption of O_2 molecules at room temperature. They typically form a 2×2 reconstruction due to the ordering of oxygen atoms on the surface (Conrad et al., 1977; Wintterlin et al., 1997).

To check whether we are able to reproduce the literature results, we adsorbed oxygen at room temperature on bulk Ru(0001) and Pd(111) surfaces. On the Ru surface, all the literature results are well reproduced: the Auger spectra reveal the presence of the oxygen $KL_{2,3}L_{2,3}$ Auger line, the LEED pattern shows a 2×2 reconstruction , and atomic-resolution STM images reveal the presence of chemisorbed oxygen atoms

(see Figure 4.6). For the Pd(111) surface, while we did observe a $\sqrt{3} \times \sqrt{3}$ LEED pattern following 20 L of oxygen exposure, showing that Pd indeed oxidizes, the Auger spectra did not shown any oxygen features. The latter could perhaps be explained by electron-induced desorption, which has been observed on Pd (Voogt et al., 1997).

To investigate the influence of the film thickness on the surface chemical reactivity, oxygen adsorption experiments were performed on ruthenium films of different thickness. We studied films with thicknesses of 3 ML, 5 ML, 10 ML, and 20 ML, and the oxygen exposure ranged from 0 to 20L. The surface concentration of Pd atoms on the ruthenium films was controlled as best as possible by controlling the surface hole coverage and the relative ratio of the Pd-330eV $M_4N_{4,5}N_{4,5}$ Auger intensity versus the Ru-273eV $M_{4,5}N_{4,5}N_{4,5}$. This was done by chosing the appropriate parameters for the annealing treatment. Figure 4.7 shows the O/Ru intensity ratio or oxygen 'uptake' from the AES measurements as a function of exposure to molecular oxygen. For all thicknesses considered here, the AES data did not show any oxygen intensity up to 20L exposure, and the LEED images lacked any evidence of an oxygen-induced reconstruction. We also studied oxygen adsorption on a bulk-like 100 ML thick Ru film at room temperature. This measurement provides a consistency check to make sure that the adsorption characteristics of bulk Ru(0001) are recovered. The 100 ML thick film did not contain voids that were observed on the thinner films in e.g., Figure 4.4, and AES measurements did not detect any measurable Pd concentration. These results indicate that the large thickness of the film prevented the Pd from diffusing through the film to the surface, which allows us to evaluate the chemical reactivity of the thick Ru film without complications arising from Pd segregation. Contrasting with the thin film results, adsorption studies on the 100 ML Ru film reproduces the literature results for adsorption on bulk Ru(0001). This, in turn, confirms the notion that the lack of oxygen adsorption on ultrathin Ru films is solely a consequence of a thickness-dependent phenomenon, possibly related to electronic confinement, lattice strain, or Pd segregation.

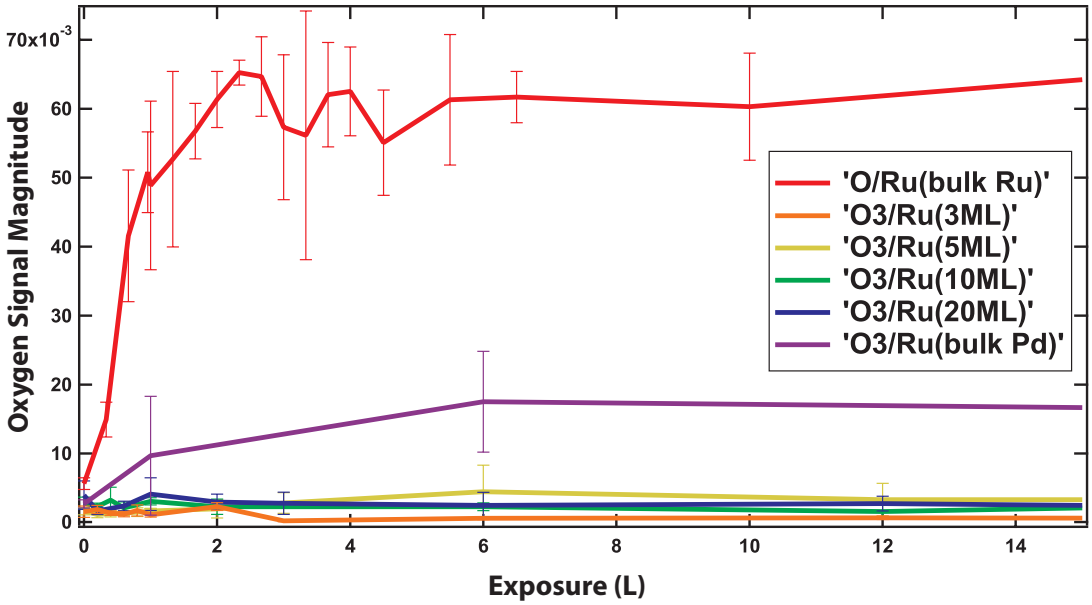

Figure 4.7: Oxygen uptake curves of Ru thin films for different film thickness. Uptake curves for bulk Ru and bulk Pd samples are also included. Each data point in the graph represents the average O/Ru Auger intensity ratio from five different areas on the sample. The error bars represent the standard deviation of the five measurements.

Clearly, oxygen does not adsorb on the ultrathin Ru films at room temperature. With decreasing temperatures, however, the oxygen sticking coefficient increases rapidly, and so it will be important to determine the desorption temperature of oxygen. To this end, we adsorbed oxygen on 3 ML and 20 ML thick Ru films at 112 K, while the sample was on the STM stage. The oxygen exposure for both samples was 1L. Immediately following the oxygen adsorption, the samples were imaged with STM at 112 K. Next, the samples were slowly warmed to room temperature, and STM images were collected at a few intermediate temperatures.

As can be seen from Figure 4.8, low temperature adsorption of oxygen gas produces small patches on the sample surface. Zooming in (see Figure 4.8(c)), one can see that these patches contain short-range ordered 2×2 structures. This is consistent with

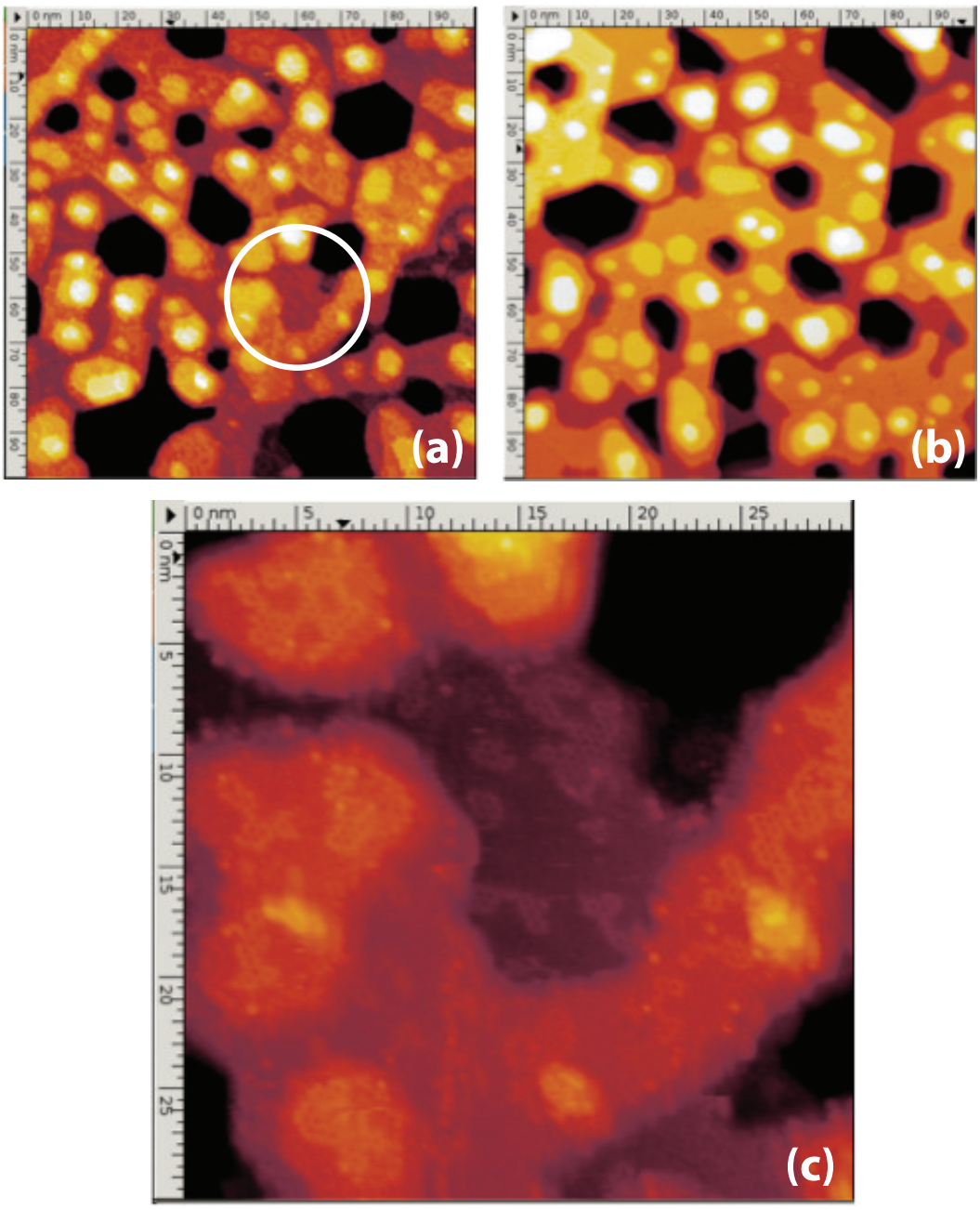

Figure 4.8: (a) STM image of a 3 ML thick Ru film, recorded at 112 K, after exposure to 1 L of oxygen at 112 K. Small patches are distributed both on the islands and in the holes. Image size: 100 nm×100 nm. (b) STM image after warming the sample to room temperature. Small patches disappeared, surface becomes clean after the warming. Image size: 100 nm×100 nm. (c) Image of circled area in (a). The oxygen induced 2×2 structure on the small patches is visible. Image size: 30 nm×30 nm

the STM results from bulk Ru(0001) and bulk Pd(111) surfaces (Wintterlin et al., 1997; Rose et al., 2004). Subsequent AES measurements at low temperature reveal a clear oxygen feature at about 515 eV kinetic energy. We can thus attribute these additional structures in the STM images to chemisorbed oxygen. STM imaging at 200 K shows a similar surface containing patches of chemisorbed oxygen. However, after warming the sample from 200 K to room temperature (see Figure 4.8(b)), the ordered patches completely disappear and, consistently, the AES spectra no longer contain any oxygen signature. When this surface is subsequently cooled down to 112K, the oxygen 2×2 patches do not re-appear. Clearly, oxygen completely desorbs somewhere between 200 K and room temperature.

The relatively weak bonding of oxygen on the ultrathin Ru films requires explanation. While it could be an electronic structure effect, related to the vertical confinement of the valence electrons in the film, or a residual strain effect do to the lattice mismatch with the Pd(111) substrate, there are complicating factors. First, the segregation of Pd atoms to the surface of the Ru film may weaken the oxygen bonding. Chapter 5 will address the thickness dependent reactivity of ultrathin Pd films grown on Ru(0001). However, it is also possible that the oxygen concentration at the surface is strongly influenced by hydrogen. Specifically, bulk Pd is known to absorb large amounts of atomic hydrogen, and there are experimental reports claiming that chemisorbed oxygen on the Pd(111) surface reacts with hydrogen originating from the Pd bulk, thus forming water molecules that readily desorb at 300 K (Steltenpohl and Memmel, 1999). This could explain the apparent inertness of our Ru films, assuming that hydrogen would diffuse through the Ru film and that water molecules readily desorb from the Ru(0001) surface at room temperature.

In our experiments, we have found it difficult to detect chemisorbed oxygen on the Pd(111) surface with LEED and AES, even after prolonged exposures at room temperature. Others (Conrad et al., 1977), however, did detect oxygen on bulk

Pd(111) with both LEED and AES. We suspect that our data on Pd(111) may be influenced by the presence of subsurface hydrogen. In order to reduce the subsurface hydrogen concentration, we annealed the Pd(111) crystal at about 1000°C, i.e., well above the hydrogen desorption temperature (Gdowski et al., 1987). After cooling the Pd crystal to room temperature, we exposed the surface to 1 L of molecular oxygen. This time, we observed a clear 2×2 LEED pattern and we also detected the oxygen $KL_{2,3}L_{2,3}$ Auger signal. However, the oxygen signatures in LEED and AES disappeared within 5 h, consistent with the literature reports (Steltenpohl and Memmel, 1999). The oxygen signatures in LEED and AES can be recovered through a second exposure experiment, but the oxygen features again vanished over time, possibly due to an additional influx of hydrogen from the bulk.

Interestingly, Ru thin films grown on the "back to normal" and "hydrogen depleted" Pd(111) substrates are no longer chemically "inert". A 1L oxygen exposure of the 3 ML and 5 ML Ru films produces an oxygen Auger signal that is comparable to that of a Ru(0001) surface, exposed to 15L of oxygen. Further investigations revealed that the observed oxygen Auger signal cannot be solely attributed to chemisorbed oxygen on the exposed Pd(111) substrate inside the deep holes (see Figure 4.4). Hence, it is reasonable to conclude that oxygen can be chemisorbed on the Ru films, provided that the Pd substrate is annealed to sufficiently high temperature. We conjecture that the apparent discrepancy with the results presented in Figure 4.7 can be attributed to differences in the hydrogen concentration below the Pd(111) surface.

4.4 Conclusion

We have studied the growth and surface reactivity of ruthenium thin films on Pd(111). Ruthenium films on Pd(111), grown at LN_2 and at room temperature, exhibit a nano-cluster morphology. Post annealing to 600°C produces a smooth surface, but Pd atoms are present on the Ru(0001) surface. The surface most likely represents

a random surface alloy. Subsequent experimental investigations of the chemical properties of the Ru thin films indicate that the Ru(0001) film surface was inert towards oxygen adsorption at room temperature. Oxygen desorbs between 200 K and room temperature. However, Ru films grown on a 1000°C pre-annealed Pd(111) substrate readily absorb oxygen. These seemingly inconsistent results suggest that hydrogen originating from the Pd bulk plays an important role in the chemical reactivity of the Ru overlayers.

Chapter 5

Growth and chemical properties of Pd thin film

5.1 Introduction

Heterogeneously catalyzed reactions typically start with the adsorption of reactant molecules onto the catalyst surface, followed by the dissociation, reaction and desorption (Ertl, 1990). As described in the Sabatier principle (Rothenberg, 2008, p. 65), the catalytic efficiency is determined by the strength of the interaction between reactants and catalyst: if the interaction is too weak, reactants do not adsorb and dissociate, whereas if the interaction is too strong the dissociation or reaction products do not desorb and leave the catalyst surface buried and inactive (Liu and Hu, 2001; Dahl et al., 2001; Nørskov et al., 2002). This interaction strength is directly related to the catalyst surface electronic structure. The underlying physics has been described by the d-band model proposed by Norskov (Hammer and Nørskov, 1995b, 2000; Bligaard and Nørskov, 2007). In the d-band model, the interaction strength between the metal catalyst and adsorbate molecule is coupled to the energy location of the metal d-band center before adsorption. The interaction of the molecular levels with the metal valence band is treated in two steps. The molecular levels first hybridize

with the relatively itinerant metal *sp* band resulting in a broad and low energy renormalized state. In a second step this renormalized state will interact with the relatively localized metal *d*-band, forming well-separated bonding and anti-bonding states. The strength of the resulting molecule-surface bond is determined by the filling of those anti-bonding states, and thus depends on the position of the unperturbed metal *d*-levels.

Indeed, while controlled tuning of catalytic activity remains difficult, manipulating the electronic structure of catalysts has been strongly pursued to enhance the catalytic activity. Typical approaches to this end include introducing active sites with a locally modified *d*-band centroid by doping or alloying with a different atomic species (Besenbacher et al., 1998; Chen et al., 2005) or by varying the dimensions of the material which exposes lattice sites with different symmetries such as step edges and high index crystallographic planes on nano-particles (Valden et al., 1998; Mavrikakis et al., 2000; Haruta, 2003). However, these approaches not only vary the *d*-state filling, they also change the local lattice symmetry and therefore the type of orbitals involved in chemical reactions taking place at these active sites. Hence, in these approaches the altered chemical activities cannot be ascribed solely to changes in the *d*-band centroid, leaving it an experimental challenge to properly validate the basic premise of the *d*-band model.

In order to circumvent these issues, we exploit size effects in atomically thin epitaxial films of Pd grown on Ru(0001) as a means to tune the metal surface *d*-band configuration in order to control oxygen adsorption. Oxygen dissociatively adsorbs on both bulk Ru(0001) and Pd(111) surfaces at room temperature (Mitchell et al., 1994; Rose et al., 2004) with saturation coverages of 0.5 and 0.25 ML for Ru and Pd, respectively (Madey et al., 1975; Wintterlin et al., 1997; Stampfl et al., 1996; Conrad et al., 1977; Leisenberger et al., 2000) for low oxygen partial pressures ($< 5 \times 10^{-5}$ torr). Our results reveal a surprisingly strong film thickness dependence of the

saturation coverage. The oxygen saturation coverage on Pd films between 2 and 5 ML thick is extremely small, while at lower and higher thicknesses it approaches that of bulk Ru and Pd, respectively. While changes in chemical reactivity and sticking probability on epitaxial Pt films on Ru(0001) have been observed before (Jakob et al., 2011), these observations were mostly attributed to a charge transfer from the film to the substrate (Rodriguez and Goodman, 1992; Hüger and Osuch, 2005). Moreover, the sticking probability was observed to increase monotonically with increasing film thickness from 1 to 10 monolayers (ML). Instead, we find that the reactivity of Pd films changes non-monotonically as a function of thickness from 1 to 5 monolayers (ML). Density functional theory (DFT) calculations of the electronic structure point at size effects in the developing Pd band structure for increasing thickness as the main cause of these observations. The observed increase in oxygen sticking probability of the Pd films beyond this minimum appears to be consistent with the central premise of the d-band model, namely, the energy-location of the d-states that are involved in oxygen binding gradually shifts towards the Fermi energy with increasing film thickness and ultimately stabilizes at the d-level location of bulk Pd. However, in a comparison of the calculated oxygen binding energies and d-band centroid locations for Pd film thicknesses below 1 ML (including the pristine Ru(0001) surface), the single-parameter description of the d-band model fails. These results therefore indicate that while the location of the d-band centroid is a proper indicator for the adsorbate-substrate interaction strength, its usefulness appears to be limited to comparisons involving the same subset of d-orbitals. Our exploitation of single crystalline films without changing symmetry or stoichiometry at the exposed surface thus offers a surprising view of the influence of size effects on the chemical reactivity, and presents a validation of the d-band model for the case where only the energy of the d-band center is tuned and the symmetry of the orbitals involved in the bonding remains unchanged.

5.2 Experimental details

Experiments were conducted in an ultra-high vacuum system (UHV) with a base pressure of 10^{-11} torr. The system is equipped with a variable temperature scanning tunneling microscope (STM), a single-pass CMA for Auger electron spectroscopy (energy resolution is 0.6%, modulation voltage is 1 V), low energy electron diffraction (LEED), and an ion sputter gun for in situ sample preparation and cleaning. Sample heating was achieved using electron-beam heating from the backside of the sample. The Ru(0001) crystal used in this study was cleaned by cycles of 500 eV Ne ion bombardment at 5×10^{-5} torr at room temperature and post-annealing up to 1100°C. Pd thin films were deposited onto the Ru substrate by direct heating of Pd in a home-made tungsten wire-basket. The Pd film thickness was calibrated with STM and AES (see Section 3.2.3). Oxygen was introduced into the UHV chamber with a variable leak valve to partial pressures between 2×10^{-8} torr and 4×10^{-8} torr. The sample was kept at room temperature during exposure. Different oxygen exposures were obtained by varying the duration of the exposure at constant pressure. The peak-to-valley amplitude of the derivative $KL_{2,3}L_{2,3}$ oxygen Auger peak was used as a measure of the oxygen concentration (see Appendix B.2).

5.3 Theoretical calculations

All density functional theory (DFT) calculations employed projector augmented wave potentials with the generalized gradient approximation for exchange and correlation as implemented in the Vienna Ab Initio Simulation Package (VASP v .5.3.3). A plane wave cutoff of 400 eV and an 8×8×1 Monkhorst k-point mesh were used for all slab calculations. The total energies were converged to 10^{-6} eV. We studied n Pd(111) thin film layers on six Ru(0001) substrate layers, where n=1, 2, 3. All thin film calculations were performed at our theoretical Ru in plane lattice constant of 2.706 $\mathring{A}$ which is in excellent agreement with the experimental value of a=2.71 $\mathring{A}$.

Bare Ru and Pd slab calculations consisted of 6 layers and were performed at their respective theoretical in-plane lattice constants. Our Pd bulk lattice constant of 3.952 $\mathring{A}$ is also within typical DFT agreement with the experimental value of 3.89 $\mathring{A}$. For each slab we consider 2×2 in-plane periodicity which resulted in 4 metal atoms on the surface. All slab calculations were performed with at least 16 $\mathring{A}$ of vacuum in between the slabs so as to eliminate spurious interactions between neighboring slabs in the periodic slab arrangement. For all simulations atoms were relaxed until the Hellman-Feynman forces on each atom was less than 0.01 eV/$\mathring{A}$.

For each system we consider a 1/4 ML oxygen coverage, where the oxygen atoms are located at the fcc hollow sites. We compute the Gibbs free energy of adsorption as follows:

$$\Delta G = E_{ads-surf} - E_{bare-surf} - N_O(\mu_O(T,p)) + ST + E_{vib}, \tag{5.1}$$

where $E_{ads-surf}$ and $E_{bare-surf}$ are the DFT total energies for the oxygen covered and bare surface of the slab respectively. N_O is the number of adsorbed O atoms and equals 1 for the 2×2 supercell. μ_O is the oxygen chemical potential and is defined as

$$\mu_O(T,p) = \frac{1}{2}E_{O_2} + \Delta\mu_O(T,p) \tag{5.2}$$

Here E_{O_2} is the total energy for an oxygen molecule at 0K obtained from DFT calculations and $\Delta\mu_O(T,p)$ are the temperature and pressure dependent part of the chemical potential which is related to the partial pressure of oxygen by:

$$\Delta\mu_0(T,p) = k_B T ln\frac{P_{O_2}}{P^0} \tag{5.3}$$

S is the configurational entropy terms defined as:

$$ST = k_B T(\frac{N_O}{4} ln\frac{N_O}{4} + (1 - \frac{N_O}{4}) ln(1 - \frac{N_O}{4})) \tag{5.4}$$

and E_{vib} is the vibrational entropy term, which is computed only for the vibrations of the oxygen molecule perpendicular to the surface.

5.4 Experimental results and discussion

For film growth and oxygen adsorption studies on reactive metals it is crucial to start with a thoroughly clean and ordered substrate surface, and to know how the film growth mode affects the surface morphology. We therefore first describe our results on the growth of the Pd films utilized in the oxygen adsorption studies. Figure 5.1 presents the surface morphology (a), surface symmetry (b), and AES spectrum (c) of the bulk Ru(0001) substrate surface after the surface cleaning procedure. The atomically flat surface morphology in STM images, the sharp hexagonal 1×1 LEED pattern without adsorbate induced reconstructions, and the absence of impurities in the AES spectrum, confirm the surface is clean.

Figure 5.2 shows the evolution of the surface morphology with increasing Pd film thickness, grown on the Ru substrate held at room temperature. As observed in Figure 5.2(a), depositing 0.65 ML Pd onto a Ru surface held at room temperature results in the formation of Pd monolayer islands emanating from the Ru step edges with alternating directions due to the $ABAB$ stacking of *hcp* Ru crystal (Hoster et al., 2006), suggesting pseudomorphic film growth. As Pd atoms continue to accumulate on the surface during further growth, the Pd islands expand and gradually fill the surface. These results mimic the growth of Pt on Ru(0001) (Käsberger and Jakob, 2003). The Pd film growth does not strictly follow the layer-by-layer growth mode. As shown in Figure 5.2(b) and (c), the growth of the second Pd layer commences before the first layer is completed. This trend persists up to larger thicknesses (see Figure 5.2(d)). LEED data for different film thicknesses (not shown) do not exhibit periodicities other than the 1×1 pattern already observed on the Ru(0001) substrate, indicating the surface of the Pd film is indeed clean and exhibits a bulk terminated

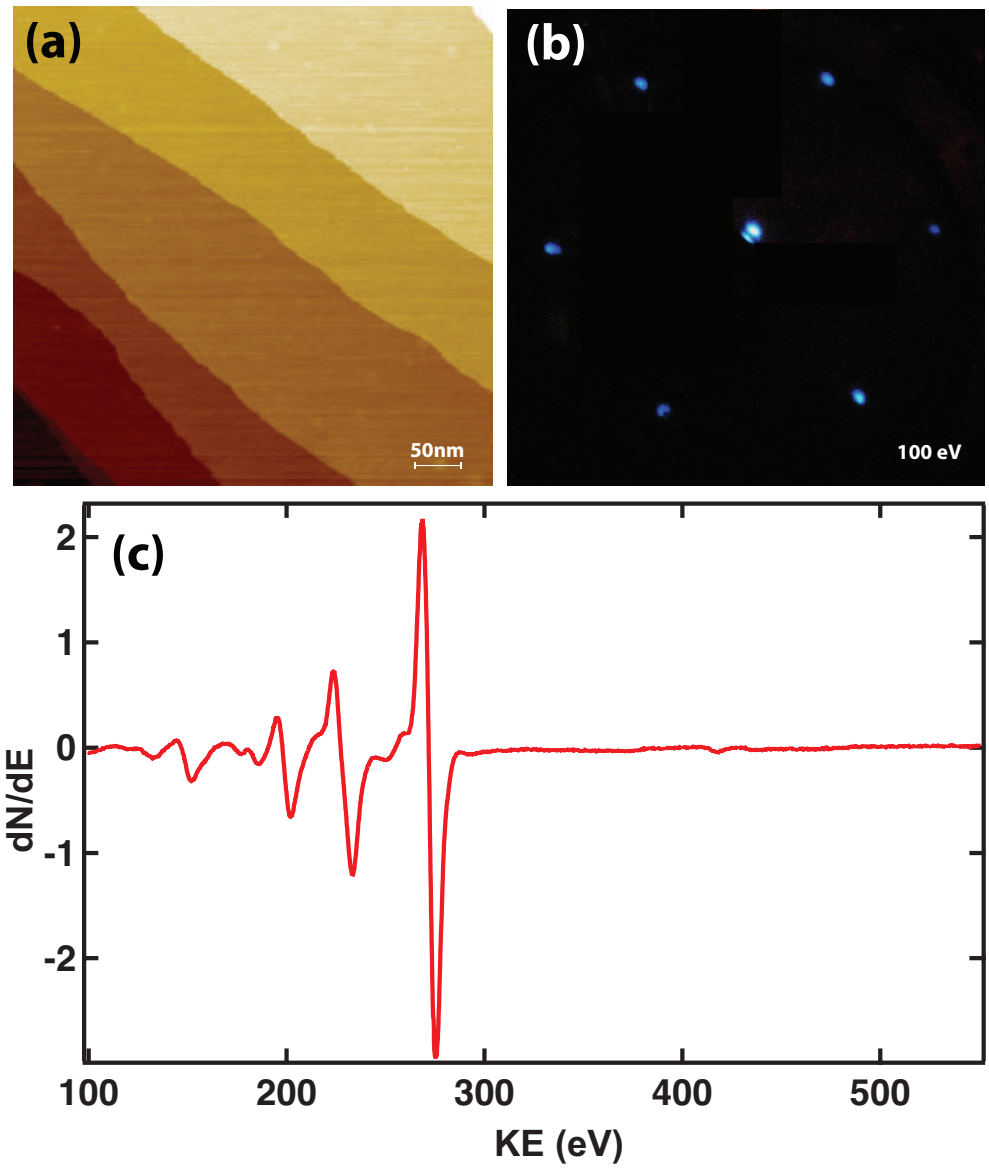

Figure 5.1: Clean Ru(0001) substrate characterization after the sputter-anneal treatment: (a) 500nm×500nm scale STM image of the surface (b) LEED pattern of surface at 100 eV (c) Auger spectrum of the surface

symmetry.

Next we examine the chemical properties of the Pd films via oxygen adsorption experiments. We exposed the films to molecular oxygen and subsequently evaluated the quantity of adsorbed oxygen using the magnitude of the oxygen $KL_{2,3}L_{2,3}$ peak at

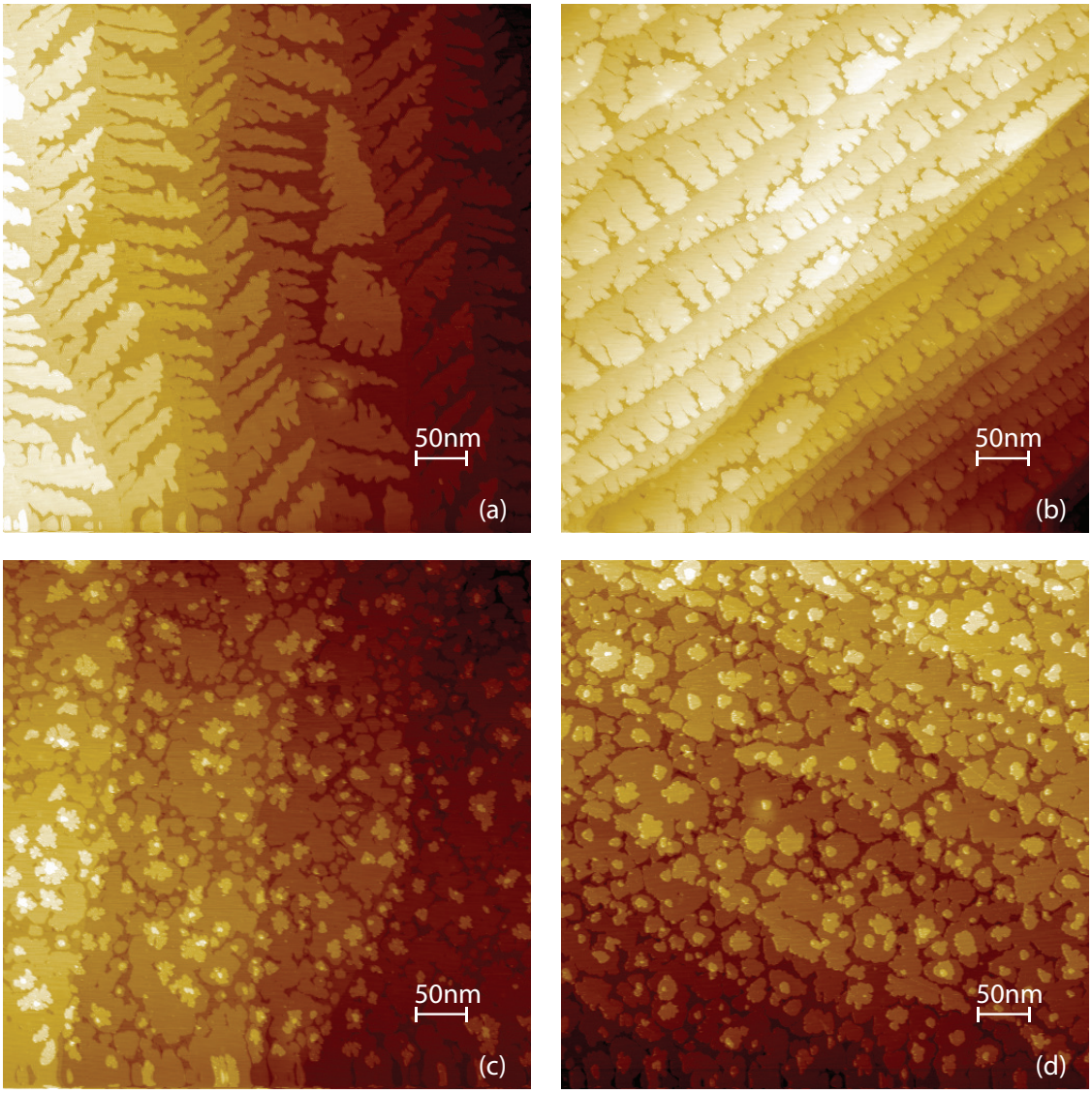

Figure 5.2: 500 nm×500 nm scale STM images of as-grown Pd thin films of different thickness: (a) 0.65 ML, (b) 0.85 ML, (c) 1.2ML, (d) 4.9M

510 eV. To account for possible beam current variations we measure the amplitude of the oxygen AES peak relative to the palladium MNN peak at 330 eV kinetic energy. We then normalized these relative O/Pd Auger peak amplitudes to the thickness of the Pd films as calibrated using STM and Auger experiments. This way, we are able to directly compare the oxygen saturation coverage for different film thicknesses. Figure 5.3 presents these data, where we used the known oxygen saturation coverages of 0.5 ML on the bulk Ru(0001) surface to calibrate our Auger intensities. The

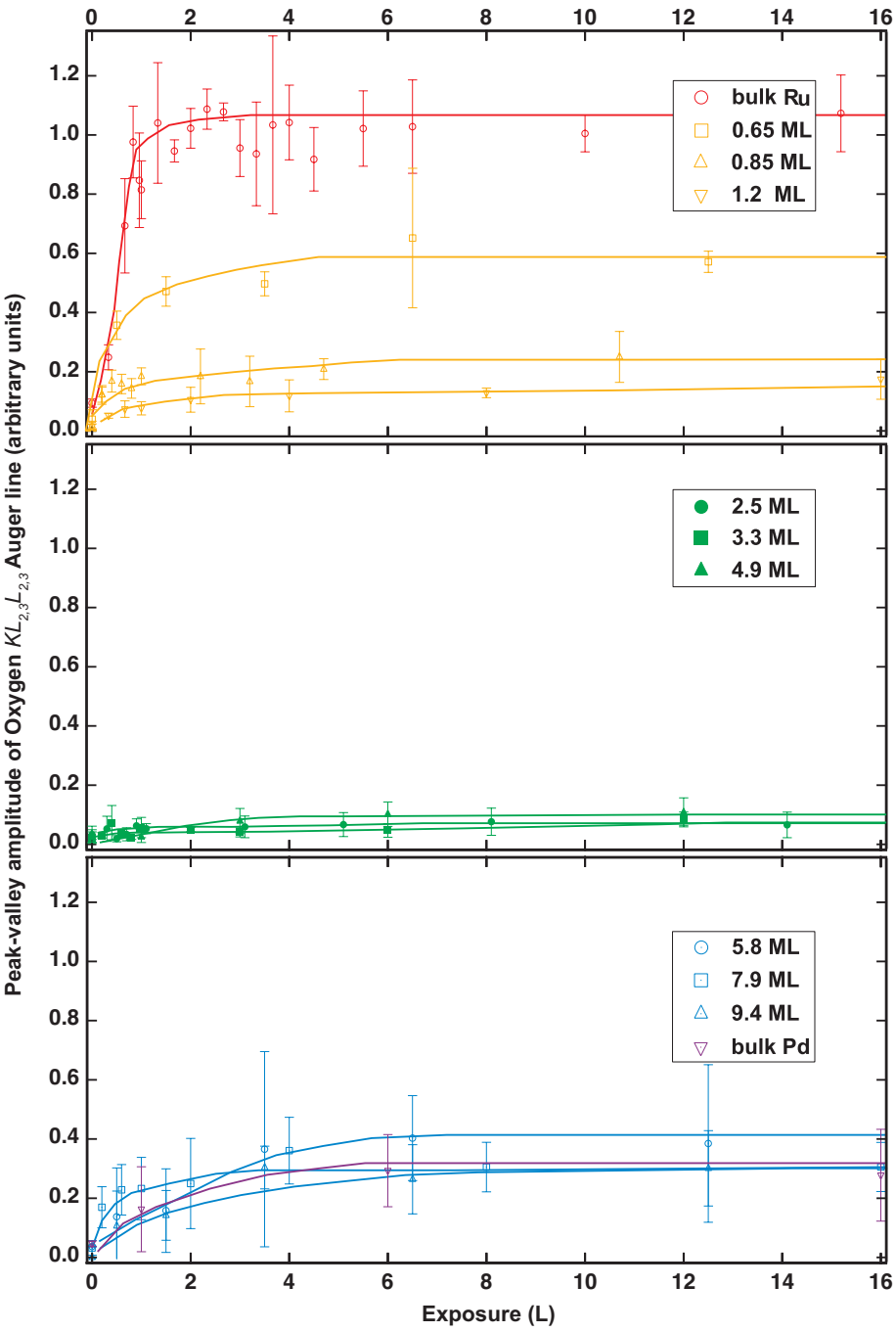

Figure 5.3: Room temperature oxygen uptake curves from Pd thin films of different thickness, including those of bulk Ru and bulk Pd. Each data point in the graph represents the average of five different areas on the sample, and the error bars come from the associated standard deviation.

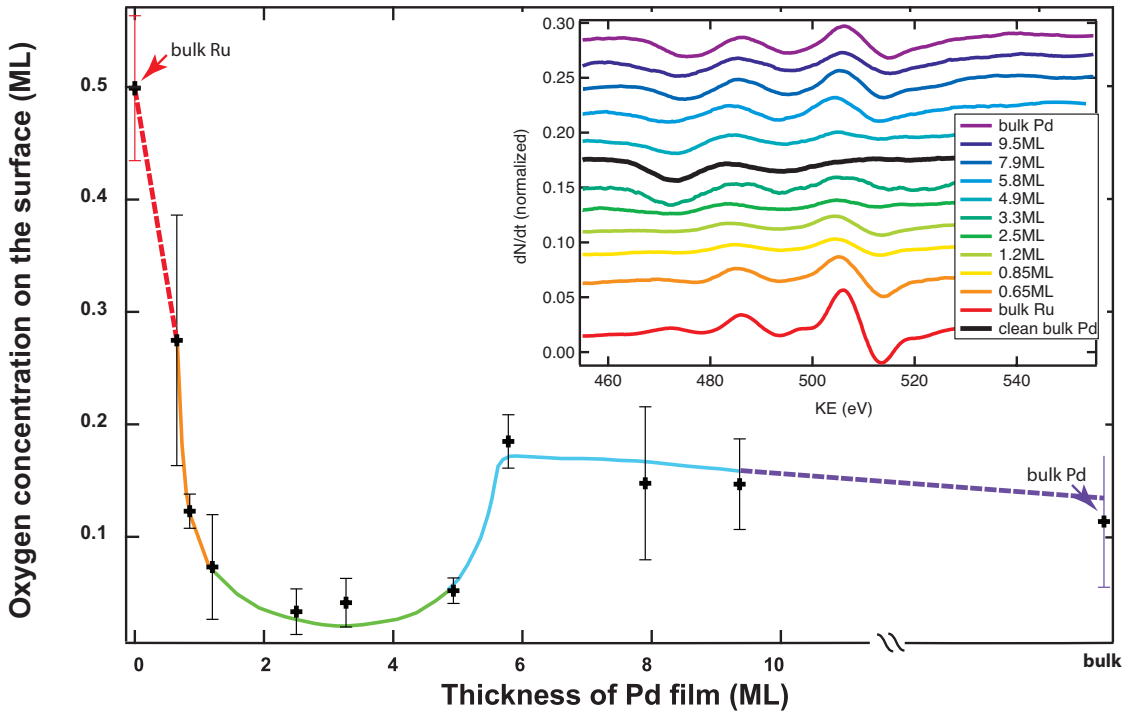

Figure 5.4: Oxygen concentration at saturation, represented by the peak-valley amplitude of Oxygen $KL_{2,3}L_{2,3}$ Auger line, as a function of the film thickness on different samples at total exposure of 12L. (Inset) Oxygen $KL_{2,3}L_{2,3}$ Auger spectra of different samples at saturation. The non-monotonic variation in the oxygen coverage is readily evident from the raw Auger spectra.

concentration of adsorbed oxygen rapidly increases and quickly saturates around 5 L for all samples, consistent with previous work (Madey et al., 1975; Conrad et al., 1977). Strikingly, the data reveal a significant non-monotonic thickness dependence of the oxygen concentration at saturation. Indeed, in Figure 5.4 we have plotted the normalized oxygen $KL_{2,3}L_{2,3}$ Auger amplitude at saturation coverage as a function of the Pd film thickness, revealing a pronounced minimum in the oxygen saturation coverage, with a minimum value almost indistinguishable from zero. This size effect can also be observed in the AES spectra of the oxygen $KL_{2,3}L_{2,3}$ Auger line, presented in the inset of Figure 5.4, showing a significant decrease in the oxygen AES amplitude for intermediate Pd film thicknesses between 2 and 5 ML. Note that the Auger spectra of Pd also exhibit small features in this energy range. Although these Pd features can be distinguished from the oxygen $KL_{2,3}L_{2,3}$ lines by their slightly different energies,

it is hard to reliably subtract them from the spectra of the oxygen exposed samples, and therefore they account for at least part of the normalized oxygen intensity in the 2-5 ML Pd film thickness range, and our extracted oxygen coverage in Figure 5.4, is therefore an upper bound. Note also that according to the literature, the room temperature oxygen saturation coverage on the bulk Pd(111) surface is half of that on the bulk Ru surface (Madey et al., 1975; Wintterlin et al., 1997; Stampfl et al., 1996; Conrad et al., 1977; Leisenberger et al., 2000). However, we observe that the measured AES amplitude of oxygen on bulk Pd(111) is even a little bit smaller. While this could be caused by electron-induced oxygen desorption from exposure to the Auger electron beam (Voogt et al., 1997; Steltenpohl and Memmel, 1999), we made sure that the total duration of electron beam exposure was similar for all experiments, suggesting that the relatively smaller signal on bulk Pd is not due to electron-induced desorption.

In order to gain an understanding of the surprising non-monotonic size dependence observed in the oxygen saturation coverage on atomically thin Pd films, we calculated the thickness dependent oxygen binding energy and the density of states of Pd films on the Ru(0001) substrate, as well as the oxygen binding energy of bulk Ru(0001) and Pd(111) surfaces, using density functional theory. The oxygen atoms are placed at the fcc hollow sites (with one oxygen atom per 2×2 unit cell) and their binding energies are plotted in Figure 5.5 as a function of the d-band center location of the corresponding bare surface (i.e. without adsorbed oxygen). For the Pd thin film samples (with the exception of the 3/4 ML thick Pd film), we find that the trend follows the prediction of the Hammer-Nørskov d-band model (Hammer and Nørskov, 1995b, 2000; Bligaard and Nørskov, 2007): the oxygen binding energy increases with decreasing d-band center energy as the film thickness increases from 1 ML up to the bulk limit (Hammer and Nørskov, 1995b). The deviations from this trend for the 0.75 ML thick Pd film and the bulk Ru(0001) surface will be discussed in further detail below.

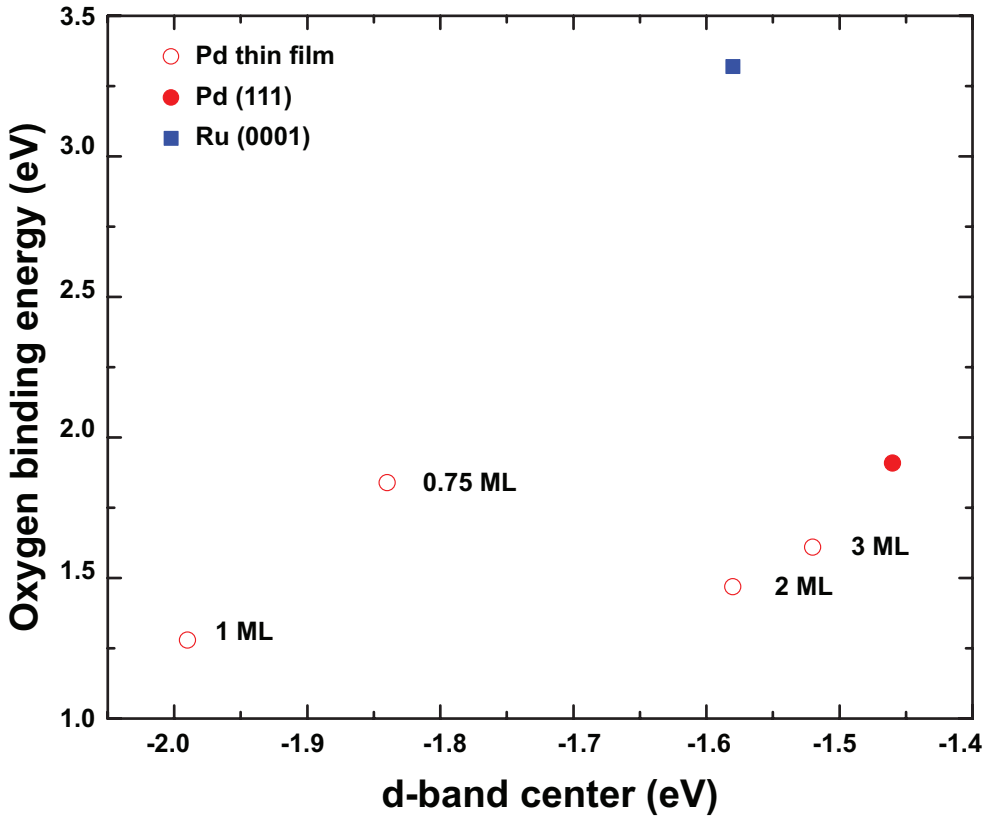

Figure 5.5: Calculated O binding energies on Pd thin films, as well as on the bulk Ru(0001) and Pd(111) surfaces, versus the corresponding unperturbed d-band centeroid

Charge density contours (not shown) reveal that the d_{xz} and d_{yz} orbitals are the principal participants in the oxygen-surface bonding. Indeed, the calculated total and partial d_{xz} and d_{yz} DOS presented in Figure 5.6 shows that the DOS of these d-orbitals gradually shifts towards the Fermi energy with increasing Pd film thickness, starting at 1 ML. In fact, the shift of the d-band center can be attributed primarily to the shift of the d_{xz} and d_{yz} partial DOS. As a consequence, the peak of the antibonding O $2p$-Pd $3d$ states (after oxygen adsorption) shifts to higher energies above the Fermi energy, decreasing its filling and increasing the oxygen binding energy. This shift can be clearly observed in the the oxygen partial DOS of the oxidized Pd films, see Figure 5.7.

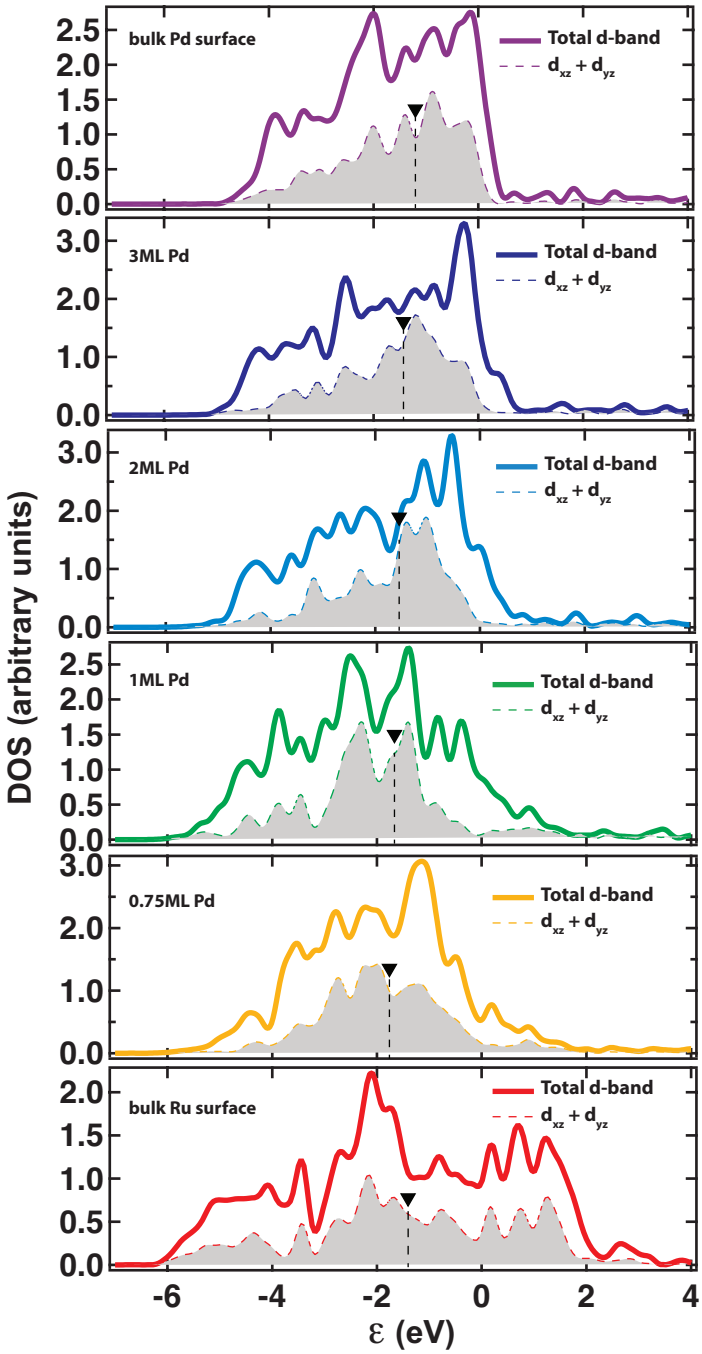

Figure 5.6: Density of states (DOS) distribution of the total d-band and of the d_{xz} d_{yz} states combined (gray area) prior to oxygen adsorption. A thickness dependent shift in the centroid of total d-band is visible. The small black triangles indicate the centroids of the partial $d_{xz} + d_{yz}$ DOS.

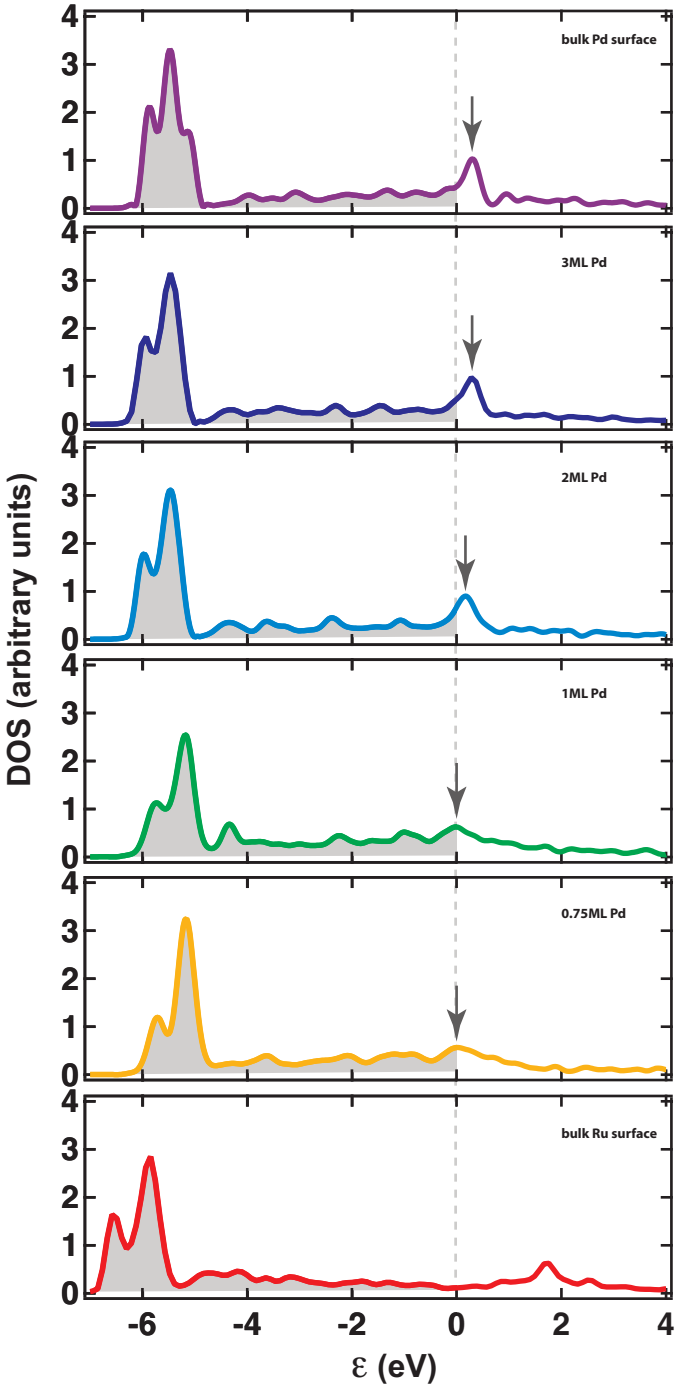

Figure 5.7: Evolution of the oxygen 2*p*-*d* hybridized states on Pd/Ru(0001) thin film samples with different Pd thickness. A shift in the 2*p*-*d* anti-bonding states, indicated by the arrow, is clearly visible.

The shift of the d-states towards the Fermi level could in principle be the result of a charge transfer between the Pd film and the Ru substrate (Rodriguez and Goodman, 1992; Cooper et al., 2005). However, this effect will be insignificant for metal films with thicknesses beyond 1 ML, and indeed our DFT calculations do not indicate such a charge transfer is significant even for the first ML of Pd. Because we do not see evidence for a quantum size effect in the calculated electronic structure, we conclude that the shift of the d_{xz} and d_{yz} states towards the Fermi energy originates in a chemical size effect: the onset of and subsequent increase in the out-of-plane bonding with increasing film thickness shifts the centroid of the d_{xz} and d_{yz} bands closer to the Fermi level.

As observed above in Figure 5.5, the 0.75 ML Pd film and the bulk surface Ru(0001) buck this trend. The oxygen binding energy is significantly higher than expected from the corresponding location of the d-band center (Figure 5.5). For the 0.75 ML Pd sample, this is mainly due to the lower Pd density, which results in the Pd d_{x^2-y2} states that are involved in in-plane Pd-Pd bonding for complete monolayers, now dominating the adsorbate-surface bonding. Moreover, fitting our results to the d-band model of Hammer et al. (1996), we find that the matrix elements V, representing the coupling between the metal d-band and the molecular resonances (see Section 2.5.2), are significantly larger for both the 0.75 ML thick Pd film and the bulk Ru(0001) surface , leading to an enhancement in the oxygen binding energy for the 0.75 ML Pd sample and bulk Ru(0001). These results make it clear that the material-independent descriptor advocated by the d-band model is only valid when the symmetry of the orbitals involved in the bonding remains the same when comparing oxygen binding energies. They emphasize the importance of understanding the nature of the orbitals involved in adsorption and catalysis (Cooper et al., 2005; Mason et al., 2008).

Finally, we calculated the Gibbs free energy of the oxidized Pd films on Ru(0001) as a

function of the oxygen chemical potential at 300 K according to Reuter and Scheffler (2001), see Figure 5.8. For $\Delta\mu_O > -1.6eV$ (i.e. at low partial pressure of O_2) the change in Gibbs free energy upon oxygen adsorption indicates that oxygen adsorption is only thermodynamically favorable for the bulk Pd(111) surface and not for the Pd thin films. As we increase $\Delta\mu_O$ above $-1.6\ eV$ the films also begin to favor adsorption, starting at thicker Pd films and progressively including the thinner Pd films. These results compare well with the observed experimental trend that the Pd films evolve toward the bulk value for thicker films, although the relevant range of the chemical potential implies much smaller partial pressures than present in the experiment*.

*While the exposure was done between 2×10^{-8} torr and 4×10^{-8} torr partial pressure, the AES measurements were done after the oxygen was pumped out and oxygen partial pressure dropped below the detection limit of our RGA (residual gas analyzer) ($< 10^{-12}$ torr).

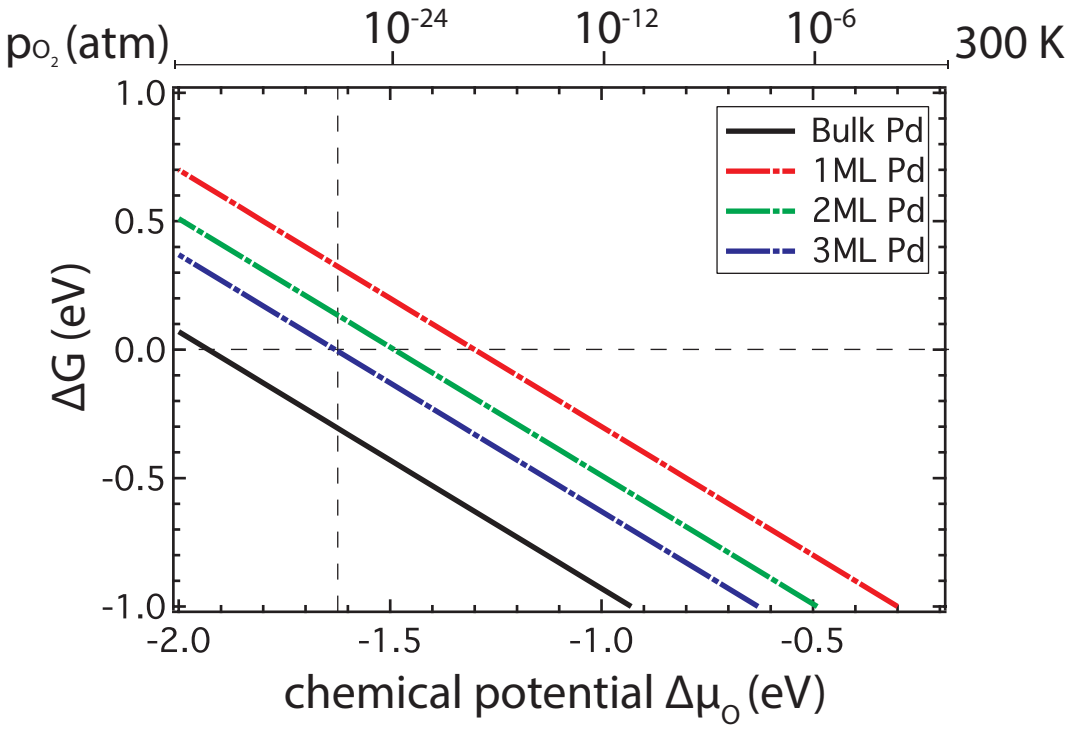

Figure 5.8: The change in the Gibbs free energy upon oxygen adsorption on bulk Pd(111) and Pd thin films as a function of the oxygen chemical potential at room temperature. Negative values of the ΔG indicate that adsorption is thermodynamically favorable.

It should be noted that the deviation in corresponding partial pressures could be a consequence of either systematic errors in the DFT calculation or they could be of a more fundamental nature. For example, it is possible that the lower binding energies of O to the films may also be manifested in higher dissociation barriers for O_2, as suggested by the empirical Brønsted-Evans-Polanyi relation (Brønsted, 1928; Evans and Polanyi, 1938; Bligaard et al., 2004)[†]. Alternatively, even species that are adsorbed with a finite binding energy can still effectively desorb at temperatures below their activation energy because of large kinetic pre-factors in the Arrhenius expression for the desorption rate (Bozso et al., 1977). This would particularly affect low-binding energy configurations, which could explain why there is no oxygen present on the surface of ultrathin Pd films for ranges of the chemical potential where theory predicted oxygen should bind. It would require computationally intensive DFT-based nudged elastic band simulations (Henkelman et al., 2000; Zhu et al., 2004) to elucidated these kinetic factors, which is out of the scope of the present study. Nevertheless, it is important to keep in mind that kinetics may play a significant role in molecular adsorption and desorption.

We would also like to note that the presence of subsurface oxygen and electron-beam induced desorption does not appear to be relevant to our observations. It has been argued(Conrad et al., 1977; Légaré et al., 1981; Weissman-Wenocur et al., 1983; Voogt et al., 1997; Leisenberger et al., 2000) that a fraction of the adsorbed oxygen atoms at room temperature can diffuse into the subsurface region of bulk Pd(111). Although there has been some debate about the location of the diffused oxygen atoms below the surface(Conrad et al., 1977; Weissman-Wenocur et al., 1983; Voogt et al., 1997), if subsurface oxygen indeed is present in our Pd thin films, then this would have the

[†]In physical chemistry, the Brønsted-Evans-Polanyi relation describes the linear relationship between the activation energy and the enthalpy of reaction, in other words, the more stable the reaction product is the lower the activation barrier of reaction is. For the dissociative chemisorption of molecules on the surface, following the reaction coordinates graph in Chapter 1 (see Figure 1.2), it corresponds to the linear relationship between the activation energy E_a and the dissociative chemisorption energy ΔE.

potential to affect our estimation of the surface oxygen concentration from the Auger measurements. However, the experimental results in Conrad et al. (1977); Légaré et al. (1981); Weissman-Wenocur et al. (1983); Voogt et al. (1997); Leisenberger et al. (2000) consistently reveal that subsurface oxygen is not present without oxygen present on the surface. Therefore, our observation of a negligible saturation coverage on the Pd films is independent of the presence or absence of any subsurface oxygen. Second, there has been evidence that (Voogt et al., 1997; Steltenpohl and Memmel, 1999) high energy Auger electron beams can induce oxygen desorption. We have ruled out this effect by keeping beam exposures the same for all samples. The different saturation concentrations for the same electron beam exposures therefore imply that beam exposure is not a factor in our experimental approach.

5.5 Conclusion

In conclusion, we have studied room temperature oxygen adsorption on pseudomorphic Pd thin films grown on Ru(0001). The oxygen saturation coverage evolves non monotonically as a function of the film thickness, exhibiting a pronounced minimum between 2 and 5 ML of Pd where the saturation coverage is almost zero. Aided by DFT calculations, our analysis suggests that a chemical size effect is the cause of these surprising observations: the formation of a band structure with increasing Pd film thickness shifts the d_{xz} and d_{yz} orbitals that are involved in the metal-oxygen bonding closer to the Fermi level. This increases the oxygen binding energy on the surface as predicted by the d-band model. The 0.75 ML thick Pd film and bulk Ru(0001) surface deviate from this trend because the symmetries of the orbitals involved in the metal-oxygen bonding are different. By tuning the density of d-states for a given element, and maintaining constant orbital character in the chemical bond formation, we have demonstrated the basic validity of the d-band model. The predictive power of the d-band model appears limited when these conditions are no longer satisfied.

Chapter 6

Summary and outlook for future research

In this thesis, we studied the chemical reactivity of ruthenium and palladium thin films at room temperature. Although the initial expectations of a "size effect" on the reactivity of these two systems were similar, experiments revealed two completely different scenarios. For Ru(0001) thin films grown on Pd(111), no clear "size effect" was observed. However, their surfaces are extremely inert towards oxygen adsorption. The presence of a Ru/Pd surface alloy appears to be main factor that governs the surface chemical reactivity of these films, although hydrogen diffusion from the Pd substrate complicated the picture. For Pd(111) thin films grown on a Ru(0001) substrate, we did observe a clear "size effect" : the surface chemical reactivity towards oxygen adsorption varies non-monotonically with film thickness. it's origin does not lie in a *quantum* size effect, but rather it is caused by the formation and evolution of the Pd band structure along the growth direction as the film thickness increases. A surprising observation common to both systems is that both exhibit a regime with an unexpected inertness of the surface toward oxygen adsorption even though both Ru and Pd are elements that easily oxidize in bulk form.

There are still many open questions specific to these two systems that would require further experimental and theoretical study. We provide two examples here. First, as we discussed in Chapter 5, the d-band model does explain the change in chemical reactivity of the Pd thin films above 1 ML, but the symmetry of the $4d$-orbitals involved in the oxygen bonding plays a key role. According to the theoretical calculations, the Pd d_{xz} and d_{yz} states are the biggest contributors to the formation of the metal-oxygen bond when oxygen adsorbs at the *fcc* hollow sites of the Pd(111) substrate. However, for the 0.75 ML Pd film, the sparse distribution of Pd atoms on the surface results in the Pd-$d_{x^2-y^2}$ states that are involved in in-plane Pd-Pd bonding for complete monolayers, now dominating the adsorbate-surface bonding. These results point to the importance of identifying the electronic structure of the surface region of these thin film materials with energy, momentum, and orbital resolution. STM alone is not able to provide these data, and other electron spectroscopic techniques such as ARPES (angle-resolved photoemission spectroscopy) or HREELS (high resolution electron energy spectroscopy) would be necessary to complete our knowledge. Similar issues play a role for the Ru films on Pd(111). Here, the situation is even more complicated due to the presence of deep holes in the film and surface alloying, creating a surface with changing chemical composition. Second, the core findings of our experiments regarding the chemical activities of thin films are all based on the observation of varying oxygen coverage on these surfaces. The explanations we put forward are based on a consideration of the thermodynamic stability of one particular state, in our case the 1/4 ML 2×2 configuration of dissociatively adsorbed oxygen. In this analysis, we neglected kinetic factors that could take effect whether or not the thermodynamically preferred state can be reached. Examples of these kinetic factors are energy barriers for dissociation, diffusion, and desorption of the oxygen atoms and molecules. Specifically, even species that are adsorbed with binding energy larger than the thermal energy (k_BT) at room temperature can still effectively desorb at temperatures well below their activation energy because of the often large kinetic pre-factors in the Arrhenius expression describing the desorption

rate. Further experiments with temperature programmed thermal-desorption (TPD) and time-resolved STM imaging of oxygen atoms and molecules on the surface of Ru and Pd thin films may provide us with a clearer picture of these kinetic factors.

The two main experimental findings in our studies of Ru and Pd thin films are that atomic scale size effects in, and surface alloying of reactive elements can create surfaces that are inert to oxygen adsorption. The system for which we developed better understanding of the underlying reasons for these surprising properties is the system that exhibits the least complicated structure: a pure, single crystalline Pd(111) overlayer on a pure, single crystalline Ru substrate. While this may not look surprising, we stress that the adherence to, and therefore validation of, the *d*-band model by Nørskov and Hammer has never before been demonstrated in a series of experiments where only one parameter, in our case the Pd film thickness, was changed. In spite of this validation of the core idea of the *d*-band model, our results also pointedly demonstrate that a conceptually simple guiding principle such as the *d*-band model quite dramatically fails when presumably minor changes in the system are brought about, such as a change in $4d$-level occupancy when going from Ru to Pd, or even only a change in orbital symmetry. This demonstrates that exquisite experimental control is indispensable if a full basic understanding or validation of a general concept is to be obtained. As we have demonstrated here, well-controlled studies on well-characterized single crystalline surfaces, without the introduction of dopants, steps, or other active sites, is one of the most achievable and promising routes to create and truly understand materials with controllable chemical properties.

Bibliography

Alayoglu, S., Nilekar, A. U., Mavrikakis, M., and Eichhorn, B. (2008). Ru–pt core–shell nanoparticles for preferential oxidation of carbon monoxide in hydrogen. *Nature materials*, 7(4):333–338. 43

Armor, J. (2008). What is catalysis? the north american catalysis society (nacs). 1

Bell, A. T. (2003). The impact of nanoscience on heterogeneous catalysis. *Science*, 299(5613):1688–1691. 1, 3

Bergbreiter, A., Hoster, H. E., and Behm, R. J. (2011). Segregation and stability in surface alloys: Pdxru1- x/ru (0001) and ptxru1- x/ru (0001). *ChemPhysChem*, 12(6):1148–1154. 49

Besenbacher, F., Chorkendorff, I., Clausen, B., Hammer, B., Molenbroek, A., Nørskov, J. K., and Stensgaard, I. (1998). Design of a surface alloy catalyst for steam reforming. *Science*, 279(5358):1913–1915. 5, 59

Biberian, J. and Somorjai, G. (1979). On the determination of monolayer coverage by auger electron spectroscopy. application to carbon on platinum. *Applications of Surface Science*, 2(3):352–358. 29

Bligaard, T. and Nørskov, J. K. (2007). Ligand effects in heterogeneous catalysis and electrochemistry. *Electrochimica Acta*, 52(18):5512–5516. 5, 20, 58, 68

Bligaard, T., Nørskov, J. K., Dahl, S., Matthiesen, J., Christensen, C. H., and Sehested, J. (2004). The brønsted–evans–polanyi relation and the volcano curve in heterogeneous catalysis. *Journal of Catalysis*, 224(1):206–217. 74

Bozso, F., Ertl, G., and Weiss, M. (1977). Interaction of nitrogen with iron surfaces: Ii. fe (110). *Journal of Catalysis*, 50(3):519–529. 74

Brønsted, J. (1928). Acid and basic catalysis. *Chemical Reviews*, 5(3):231–338. 74

Cant, N. W., Hicks, P., and Lennon, B. (1978). Steady-state oxidation of carbon monoxide over supported noble metals with particular reference to platinum. *Journal of Catalysis*, 54(3):372–383. 3

Chen, C. J. (1993). *Introduction to scanning tunneling microscopy*, volume 227. Oxford University Press New York. xiv, 33, 34

Chen, M., Kumar, D., Yi, C.-W., and Goodman, D. W. (2005). The promotional effect of gold in catalysis by palladium-gold. *Science*, 310(5746):291–293. 5, 59

Chorkendorff, I. and Niemantsverdriet, J. W. (2006). *Concepts of modern catalysis and kinetics*. John Wiley & Sons. 5

Conrad, H., Ertl, G., Küppers, J., and Latta, E. (1977). Interaction of no and O_2 with pd (111) surfaces. ii. *Surface Science*, 65(1):245–260. 51, 55, 59, 67, 68, 74, 75

Cooper, V. R., Kolpak, A. M., Yourdshahyan, Y., and Rappe, A. M. (2005). Supported metal electronic structure: Implications for molecular adsorption. *Physical Review B*, 72(8):081409. 5, 72

Dahl, S., Logadottir, A., Jacobsen, C. J., and Nørskov, J. K. (2001). Electronic factors in catalysis: the volcano curve and the effect of promotion in catalytic ammonia synthesis. *Applied Catalysis A: General*, 222(1):19–29. 4, 58

Deutschmann, O., Knözinger, H., Kochloefl, K., and Turek, T. (2000). *Heterogeneous Catalysis and Solid Catalysts*. Wiley-VCH Verlag GmbH & Co. KGaA, Weinheim, Germany. 16, 17

Duan, L., Bozoglian, F., Mandal, S., Stewart, B., Privalov, T., Llobet, A., and Sun, L. (2012). A molecular ruthenium catalyst with water-oxidation activity comparable to that of photosystem ii. *Nature chemistry*, 4(5):418–423. 42

Engel, T. and Ertl, G. (1979). Elementary steps in the catalytic oxidation of carbon monoxide on platinum metals. *Advances in Catalysis*, 28:1–78. 3

Erti, G. and Freund, H.-J. (1999). Catalysis and surface science. *Phys. Today*, 52:32. 3

Ertl, G. (1990). Elementary steps in heterogeneous catalysis. *Angewandte Chemie International Edition in English*, 29(11):1219–1227. 58

Ertl, G. (2002). Heterogeneous catalysis on atomic scale. *Journal of Molecular Catalysis A: Chemical*, 182:5–16. 4, 6

Ertl, G., Knözinger, H., Schüth, F., and Weitkamp, J. (2008). *Handbook of Heterogeneous Catalysis, 8 Volumes(part.1)*. Wiley-VCH. 3, 5, 6, 16, 17

Evans, M. and Polanyi, M. (1938). Inertia and driving force of chemical reactions. *Trans. Faraday Soc.*, 34:11–24. 74

Feibelman, P. J. and Hamann, D. (1984). Electronic structure of a" poisoned" transition-metal surface. *Physical review letters*, 52(1):61. 20

Feibelman, P. J. and Hamann, D. (1985). Modification of transition metal electronic structure by p, s, cl, and li adatoms. *Surface Science*, 149(1):48–66. 20

Gallon, T. (1969). A simple model for the dependence of auger intensities on specimen thickness. *Surface Science*, 17(2):486–489. 29

Gdowski, G., Felter, T., and Stulen, R. (1987). Effect of surface temperature on the sorption of hydrogen by pd (111). *Surface Science*, 181(3):L147–L155. 56

Griffiths, D. J. (2005). Introduction to quantum mechanics. *Prentice Hall)*,, 23:26. 18

Groß, A. (2007). Theoretical surface science: A microscopic perspective. xiii, 7, 9, 11, 18, 20

Grubbs, R. H. (2005). Olefin metathesis catalysts for the preparation of molecules and materials. *Nobel Lecture, December*, 8. 5, 17, 42

Hammer, B., Morikawa, Y., and Nørskov, J. K. (1996). Co chemisorption at metal surfaces and overlayers. *Physical review letters*, 76(12):2141. 72

Hammer, B. and Nørskov, J. (1995a). Electronic factors determining the reactivity of metal surfaces. *Surface Science*, 343(3):211–220. 20, 23

Hammer, B. and Nørskov, J. (1995b). Why gold is the noblest of all the metals. *Nature*, 376(6537):238–240. 5, 20, 58, 68

Hammer, B. and Nørskov, J. K. (2000). Theoretical surface science and catalysis?calculations and concepts. *Advances in catalysis*, 45:71–129. 5, 20, 22, 58, 68

Harris, J. and Andersson, S. (1985). H 2 dissociation at metal surfaces. *Physical review letters*, 55(15):1583. 20

Haruta, M. (2003). When gold is not noble: catalysis by nanoparticles. *The Chemical Record*, 3(2):75–87. 59

Henkelman, G., Uberuaga, B. P., and Jónsson, H. (2000). A climbing image nudged elastic band method for finding saddle points and minimum energy paths. *The Journal of Chemical Physics*, 113(22):9901–9904. 74

Hoffmann, R. (1987). How chemistry and physics meet in the solid state. *Angewandte Chemie International Edition in English*, 26(9):846–878. 18

Hoffmann, R. (1988a). A chemical and theoretical way to look at bonding on surfaces. *Reviews of modern Physics*, 60(3):601. xiii, 18, 19, 20

Hoffmann, R. (1988b). Solids and surfaces: a chemist's view of bonding in extended structures. Technical report, DTIC Document. 18

Hondros, E. and Seah, M. (1977). The theory of grain boundary segregation in terms of surface adsorption analogues. *Metallurgical Transactions A*, 8(9):1363–1371. 9, 12

Hoster, H., Filonenko, E., Richter, B., and Behm, R. (2006). Formation and short-range order of two-dimensional cu x pd 1- x monolayer surface alloys on ru (0001). *Physical Review B*, 73(16):165413. 63

Hüger, E. and Osuch, K. (2005). Making a noble metal of pd. *EPL (Europhysics Letters)*, 71(2):276. 60

Jakob, P., Schlapka, A., and Gazdzicki, P. (2011). Oxygen adsorption on pt/ru (0001) layers. *The Journal of chemical physics*, 134(22):224707. 60

Joo, S. H., Park, J. Y., Renzas, J. R., Butcher, D. R., Huang, W., and Somorjai, G. A. (2010). Size effect of ruthenium nanoparticles in catalytic carbon monoxide oxidation. *Nano letters*, 10(7):2709–2713. 3

Käsberger, U. and Jakob, P. (2003). Growth and thermal evolution of submonolayer pt films on ru (0001) studied by stm. *Surface science*, 540(1):76–88. 63

Kasemo, B. and Törnqvist, E. (1980). Weighing fractions of monolayers: Application to the adsorption and catalytic reactions of H_2, CO, and O_2 on Pt. *Physical Review Letters*, 44(23):1555. 27

Kitchin, J., Nørskov, J. K., Barteau, M., and Chen, J. (2004a). Modification of the surface electronic and chemical properties of pt (111) by subsurface 3d transition metals. *Journal of Chemical Physics*, 120(21):10240–10246. 22

Kitchin, J. R., Nørskov, J. K., Barteau, M. A., and Chen, J. (2004b). Role of strain and ligand effects in the modification of the electronic and chemical properties of bimetallic surfaces. *Physical review letters*, 93(15):156801. 22

Légaré, P., Hilaire, L., Maire, G., Krill, G., and Amamou, A. (1981). Interaction of oxygen and hydrogen with palladium. *Surface Science*, 107(2):533–546. 74, 75

Leisenberger, F., Koller, G., Sock, M., Surnev, S., Ramsey, M., Netzer, F., Klötzer, B., and Hayek, K. (2000). Surface and subsurface oxygen on pd (111). *Surface science*, 445(2):380–393. 59, 68, 74, 75

Lischka, M. and Groß, A. (2002). Hydrogen adsorption on an open metal surface: H 2/pd (210). *Physical Review B*, 65(7):075420. 9

Liu, Z.-P. and Hu, P. (2001). General trends in co dissociation on transition metal surfaces. *The Journal of Chemical Physics*, 114(19):8244–8247. 58

Ma, X., Jiang, P., Qi, Y., Jia, J., Yang, Y., Duan, W., Li, W.-X., Bao, X., Zhang, S., and Xue, Q.-K. (2007). Experimental observation of quantum oscillation of surface chemical reactivities. *Proceedings of the National Academy of Sciences*, 104(22):9204–9208. 2, 5

Madey, T. E., Albert Engelhardt, H., and Menzel, D. (1975). Adsorption of oxygen and oxidation of co on the ruthenium (001) surface. *Surface Science*, 48(2):304–328. 43, 59, 67, 68

Mason, S. E., Grinberg, I., and Rappe, A. M. (2008). Orbital-specific analysis of co chemisorption on transition-metal surfaces. *The Journal of Physical Chemistry C*, 112(6):1963–1966. 72

Mavrikakis, M., Stoltze, P., and Nørskov, J. K. (2000). Making gold less noble. *Catalysis Letters*, 64(2-4):101–106. 59

Michaelides, A. and Scheffler, M. (2010). An introduction to the theory of metal surfaces. *Textbook of Surface and Interface Science*, 1. xii, 7, 8

Mino, L., Agostini, G., Borfecchia, E., Gianolio, D., Piovano, A., Gallo, E., and Lamberti, C. (2013). Low-dimensional systems investigated by x-ray absorption spectroscopy: a selection of 2d, 1d and 0d cases. *Journal of Physics D: Applied Physics*, 46(42):423001. xii, 2

Mitchell, W. J., Xie, J., Lyons, K. J., and Weinberg, W. H. (1994). Dissociative chemisorption of oxygen on the ru (001) surface: Spectroscopic identification of precursor intermediates at low surface temperatures. *Journal of Vacuum Science & Technology A*, 12(4):2250–2254. 43, 59

Naota, T., Takaya, H., and Murahashi, S.-I. (1998). Ruthenium-catalyzed reactions for organic synthesis. *Chemical reviews*, 98(7):2599–2660. 42

Narumand, D. H. and Childs, K. D. (2004). Auger Spectrometers: A Tutorial Review. *Applied Spectroscopy Reviews*, 34(3):139–158. xv, 39

Nielsen, M., Alberico, E., Baumann, W., Drexler, H.-J., Junge, H., Gladiali, S., and Beller, M. (2013). Low-temperature aqueous-phase methanol dehydrogenation to hydrogen and carbon dioxide. *Nature*. 5, 17, 42

Nieuwenhuys, B. E. (1999). The surface science approach toward understanding automotive exhaust conversion catalysis at the atomic level. *Advances in catalysis*, 44:259–328. 17

Nørskov, J. K., Bligaard, T., Logadottir, A., Bahn, S., Hansen, L. B., Bollinger, M., Bengaard, H., Hammer, B., Sljivancanin, Z., Mavrikakis, M., et al. (2002). Universality in heterogeneous catalysis. *Journal of Catalysis*, 209(2):275–278. xii, 4, 5, 58

Ohring, M. (2001). *Materials science of thin films*. Academic press. 13, 16

Over, H., Kim, Y., Seitsonen, A., Wendt, S., Lundgren, E., Schmid, M., Varga, P., Morgante, A., and Ertl, G. (2000). Atomic-scale structure and catalytic reactivity of the ruo2 (110) surface. *Science*, 287(5457):1474–1476. 3, 4, 6, 17, 42

Park, C. (1988). Growth of ag, au and pd on ru (0001) and co chemisorption. *Surface Science*, 203(3):395–411. 32

Reuter, K. and Scheffler, M. (2001). Composition, structure, and stability of ruo 2 (110) as a function of oxygen pressure. *Physical Review B*, 65(3):035406. 10, 73

Rodahl, M., Hook, F., Krozer, A., Brzezinski, P., and Kasemo, B. (1995). Quartz crystal microbalance setup for frequency and q-factor measurements in gaseous and liquid environments. *Review of Scientific Instruments*, 66(7):3924–3930. 27

Rodriguez, J. and Goodman, D. W. (1992). The nature of the metal-metal bond in bimetallic surfaces. *Science*, 257(5072):897–903. 60, 72

Roduner, E. (2006a). *Nanoscopic materials: size-dependent phenomena*. Royal Society of Chemistry. xii, 2

Roduner, E. (2006b). Size matters: why nanomaterials are different. *Chemical Society Reviews*, 35(7):583–592. 1

Rogal, J. (2006). *Stability, composition and function of palladium surfaces in oxidizing environments*. PhD thesis, Freie Universität Berlin, Universitätsbibliothek. 9

Rogal, J. and Reuter, K. (2006). Ab initio atomistic thermodynamics for surfaces: A primer. Technical report, DTIC Document. 9, 10

Rose, M., Borg, A., Dunphy, J., Mitsui, T., Ogletree, D., and Salmeron, M. (2004). Chemisorption of atomic oxygen on pd (111) studied by stm. *Surface science*, 561(1):69–78. 55, 59

Rothenberg, G. (2008). *Catalysis: concepts and green applications*. Wiley-VCH. 4, 58

Ruban, A., Skriver, H. L., and Nørskov, J. K. (1999). Surface segregation energies in transition-metal alloys. *Physical review B*, 59(24):15990. 49

Smith, A. R., Chao, K.-J., Niu, Q., and Shih, C.-K. (1996). Formation of atomically flat silver films on gaas with a "silver mean" quasi periodicity. *Science*, 273(5272):226–228. 43

Stampfl, C., Schwegmann, S., Over, H., Scheffler, M., and Ertl, G. (1996). Structure and stability of a high-coverage (1× 1) oxygen phase on ru (0001). *Physical review letters*, 77(16):3371. 43, 59, 68

Steltenpohl, A. and Memmel, N. (1999). Adsorption site of oxygen on pd (111). *Surface science*, 443(1):13–18. 55, 56, 68, 75

Stoltze, P. and Nørskov, J. (1985). Bridging the" pressure gap" between ultrahigh-vacuum surface physics and high-pressure catalysis. *Physical review letters*, 55(22):2502. 4

Stroscio, J. A., Feenstra, R., and Fein, A. (1987). Imaging electronic surface states in real space on the si (111) 2× 1 surface. *Journal of Vacuum Science & Technology A*, 5(4):838–841. 35

Tectra (2014). Manual of tectra e-flux evaporator. https://docs.google.com/viewer?url=http%3A%2F%2Fwww.tectra.de%2Fe-flux.pdf. 25

Valden, M., Lai, X., and Goodman, D. W. (1998). Onset of catalytic activity of gold clusters on titania with the appearance of nonmetallic properties. *Science*, 281(5383):1647–1650. 3, 26, 59

Vanderbilt, D., editor (2013). *Band Structure: Bulk and Surface*. Rutgers University. 7

Venables, J. (2000). *Introduction to Surface and Thin Film Processes*. Cambridge University Press. 13

Voogt, E., Mens, A., Gijzeman, O., and Geus, J. (1997). Adsorption of oxygen and surface oxide formation on pd (111) and pd foil studied with ellipsometry, leed, aes and xps. *Surface science*, 373(2):210–220. 52, 68, 74, 75

Wang, Y., Jacobi, K., and Ertl, G. (2003). Interaction of no with the stoichiometric ruo2 (110) surface. *The Journal of Physical Chemistry B*, 107(50):13918–13924. 6, 17, 42

Wei, C. and Chou, M. (2002). Theory of quantum size effects in thin pb (111) films. *Physical Review B*, 66(23):233408. 44

Weissman-Wenocur, D., Shek, M., Stefan, P., Lindau, I., and Spicer, W. (1983). The temperature dependence of the interaction of oxygen with pd (111); a study by photoemission and auger spectroscopy. *Surface Science*, 127(3):513–525. 74, 75

Weitering, H., Heslinga, D., and Hibma, T. (1992). Structure and growth of epitaxial pb on si (111). *Physical Review B*, 45(11):5991. 44

Wilson, O. M., Knecht, M. R., Garcia-Martinez, J. C., and Crooks, R. M. (2006). Effect of pd nanoparticle size on the catalytic hydrogenation of allyl alcohol. *Journal of the American Chemical Society*, 128(14):4510–4511. 3

Wintterlin, J., Trost, J., Renisch, S., Schuster, R., Zambelli, T., and Ertl, G. (1997). Real-time stm observations of atomic equilibrium fluctuations in an adsorbate system: O/ru (0001). *Surface science*, 394(1):159–169. 43, 51, 55, 59, 68

Yip, S. (2007). *Handbook of Materials Modeling part.A*. Springer. xiii, 11

Zangwill, A. (1988). *Physics at surfaces*. Cambridge University Press. 7, 9, 36

Zhang, Z., Niu, Q., and Shih, C.-K. (1998). Electronic growth of metallic over layers on semiconductor substrates. *Physical review letters*, 80(24):5381. 43

Zhu, W., Weitering, H., Wang, E., Kaxiras, E., and Zhang, Z. (2004). Contrasting growth modes of mn on ge (100) and ge (111) surfaces: subsurface segregation versus intermixing. *Physical review letters*, 93(12):126102. 74

Appendix

Appendix A

Computer programs

A.1 Matlab codes

The Matlab program for the model (see Figure 4.5) used to calculate the surface concentration of Pd is given below:

```
% In this program, we are trying to build a correlation among the three
% variables (x,npd,ratio)
% x is hole coverage at the threshold level we choose
% npd is the number of Pd layers we add on top of the Ru film (islands)
% ratio is the calibrated value of Pd330eV/Ru273eV ratio for this system
%.....................................................................
a1=2.3;%Pd c-axis
a2=2.1;%Ru c-axis
d11 = 6.79;%IMFP of 230eV electron in Pd
d12 = 5.66;%IMFP of 230eV electron in Ru
d21 = 7.49;%IMFP of 273eV electron in Pd
d22 = 6.22;%IMFP of 273eV electron in Ru
d31 = 8.41;%IMFP of 330eV electron in Pd
d32 = 6.97;%IMFP of 330eV electron in Ru
```

```
% We are considering the case of Ru thin film grown on Pd(111) substrate

% The second digits in the IMFP variables represent the materials we
% considering
% Pd -> 1
% Ru -> 2

% The first digits in the IMFP variables represent the electron energies we
% are considering
% 230eV -> 1
% 273eV -> 2
% 330eV -> 3

%Bulk Ru signal of 230eV without the prefactor to identify the signal
%strength of one single ML of Ru film
Ru_1b = 1/(1-exp(-a2/d12));
%Bulk Pd signal of 330eV without the prefactor to identify the signal
%strength of one single ML of Pd film
Pd_3b = 1/(1-exp(-a1/d31));

N = 50; % maximum number of Ru MLs we are intersted in
p = 0.01; % precision of film thickness increment in the unit of Ru MLs

%Signal of 230eV electron from Ru films of different thicknesses without
%the prefactor representing the real signal strength of one single ML of Ru
%film
Ru1 = zeros(1,N/p+1);
%Signal of Pd 330eV electron from Pd bulk crystal with Ru films of
%different thicknesses on top, the prefactor representing the real signal
%strength of one single ML of Pd is not included
Pd3 = zeros(1,N/p+1);

d = p:p:N; % film thickness in the unit of MLs
```

```
for i = 1:(N/p+1) % For the case of integer number of MLs
    Ru1(i) = (1-exp(-i*a2/d12))/(1-exp(-a2/d12));
    Pd3(i) = exp(-i*a2/d32)/(1-exp(-a1/d31));
end
% surface layer of Pd films
% Pds(i) is a function of i, i represents the number of Pd MLs
Pds = @(i)(1-exp(-i*a1/d31))/(1-exp(-a1/d31));

%Pd_330eV/Ru_230eV ratio for 0.85 ML Pd on bulk Ru crystal is 2.282576716
%with STDEV of 0.086202627
ratio31 = 2.282576716;
Pd = 0.85;
Ru = Ru_1b*0.15 + Ru_1b*exp(-a1/d11)*0.85;
%The ratio of 1ML Pd_330eV versus 1ML Ru_230eV: r31
r31 = ratio31/(Pd/Ru);

%.....................................................................
n = input('Thickness of unannealed film (unit: Ru ML): ');

x = 0:0.01:0.99; %representing different hole coverages
temp = size(x);
sx = temp(2); %size of array x, 100

% Model 1 only considers the Ru island on Pd bulk crystal, and calculate
% the Pd/Ru ratio in this system
% Model 2 adds surface layer of Pd on top of Ru islands, model 1 doesn't
% For our current interests, Model 2 is the model we want to use
model = input('Model number: ');
% npd belongs to [0,10], representing the number of Pd MLs adding to the
% surface
npd = 0:0.01:9.99;
temp = size(npd);
snpd = temp(2);%size of array npd, 1000
```

```
if model==1
    ratio = zeros(1,sx);
    for i = 1:sx
        np = n/(1-x(i)); %thickness of the unified Ru islands
        ni = floor(np/1);%integer part of np
        f = np - ni;%fractional part of np

        Iru = Ru1(ni)*(1-f)*(1-x(i)) + Ru1(ni+1)*f*(1-x(i));
        Ipd = Pd_3b*x(i) + Pd3(ni)*(1-f)*(1-x(i)) + Pd3(ni+1)*f*(1-x(i));
        ratio(i) = r31*Ipd/Iru;
    end
    plot(x,ratio,'-o');%Pd/Ru_230 ratio versus Ru thickness
else
    ratio = zeros(snpd,sx);
    for i = 1:sx
        np = n/(1-x(i)); %thickness of the unified Ru islands
        ni = floor(np/1);%integer part of np
        f = np - ni;%fractional part of np
        for j = 1:snpd
            npdi = floor(npd(j)/1);
            npdf = npd(j) - npdi;

            Iru = (Ru1(ni)*(1-f)*(1-x(i)) + Ru1(ni+1)*f*(1-x(i)))*(1-npdf)
            *exp(-npdi*a1/d11) + (Ru1(ni)*(1-f)*(1-x(i)) + Ru1(ni+1)*f
            *(1-x(i)))*npdf*exp(-(npdi+1)*a1/d11);
            Ipd = Pds(npdi)*(1-npdf)*(1-x(i)) + Pds(npdi+1)*npdf*
            (1-x(i)) + Pd_3b*x(i) + (Pd3(ni)*(1-f)*(1-x(i)) + Pd3(ni+1)*f
            *(1-x(i)))*(1-npdf)*exp(-npdi*a1/d31) + (Pd3(ni)*(1-f)*(1-x(i))
             + Pd3(ni+1)*f*(1-x(i)))*npdf*exp(-(npdi+1)*a1/d31);

            ratio(j,i) = r31*Ipd/Iru;
        end

    end
```

```
    %contour(x,npd,ratio,2.76);
    disp('Use command surf(x,npd,ratio) to see the 3D surface for the
    sample with pre-determined Ru thickness');
    disp('Use command contour(x,npd,ratio,Pd/Ru_after_anneal) to
    get the contour you want!');
end
```

Appendix B

Mathematical Derivations

B.1 Layer-by-layer attenuation model of the Auger intensity

In section 3.2.2, we discussed a simple model to calibrate the film thickness with Auger spectroscopy. Here, we provide the derivation for some of the equations used in section 3.2.2.

Let I_2 be the intensity of a specific Auger transition originating from a single atomic layer of a given element, a_2 the bulk lattice constant of that element along the direction perpendicular to the layer, and λ_{22} the inelastic mean free path (IMFP) of the Auger electron, then the Auger intensity from the corresponding bulk crystall can be written as

$$I_2^0 = I_2 + I_2 e^{-\frac{a_2}{\lambda_{22}}} + I_2 e^{-\frac{2a_2}{\lambda_{22}}} + I_2 e^{-\frac{3a_2}{\lambda_{22}}} + ... \tag{B.1}$$

Then,

$$e^{-\frac{a_2}{\lambda_{22}}} I_2^0 = I_2 e^{-\frac{a_2}{\lambda_{22}}} + I_2 e^{-\frac{2a_2}{\lambda_{22}}} + I_2 e^{-\frac{3a_2}{\lambda_{22}}} + ... \tag{B.2}$$

Therefore,

$$(1 - e^{-\frac{a_2}{\lambda_{22}}}) I_2^0 = I_2 \tag{B.3}$$

$$I_2^0 = I_2 \frac{1}{1 - e^{-\frac{a_2}{\lambda_{22}}}}, \tag{B.4}$$

where I_2^0 represents the Auger intensity of the bulk material. The superscript "0" means that there is no overlayer on top of the bulk surface.

Similarly, the Auger intensity of a complete n-monolayer thin film can be expressed as

$$I_1^n = I_1 + I_1 e^{-\frac{a_1}{\lambda_{11}}} + I_1 e^{-\frac{2a_1}{\lambda_{11}}} + ... + I_1 e^{-\frac{(n-1)a_1}{\lambda_{11}}}, \tag{B.5}$$

where I_1 is the Auger intensity from one atomic layer of the film, a_1 is the corresponding lattice constant perpendicular to the film, and λ_{11} is the corresponding IMFP. In addition,

$$I_1^n = I_1 \times \frac{1 - e^{-na_1/\lambda_{11}}}{1 - e^{-a_1/\lambda_{11}}}, \tag{B.6}$$

where I_1^n represents the Auger intensity of a n-layer thin film.

If this n-layer thin film is grown on a bulk substrate, then the Auger intensity from the bulk substrate will be

$$I_2^n = I_2 \times \frac{e^{-na_1/\lambda_{21}}}{1 - e^{-a_2/\lambda_{22}}} \tag{B.7}$$

B.2 Oxygen signal normalization

The magnitude on the oxygen Auger signal on the Pd films is represented by the ratio of the 515 eV oxygen $KL_{2,3}L_{2,3}$ peak and the 330eV palladium MNN peak. Because the intensity of the palladium peak increases with the Pd film thickness, we need to normalize the Pd intensities of the films to the experimentally measured magnitude of bulk Pd, in order to determine and compare the oygen surface concentrations for the different films. The normalization is based on the assumption that

$$I_{Pd}^n = I_1^n \times \frac{1 - e^{-na_1/\lambda_{11}}}{1 - e^{-a_1/\lambda_{11}}} \tag{B.8}$$

and

$$I_{Pd}^{bulk} = I_1^n \times \frac{1}{1 - e^{-a_1/\lambda_{11}}} \tag{B.9}$$

In order to compare the oxygen signal from the bulk Ru crystal to the oxygen signals from the Pd films and Pd bulk crystal, we used a second normalization procedure which is based on the fact that

$$I_{Pd}^{bulk}/I_{Ru}^{bulk} = I_1/I_2 \times \frac{1}{1 - e^{-a_1/\lambda_{11}}}/\frac{1}{1 - e^{-a_2/\lambda_{22}}} \tag{B.10}$$

B.3 The d-band shift upon band narrowing

Here, we assume that the filling factor of the d-band is f, and that the d-band has a rectangular shape. If the initial d-band centroid is located at $E_c^i = 0$ and the initial band width is W_i, then the total number of electrons in the d-band can be expressed

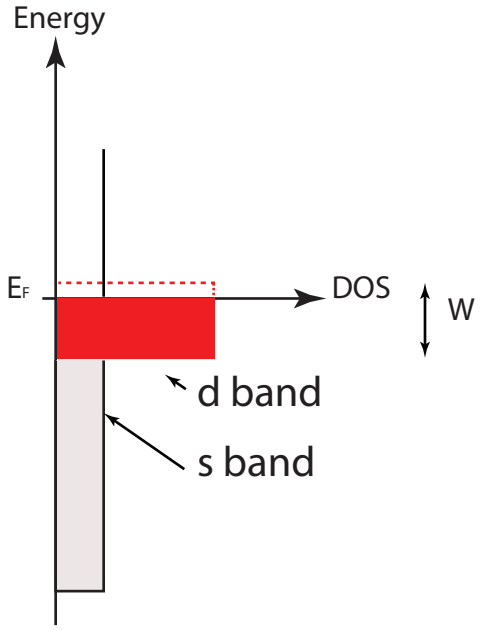

Figure B.1: Schematic illustration of the density of states of a transition metal with a broad s-band and a narrow d-band of width W around the Fermi level.

as

$$N_d = 10f = \int_{-W_i/2}^{E_F} \frac{10}{W_i} dE = \frac{10}{W_i}(E_F + W_i/2) \tag{B.11}$$

When the d-band width changes to W_f, we will assume that in order to maintain the same band filling, the lower edge of the d-band changes to Δ. Then the number of d electrons can be expressed as

$$N_d = 10f = \int_{\Delta}^{E_F} \frac{10}{W_i} dE = \frac{10}{W_f}(E_F + W_f/2) \tag{B.12}$$

Here, we assumed that the position of Fermi level remains constant because in reality, the position of the Fermi level is determined by the bulk. By equating the two equations above, it is easy to show that the new d-band center will be located at

$$E_c^f = \frac{W_f}{2} + \Delta = (1 - \frac{W_f}{W_i})E_F \tag{B.13}$$

This indicates that the d-band shift correlates with the position of Fermi level and thus the d-band shift depends on the filling factor *f*. If $f > 0.5$, narrowing of the d-band will result in an upward shift; if $f < 0.5$ narrowing of the d-band will result in a downward shift.

Vita

Xiangshi Yin was born on August 8, 1987 in Daixian, Shanxi Province, P.R. China. He attended University of Science and Technology of China (USTC) in 2004 after graduating from Xinzhou No.1 High School. He spent four years in USTC and obtained a Bachelor's degree in Physics in 2008. In summer 2008, he joined the physics department of University of Tennessee as a graduate student. One year later, he joined Dr. Hanno Weitering's research group and co-advised by Dr. Hanno Weitering and Dr. Paul Snijders. Since then, he spent five years in the experimental study of the chemical property of Ru and Pd thin films in Oak Ridge National Laboratory and University of Tennessee. He expects to receive his Doctorate of Philosophy degree in Physics in August of 2014.